



Universiteit
Leiden
The Netherlands

Probing quantum materials with novel scanning tunneling microscopy techniques

Bastiaans, K.M.

Citation

Bastiaans, K. M. (2019, December 10). *Probing quantum materials with novel scanning tunneling microscopy techniques*. *Casimir PhD Series*. Retrieved from <https://hdl.handle.net/1887/81815>

Version: Publisher's Version

License: [Licence agreement concerning inclusion of doctoral thesis in the Institutional Repository of the University of Leiden](#)

Downloaded from: <https://hdl.handle.net/1887/81815>

Note: To cite this publication please use the final published version (if applicable).

Cover Page



Universiteit Leiden



The handle <http://hdl.handle.net/1887/81815> holds various files of this Leiden University dissertation.

Author: Bastiaans, K.M.

Title: Probing quantum materials with novel scanning tunneling microscopy techniques

Issue Date: 2019-12-10

Probing quantum materials with novel scanning tunneling microscopy techniques

Proefschrift

ter verkrijging van
de graad van Doctor aan de Universiteit Leiden,
op gezag van Rector Magnificus prof.mr. C.J.J.M. Stolker,
volgens besluit van het College voor Promoties,
te verdedigen op dinsdag 10 december 2019
klokke 11.15 uur

door

Koen Mathijs Bastiaans

geboren te Leiden
in 1990

Promotor: Prof. dr. J. Aarts

Co-promotor: Dr. M.P. Allan

Promotiecommissie: Prof. dr. J.C. Davis

Dr. I. Swart

Prof. dr. E.R. Eliel

Prof. dr. J.M. van Ruitenbeek

Prof. dr. J. Zaanen

University of Oxford

Universiteit Utrecht

Casimir PhD series, Delft-Leiden 2019-40

ISBN 978-90-8593-423-3

An electronic version of this thesis can be found at

<https://openaccess.leidenuniv.nl/>.

Copyright © 2019 Koen Mathijs Bastiaans

Cover design by Ilse Modder (www.ilsemodder.nl)

Printed by Gildeprint - Enschede

This work was supported by the European Research Council (ERC StG SpinMelt) and by the Netherlands Organization for Scientific Research (NWO/OCW), as part of the Frontiers of Nanoscience program (NanoFront), as well as through the Vidi talent scheme (Project No. 680-47-536).

For Arnold and Jan,
two amazing grandfathers

CONTENTS

1	Introduction	1
1.1	A scanning tip to explore quantum matter	4
1.2	The noise as the signal	5
1.3	Probing the condensate	6
1.4	Outline of this thesis	7
	Bibliography	9
2	Amplifier for scanning tunneling microscopy at MHz frequencies	11
2.1	Introduction and motivation	13
2.2	Noise sources in STM	14
2.3	Amplifier and circuit	16
2.3.1	General idea	16
2.3.2	Circuit elements and printed circuit board design	17
2.4	Noise spectroscopy performance on atomically Au(111)	21
2.5	MHz differential conductance measurements	21
2.6	Conclusions and outlook	22
	Bibliography	24
3	Charge trapping and super-Poissonian noise centers in cuprates	27
3.1	Introduction	29
3.2	Noise as the signal	29
3.3	Discovery of super-Poissonian noise centers	31
3.4	Noise spectroscopy on noise centers	31
3.5	Modulated transport by polaronic charge trapping	33
3.6	Conclusions and outlook	35
	Appendices	37
3.A	Correlation to low-energy features	37
3.B	Determination of impurity states	37
3.C	Various super-Poissonian noise centers	40
	Bibliography	41

4	Imaging doubled shot noise in a Josephson STM	45
4.1	Introduction	47
4.2	Experimental setup	48
4.3	Josephson tunneling spectroscopy	49
4.4	Noise spectroscopy	51
4.5	Doubled noise due to Andreev reflections.	52
4.6	Spatially resolved noise doubling	53
4.7	Conclusions and outlook	55
	Bibliography	56
5	A strongly inhomogeneous superfluid in an iron-based superconductor	61
5.1	Introduction	63
5.2	Spectroscopy in a Josephson STM.	63
5.3	Visualizing the inhomogeneous superfluid	66
5.4	Correlation between superfluid density and quasiparticle coherence . .	68
5.5	Conclusions and outlook	71
	Appendices	72
	5.A Accessing the superfluid density with Josephson STM	72
	5.B Determining the critical current from Josephson tunneling spectra.	72
	5.C Visualizing the superfluid density for samples with inhomoge- neous normal state junction resistance	74
	Bibliography	77
6	Melting the Mott state in electron doped iridates	81
6.1	Introduction	83
6.2	Low doping: frozen Mott state	85
6.3	Higher doping: pseudogap and local order	86
	6.3.1 Phase separation: Mott and pseudogap	86
	6.3.2 Emergent order	88
6.4	Doping evolution: impurity band Mott transition.	88
6.5	Conclusions and outlook	91
	Appendices	92
	6.A Experimental setup	92
	6.B Extraction of Δ_{Mott} and Δ_{PG}	92
	Bibliography	94

Samenvatting	97
Curriculum Vitae	101
List of Publications	103
Acknowledgements	105

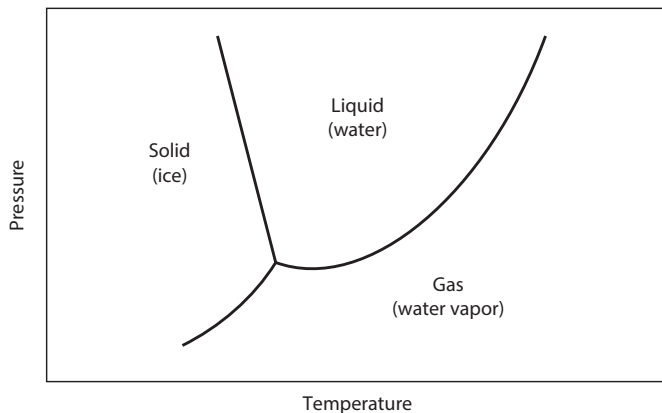
1

Introduction

In this thesis we will deal with the quantum matter realized in electron systems in the structural arrangements of atoms that form a solid. This may sound as a cryptic sentence at first look, but it connects some basic ingredients that form the starting point for this dissertation; it contains the notion that the *electronic* phase and the *structural* phase of a material can be viewed as two distinct properties, which, remarkably, do not need to be the same states of matter. This can be illustrated by the following example: Say you would be asked to think of an electrically conducting material, probably the first thing that comes to mind is a *solid* material, probably a metal. A structural solid is characterized by a close packing of the constituent particles (atoms), and, in the example of a metal, this packing of atoms is regularly ordered in a repeating pattern which gives it its stability and definite shape and volume. In such a solid, because of the rigid (crystalline) arrangement, the constituent particles cannot move freely throughout the material; the constituent particles don't flow. But what about the electronic phase of this material? Each atom in the material brings a set of electrons. If these constituent particles of the electron system would also be rigidly arranged the system would act like a solid; the electrons would not be able to move through the material, as in an electronic insulator. However, in a conducting material the electrons are mobile and thus its electronic phase cannot be equivalent to a solid. As it turns out, we describe the electronic phase of most simple metals by a *gas* or *liquid* phase, which allows us to reproduce many of its electronic properties reasonably well [1, 2].

Using Landau's theory of electronic liquids we can describe the electronic properties

a.



b.

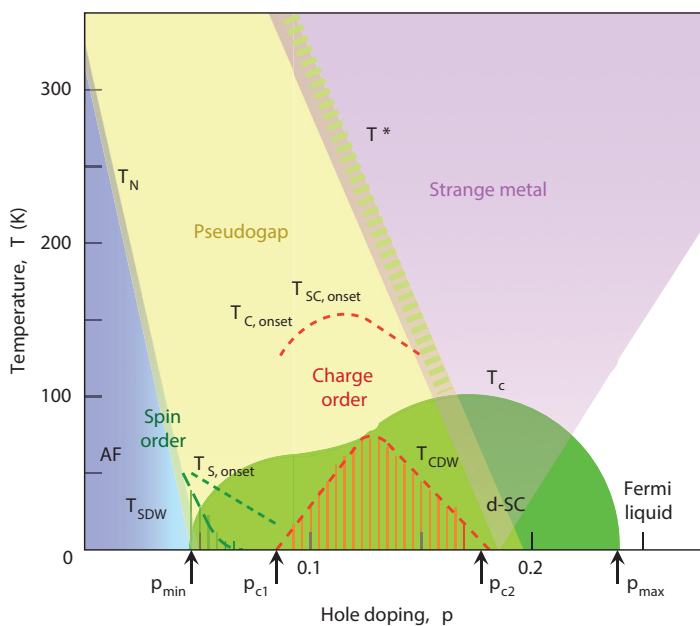


Figure 1.1: **Phase diagrams.** **a.** A typical phase diagram of a simple single substance (for example water). In the temperature - pressure plane, the phase-equilibrium lines separate the three different types of phases. In this case: solid, liquid and gas. **b.** Electronic phase diagram of the cuprate high-temperature superconductor, where as function of temperature and carrier doping the various different electronic phases are shown, presented in a similar fashion as the structural phase diagram of a simple substance (a.). Figure reproduced from Keimer *et al.* [3].

of most simple metals by a non-interacting single-particle picture. But what about materials where the interactions between the particles become so strong that the simple single-particle description starts to fail? Now we enter the realm of the *quantum materials*. Here the independent single-electron picture breaks down since the constituent electronic particles start to notice and influence each other, becoming so-called *strongly correlated*. The collective behavior of all the electrons will start to dictate the general electronic properties of the material. Out of this microscopic strongly correlated electron soup, macroscopic properties can emerge that are quantum mechanical of nature. Superconductivity might be the prime example, where pairing of the electrons induces a new state of matter which can be described by a single macroscopic quantum mechanical wave function. It are not only the strong electronic correlations that can lead to the emergence of complex macroscopic states, making quantum materials stand out from ordinary matter. Such complex electronic states can also require other ingredients such as topological order or quantum criticality, bringing 'quantum' in the material.

The most well studied quantum materials to date are arguably the copper oxide (*cuprate*) high-temperature superconductors. Their rich phase diagram shown in figure 1.1 illustrates the wild zoo of different electronic phases found in these materials. However, despite the large number of experimental and theoretical effort, our contemporary understanding of the microscopic details of these copper oxides still fails to reproduce their emerging macroscopic features and electronic states [3]. For several decades now, the field of condensed matter physics is challenged to understand these emerging states of matter, as well as their driving forces. Interestingly though, the interplay between the electronic and structural phases seems to play an important role. Therefore, in this thesis, in our personal search for understanding, we will employ an experimental technique that can visualize the electronic and structural phases of a material, simultaneously, on the atomic level. We will build upon the existing experimental foundations and add new tools that will allow us to explore the uncharted territory of quantum matter in strongly correlated electron systems.

In the following sections we will introduce a scanning probe technique that will form the point of departure for the work presented in this thesis. We will take this local probe and dress it up with two novel tools, to be able to investigate the relevant quantum mechanical degrees of freedom in strongly correlated quantum matter. After a brief introduction of the scanning probe, we will introduce the concepts of *noise* and *Josephson* scanning tunneling microscopy, followed by a further outline of this thesis.

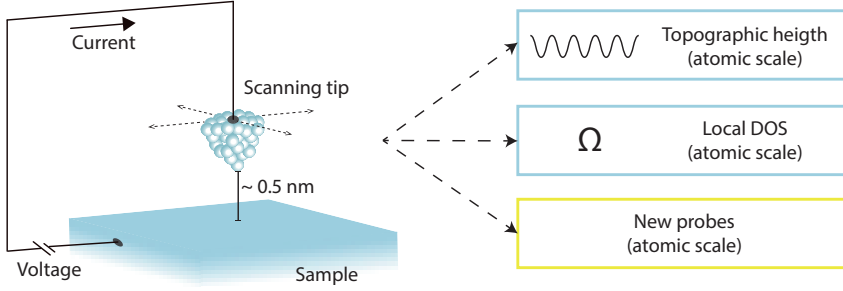


Figure 1.2: **Scanning Tunneling Microscopy (STM)**. A schematic picture to illustrate the experimental setup of STM. An atomically sharp scanning tip is brought in the close vicinity of the sample under investigation (also atomically flat). Applying a bias voltage over the tip-sample junctions results in a measurable tunneling current. This is used to obtain topographic and spectroscopic (local density of states (DOS)) information about the sample. In this thesis we will add two new ingredients by introducing new probes.

1.1. A SCANNING TIP TO EXPLORE QUANTUM MATTER

A scanning tunneling microscope (STM), illustrated in figure 1.2, is an instrument that is designed to visualize the surface of a material on the atomic level. It has established itself as one of the powerful experimental tools to investigate strongly correlated quantum matter. This is, for a large part, due to the fact that STM can spatially resolve the structural and electronic phases with atomic-scale precision. In the following paragraphs we will briefly discuss the basic principles of STM. For all further details we refer to some excellent descriptions elsewhere, see references [4, 5].

STM is based on the concept of quantum tunneling. An (atomically) sharp metallic tip (scanning tip in figure 1.2) is brought in the close vicinity of the clean and atomically flat sample surface. Tip and sample are separated by a thin vacuum barrier (typical tunneling distance ~ 0.5 nm). When a bias voltage is applied over the tip-sample junction, electrons are allowed to tunnel through the vacuum barrier, generating a tunneling current (typically in the pA to nA range) which scales exponentially with the tip-sample separation distance. The tip can be scanned over the sample surface while employing a feedback loop that keeps the tunneling current constant by adjusting the tip-sample separation distance. By measuring the vertical position of the tip while scanning over the sample surface a topographic height image of the surface is made with atomic-scale resolution, allowing for visualization of crystalline atomic structure of the sample. Later on we will refer to such an image as 'topograph'.

The true power of using STM for investigating quantum matter lies in the combination of performing topographic and spectroscopic measurements in the same field of view, both with atomic scale resolution. This allowed for example for the visualization of charge order in cuprate high-temperature superconductors [6–8] and its

nanoscale electronic disorder [9–11]. Also it shed light on Cooper pairing in heavy fermion systems [12, 13] and the nematic electronic structure in an iron-based superconductor [14, 15]. Spatially resolving the electronic structure is done by measuring the local density of states as function of energy (local DOS in figure 1.2), while scanning the tip over the sample surface. The tip is stopped at an equally spaced grid of points to measure the differential conductance (dI/dV) in a set energy window. In this way a three-dimensional dataset is constructed by registering the local density of states as function of spatial coordinates and energy, providing a measure on a broad set of electronic properties of the sample.

We will build on these foundations of STM as a powerful probe to investigate quantum matter. We are challenged by the idea that the decisive information needed to explain most of the complex physical phenomena observed in the phase diagram of quantum matter (see i.e. the phase diagram in figure 1.1) is still missing. Therefore this thesis is devoted to adding new experimental tools to the STM toolset, in order to access physical parameters that are not accessible yet. Our motivation for both new tools will be discussed in the following two sections. Later in this thesis we will develop these techniques and employ them on quantum matter, in order to shed light on (new) physical phenomena, trying to bring us one step closer to decoding the microscopic nature of the phase diagram of quantum materials.

1.2. THE NOISE AS THE SIGNAL

"The noise is the signal." These words by Rolf Landauer are the inspiration for the first new technique we will introduce in this thesis. What Landauer meant was that fluctuations in time of a measurement can be a source of information that is not present in the time-averaged value [16]. What does this mean for the tunneling current between the STM tip and the sample? The basic flow of electrons between the two leads is a purely Poissonian process, meaning that the electrons are completely uncorrelated (they don't influence each other) and transfer at random moments in time between both electrodes. The net amount of charge that these electrons transfer per unit time is what we generally consider as the (time-averaged) magnitude of the current. The deviation from this mean value is what we usually call the *noise*, as illustrated in figure 1.3.

The current noise in a tunnel junction originates from the fact that the flow of charge carriers is discrete (it consists of small packages of charge: electrons)[17]. Since it is the quantized nature of the tunneling current itself that gives rise to the noise, it is also linked to electron-electron correlations and other dynamical charge phenomena. Imagine one would be able to probe the magnitude of these electronic correlations and visualize it on the atomic scale. One could apply it to quantum matter,

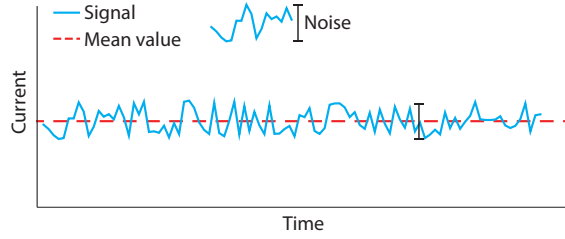


Figure 1.3: **Illustration of 'signal' and 'noise' in a current-time trace.** The tunneling current flowing through the tip-sample junction is the 'signal'. In conventional STM a time averaged value of the tunneling current is measured, here indicated by the red dashed line 'mean'. In this thesis we will improve the temporal resolution of STM in order to also measure the 'noise'.

where the strong electron correlations make up the collective electronic behavior, with the aim to investigate how these electronic correlations make up the emerging states of matter. Unfortunately, one of the main limitations of STM is that the time resolution of the measurement is limited due to the technical details of the experimental setup (which will be discussed in detail later in this thesis), allowing only the measurement of the time-averaged value of the tunneling current (red dashed line in figure 1.3). This prevented quantification the local noise in a scanning tunneling setup up till now. In this thesis we will overcome this limitation and present spatially resolved noise measurements.

In order to add atomic-scale spectroscopic noise measurements to the STM toolbox, we will build on pioneering experiments in STM [18, 19] and high precision quantum transport technologies [20] to tailor the scanning tip into a device that measures the local noise associated with the tunneling current. In this thesis we will discuss this development and unleash it on quantum matter.

1.3. PROBING THE CONDENSATE

The second new technique we will utilize is based on the *Josephson* effect [21]. By using a superconducting STM tip and bringing it in tunneling contact with a superconducting sample, we couple two superconducting macroscopic objects through a thin insulating vacuum barrier, creating a scannable Josephson junction. The tunneling current can now be carried by Cooper pairs, rather than quasiparticles carrying single electron charge, granting direct access to both superconducting condensates.

We will keep the further details of this technique for the later chapters in this thesis, but already we would like to point out the advantage of Josephson STM. While (conventional) STM is a widely used and powerful technique to investigate the su-

perconducting phase of a material, it remarkably doesn't probe the superconducting state directly. Instead it only accesses the single-particle channel, where Bogoliubov quasiparticles with energies larger than the pair-breaking gap transport the charge. Although this already provides an insight into the superconducting phase, we would also like to get access to the Cooper pair channel. Pioneering work by the group of Dynes guides the route of how this should be approached experimentally [22–24]. Recently the first atomic-resolution Josephson experiment on a conventional superconductor [25] and first visualization of an unconventional high-temperature superfluid [26] were reported.

We will take the next step and for the first time visualize the superfluid of an unconventional high-temperature superconductor with atomic-resolution by spatially resolving the Josephson current, while simultaneously also registering the topographic and single-particle electronic properties.

1.4. OUTLINE OF THIS THESIS

In this thesis we will introduce new techniques for scanning tunneling microscopy and use them to reveal uncharted physical phenomena and insights in various quantum materials. The thesis is further organized as follows.

In *chapter 2* we discuss the development, build-up and testing of a novel amplification circuit to measure the tunneling current in the MHz regime, in order to uncover the *shot noise* caused by the tunneling electrons. We demonstrate the unique performance of our amplifier by spatially mapping the noise on a Au(111) surface with atomic resolution in the giga-Ohm regime. We also show differential conductance measurements at 3 MHz, which yields superior performance over the conventional STM spectroscopy techniques.

In *chapter 3* we utilize this newly developed scanning *noise* spectroscopy technique to elucidate the properties of the atomically thin insulating layers in a cuprate high-temperature superconductor. We discover atomic-scale noise centers that exhibit MHz current fluctuations up to 40 times the of the expected noise, which we can attribute to trapping of charge. The results presented in this chapter provide a new picture of how these materials should be looked at: an atomic stacking of atomically thin metallic layers separated by polarizable insulators withing a three-dimensional superconducting state.

In *chapter 4* we combine the scanning *noise* technique with a *Josephson* STM. We image the current noise with atomic resolution on a superconducting Pb(111) surface using a superconducting Pb STM tip. By measuring the current noise as function of applied bias, we reveal the change from single electron tunneling above the super-

conducting gap energy to double electron charge transfer below the superconducting gap energy, and we spatially map this noise doubling over the sample surface.

In *chapter 5* we use atomic-resolution *Josephson* scanning tunneling microscopy to reveal a strongly spatially inhomogeneous superfluid in an iron-based superconductor. By simultaneously measuring the topographic and electronic properties we find that this inhomogeneity in the superfluid is correlated with the coherence of the quasiparticles (electrons / holes) meaning that superconductivity appears to be needed for coherent quasiparticles, locally on the length scale of Cooper pairing.

In *chapter 6* we visualize the electronic properties of an *iridate* sample while crossing the phase transition from a solid electronic phase (Mott state), melting into the so-called pseudogap phase. We show that when extra charge carriers are added into the material a phase-separated state appears along with emergent electronic order and we are able to precisely decode how this state develops from the Mott insulating state. While the material is chemically very different, the phenomena we observe are very similar to that observed in the cuprate high-temperature superconductors. Therefore we attribute them as generic features of doped Mott insulators, disregarding their chemical make-up.

BIBLIOGRAPHY

- [1] C. Kittel, *Introduction to solid state physics*, Vol. 8 (Wiley New York, 1976).
- [2] N. W. Ashcroft and N. D. Mermin, *Solid state physics*, (1976).
- [3] B. Keimer, S. A. Kivelson, M. R. Norman, S. Uchida, and J. Zaanen, *From quantum matter to high-temperature superconductivity in copper oxides*. *Nature* **518**, 179 (2015).
- [4] C. J. Chen, *Introduction to Scanning Tunneling Microscopy Second Edition* (Oxford University Press, 2008).
- [5] R. Wiesendanger, *Scanning probe microscopy and spectroscopy: methods and applications* (Cambridge university press, 1994).
- [6] C. Howald, H. Eisaki, N. Kaneko, M. Greven, and A. Kapitulnik, *Periodic density-of-states modulations in superconducting $\text{Bi}_2\text{Sr}_2\text{CaCu}_2\text{O}_{8+\delta}$* , *Phys. Rev. B* **67**, 014533 (2003).
- [7] T. Hanaguri, C. Lupien, Y. Kohsaka, D.-H. Lee, M. Azuma, M. Takano, H. Takagi, and J. C. Davis, *A 'checkerboard' electronic crystal state in lightly hole-doped $\text{Ca}_{2-x}\text{Na}_x\text{CuO}_2\text{Cl}_2$* , *Nature* **430**, 1001 (2004).
- [8] M. Vershinin, S. Misra, S. Ono, Y. Abe, Y. Ando, and A. Yazdani, *Local ordering in the pseudogap state of the high- T_c superconductor $\text{Bi}_2\text{Sr}_2\text{CaCu}_2\text{O}_{8+\delta}$* , *Science* **303**, 1995 (2004).
- [9] K. M. Lang, V. Madhavan, J. E. Hoffman, E. Hudson, H. Eisaki, S. Uchida, and J. C. Davis, *Imaging the granular structure of high- T_c superconductivity in underdoped $\text{Bi}_2\text{Sr}_2\text{CaCu}_2\text{O}_{8+\delta}$* , *Nature* **415**, 412 (2002).
- [10] C. Howald, P. Fournier, and A. Kapitulnik, *Inherent inhomogeneities in tunneling spectra of $\text{Bi}_2\text{Sr}_2\text{CaCu}_2\text{O}_{8-x}$ crystals in the superconducting state*, *Phys. Rev. B* **64**, 100504 (2001).
- [11] K. McElroy, J. Lee, J. A. Slezak, D.-H. Lee, H. Eisaki, S. Uchida, and J. C. Davis, *Atomic-scale sources and mechanism of nanoscale electronic disorder in $\text{Bi}_2\text{Sr}_2\text{CaCu}_2\text{O}_{8+\delta}$* , *Science* **309**, 1048 (2005).
- [12] M. P. Allan, F. Massee, D. K. Morr, J. Van Dyke, A. W. Rost, A. P. Mackenzie, C. Petrovic, and J. C. Davis, *Imaging cooper pairing of heavy fermions in CeCoIn_5* , *Nature physics* **9**, 468 (2013).
- [13] B. B. Zhou, S. Misra, E. H. da Silva Neto, P. Aynajian, R. E. Baumbach, J. Thompson, E. D. Bauer, and A. Yazdani, *Visualizing nodal heavy fermion superconductivity in CeCoIn_5* , *Nature Physics* **9**, 474 (2013).

- [14] T.-M. Chuang, M. P. Allan, J. Lee, Y. Xie, N. Ni, S. L. Bud'ko, G. S. Boebinger, P. C. Canfield, and J. C. Davis, *Nematic electronic structure in the "parent" state of the iron-based superconductor $\text{Ca}(\text{Fe}_{1-x}\text{Co}_x)\text{As}_2$* , Science **327**, 181 (2010).
- [15] J. E. Hoffman, *Spectroscopic scanning tunneling microscopy insights into Fe -based superconductors*, Reports on Progress in Physics **74**, 124513 (2011).
- [16] C. W. J. Beenakker, C. Schönenberger, *et al.*, *Quantum shot noise*, Physics Today **56**, 37 (2003).
- [17] Y. M. Blanter and M. Büttiker, *Shot noise in mesoscopic conductors*, Physics Reports **336**, 1 (2000).
- [18] H. Birk, M. J. M. De Jong, and C. Schönenberger, *Shot-noise suppression in the single-electron tunneling regime*, Phys. Rev. Lett. **75**, 1610 (1995).
- [19] U. Kemiktarak, T. Ndukum, K. C. Schwab, and K. L. Ekinci, *Radio-frequency scanning tunnelling microscopy*, Nature **450**, 85 (2007).
- [20] L. DiCarlo, Y. Zhang, D. T. McClure, C. M. Marcus, L. N. Pfeiffer, and K. W. West, *System for measuring auto-and cross correlation of current noise at low temperatures*, Rev. Sci. Instrum. **77**, 073906 (2006).
- [21] B. D. Josephson, *Possible new effects in superconductive tunnelling*, Phys. Lett. **1**, 251 (1963).
- [22] O. Naaman, W. Teizer, and R. C. Dynes, *Fluctuation dominated josephson tunneling with a scanning tunneling microscope*, Phys. Rev. Lett. **87**, 097004 (2001).
- [23] H. Kimura, R. Barber Jr, S. Ono, Y. Ando, and R. C. Dynes, *Scanning josephson tunneling microscopy of single-crystal $\text{Bi}_2\text{Sr}_2\text{CaCu}_2\text{O}_{8+\delta}$ with a conventional superconducting tip*, Phys. Rev. Lett. **101**, 037002 (2008).
- [24] H. Kimura, R. P. Barber Jr, S. Ono, Y. Ando, and R. C. Dynes, *Josephson scanning tunneling microscopy: A local and direct probe of the superconducting order parameter*, Phys. Rev. B **80**, 144506 (2009).
- [25] M. T. Randeria, B. E. Feldman, I. K. Drozdov, and A. Yazdani, *Scanning Josephson spectroscopy on the atomic scale*, Phys. Rev. B **93**, 161115(R) (2016).
- [26] M. H. Hamidian, S. D. Edkins, S. H. Joo, A. Kostin, H. Eisaki, S. Uchida, M. J. Lawler, E.-A. Kim, A. P. Mackenzie, K. Fujita, J. Lee, and J. C. Davis, *Detection of a cooper-pair density wave in $\text{Bi}_2\text{Sr}_2\text{CaCu}_2\text{O}_{8+x}$* , Nature **532**, 343 (2016).

2

Amplifier for scanning tunneling microscopy at MHz frequencies

This chapter has been published as *Rev. Sci. Instrum.* **89**, 093709 (2018)

Conventional scanning tunneling microscopy (STM) is limited to a bandwidth of a few kHz around DC. In this chapter, we develop, build and test a novel amplifier circuit capable of measuring the tunneling current in the MHz regime while simultaneously performing conventional STM measurements. This is achieved with an amplifier circuit including a LC tank with a quality factor exceeding 600 and a home-built, low-noise high electron mobility transistor (HEMT). The amplifier circuit functions while simultaneously scanning with atomic resolution in the tunneling regime, i.e. at junction resistances in the range of giga-ohms, and down towards point contact spectroscopy. To enable high signal-to-noise and meet all technical requirements for the inclusion in a commercial low temperature, ultra-high vacuum STM, we use superconducting cross-wound inductors and choose materials and circuit elements with low heat load. We demonstrate the high performance of the amplifier by spatially mapping the Poissonian noise of tunneling electrons on an atomically clean Au(111) surface. We also show differential conductance spectroscopy measurements at 3 MHz, demonstrating superior performance over conventional spectroscopy techniques.

2.1. INTRODUCTION AND MOTIVATION

Possible applications of scanning tunneling microscopy (STM) experiments in the MHz regime include high-frequency differential conductance measurements, scanning spin resonance experiments, and noise spectroscopy on the atomic scale. Conventionally, this is prevented in STM by the combination of a GOhm resistance of the tunnel junction and a capacitor from the cabling which together form a low pass filter in the kHz regime. In this chapter, we build a matching circuit including superconducting inductors and a home-built HEMT that allows us to measure STM currents at MHz frequencies while remaining in tunneling and with atomic resolution. We demonstrate the amplifier's superior performance for both scanning noise spectroscopy and MHz differential conductance measurements.

We start with an introduction to noise spectroscopy. Measurements of electronic noise can yield information in mesoscopic systems that is not present in their time-averaged transport characteristics, including fractional charges in the quantum hall regime [1, 2], the doubling of charge in Andreev processes (see also chapter 4) [3], Coulomb interactions in quantum dots [4–7] and the vanishing of noise in break junctions at the quantum conductance [8]. Generally, the quantity of interest is the deviation of the noise from the Poissonian noise of independent tunneling events of electrons, $S_P = 2e|I|$, with e the electron charge and I the current [9, 10]. Here we define the normalized noise S_n as the ratio between measured (S) and Poissonian (S_P) noise, $S_n = S/S_P$, similar to the Fano factor F . For an uncorrelated electronic liquid, one expects $S_n = 1$; but one can imagine systems where the charge of the carriers is not equal to the electron charge ($q \neq e$) or where the electron flow is strongly correlated. In these cases, the Fano factor will not be equal to unity, i.e. the current noise will be smaller or larger than the Poissonian value even though the time-averaged value of the current will not be influenced. Resolving the noise with atomic precision might provide us with new information in systems with strong electronic correlations or charge aggregations that are not present in the mean current. This is our main motivation to combine noise measurement with scanning probe microscopy.

As for the application of MHz differential conductance measurements, we use a lock-in amplifier as it is done conventionally, but with 3 MHz instead of the more common 400 Hz – 1 kHz. The clear advantage is that in this way, one can perform the spectroscopy measurement in a frequency window where $1/f$ noise is much lower. In addition to this, we can clearly separate the high and low frequency signal, thus it is, for example, easier to measure in feedback.

Bringing noise measurements to STM in the tunneling regime comes with unique challenges, which prevented any atomic resolution noise measurement in the tunneling regime thus far. The high impedance of the tunnel junction, formed by the few angstroms vacuum gap between the STM tip and sample, is the critical obstacle. To-

gether with the capacitance of the interfacing coax cable, the junction acts as a low pass filter only allowing transmission of signals in the small frequency range [11]. Moreover, conventional amplifiers used in STM also have a limited bandwidth due to a large feedback resistor and unavoidable parasitic capacitances [12]. This conventional STM circuitry limits the bandwidth to detect the tunneling current from DC to a few kHz (Fig. 1a). Possible solutions to this are bootstrapping the amplifier [13–16], or impedance matching [11]. These enabled noise measurements in MOhm tunnel junctions [11, 13, 17, 18], but a GOhm impedance as it is present in many STM experiments still leads to prohibitive losses in the matching circuit.

In this chapter, we report on a new amplifier circuit that allows us to overcome these challenges. The requirements for our amplifier were: (i) the amplifier should not interfere with traditional STM measurements, (ii) it should work in the GOhm regime, (iii), it has to be possible to easily implement the amplifier in a commercial STM, (iv) it has to be compatible with UHV, implying low outgassing so that the system can be baked and ultra-high- (cryogenic) vacuum can be achieved.

Our key figures of merit are: (i) the low noise of the circuit, (ii) the most efficient separation of high and low frequency signals, and (iii) the highest possible Q factor of the resonator for highest amplification at 3 MHz.

This chapter is structured as follows. Noise in a STM junction is discussed in section 2.2. A block diagram of the newly developed system for noise-spectroscopy measurements in STM is presented in section 2.3.a, followed by a discussion on the requirements for implementing such techniques in STM. Section 2.3.b describes the realization of this new amplifier. A demonstration measurement on an Au(111) surface is presented in section 2.4. Differential conductance measurements with MHz voltage modulation are discussed in section 2.5.

2.2. NOISE SOURCES IN STM

We start by considering the types of unwanted noise present in a STM setup: mechanical noise, thermal (Johnson) noise, amplifier noise, and flicker ($1/f$) noise.

They have distinguishable frequency dependences, as shown in Fig. 2.1.a. First, flicker noise or $1/f$ noise, which is present in almost all electronic devices. The power spectral density of this low-frequency phenomenon is inversely proportional to the frequency and is related to slow resistance fluctuations modulated by temperature variations. Second, noise induced by mechanical vibrations transferred to the junction, where this mechanical noise is converted to current noise. Both noise sources are usually present in the range from DC to a few kHz, indicated by the blue shaded area in Fig. 2.1.a. This emphasizes that the low frequency regime should be avoided

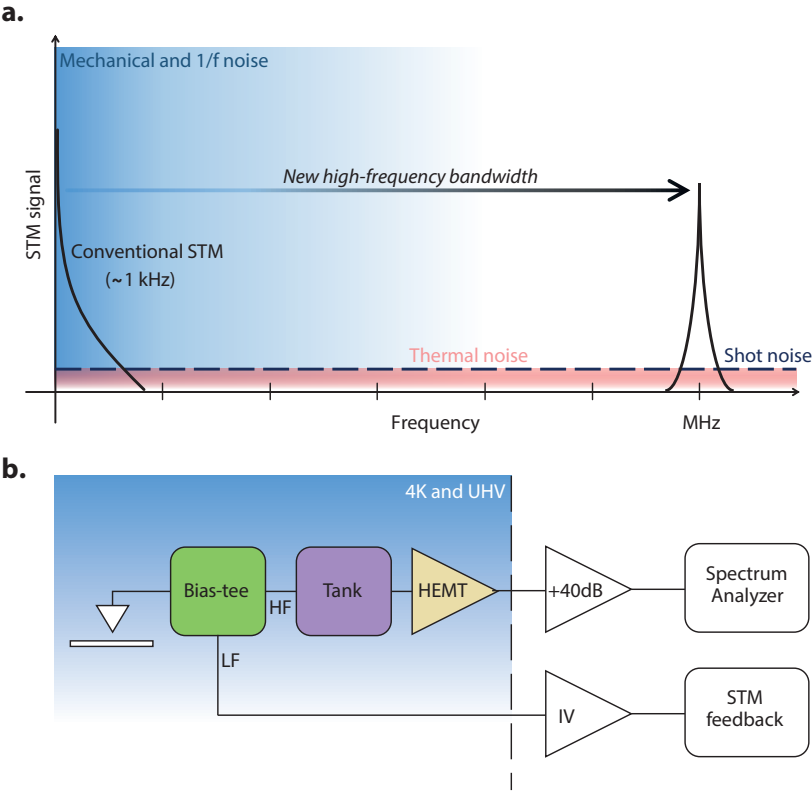


Figure 2.1: **Noise in scanning tunneling microscopy (STM).** **a.** The different noise sources in STM and their frequency dependence are depicted in this schematic plot. At low frequencies mechanical and $1/f$ noise dominate (indicated by blue region), in this region conventional STM is sensitive. To measure shot noise in the tunnel junction we need to create a new bandwidth at high-frequency. Here thermal noise and shot noise are the most dominant noise sources, since they are independent of frequency. **b.** Requirements for the newly built amplifier for combining STM and noise-spectroscopy. Crucial components are highlighted: i) the bias-tee (green) that separates the low and high frequency signals. ii) tank circuit (purple). iii) High electron mobility transistor (HEMT, indicated in yellow) to amplify the high-frequency signal. Both the low and high frequency signals have additional room temperature amplification and detection (white).

and illustrates the disadvantages of the conventional STM bandwidth.

At higher frequencies, the current fluctuations are dominated by thermal noise and shot noise, both of which are informative about the sample. In principle, both phenomena are frequency independent (white noise), and thus are also present at lower frequencies, where the total noise power is dominated by the other contributions. Thermal (also called Johnson-Nyquist) noise is the thermodynamic electronic noise in any conductor with a finite resistance R ; its power spectral density is constant throughout the frequency spectrum, $S = 4k_B T$, where k_B is Boltzmann's constant and T is the temperature. Since thermal noise in a conductor is proportional to the temperature, it can be lowered by reducing the temperature. It can be distinguished from shot noise at zero current, where the latter vanishes.

Our goal is thus to increase the bandwidth and move it to higher frequencies, all whilst retaining the conventional capabilities and staying in the tunneling regime.

2.3. AMPLIFIER AND CIRCUIT

2.3.1. GENERAL IDEA

To achieve the requirements and goals of section 2.1 while avoiding the unwanted noise sources described in section 2.2, we develop a resonance circuit based amplifier including a resonator-based bias-tee.

We follow the principle of amplifier circuits built for noise spectroscopy measurements in mesoscopic systems [19–22] but we modify it to work for high junction resistances in the GOhm regime and to be compatible with STM. Figure 2.1.b shows a block diagram of the amplifier circuit combined with STM. First, a bias-tee (green) separates the low- and high-frequency signals coming from the STM junction. The low-frequency part is needed for the STM feedback loop, where the current is converted to a voltage by a transimpedance amplifier at room temperature. To separate the high frequency, one could use a bias-tee consisting of an inductor in one arm and a capacitor in the other one. However, as we still need a kHz bandwidth in the low frequency branch and as we want to minimize losses of the high frequency signal, we use a resonator based bias-tee.

The high-frequency part of the signal is then passed through the parallel RLC circuit (tank, indicated in purple Fig. 2.1.b), which converts current to voltage at the resonance frequency of the tank circuit $f_0 = (2\pi\sqrt{LC})^{-1}$. The voltage over the tank circuit is detected by the gate of a high electron mobility transistor (HEMT, indicated in yellow Fig. 2.1.b) with very low input referred voltage [23, 24] and current noise, operating at the base temperature ($T \sim 3.3$ K in this chapter) of the STM. Through

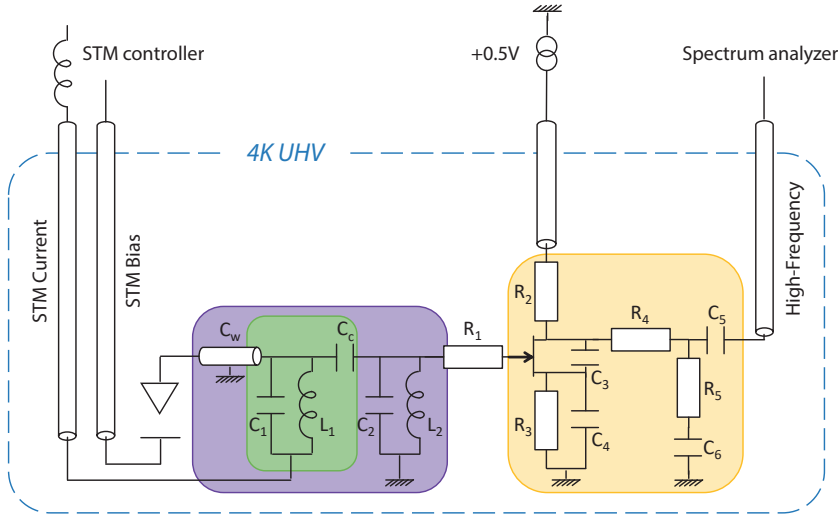


Figure 2.2: **Circuit diagram of the newly developed amplifier for scanning noise spectroscopy.** The colored boxes (green, purple and yellow) highlight specific parts of the amplifier corresponding to Fig. 2.1.b.

the transimpedance of the HEMT, the voltage fluctuations at its gate are converted into current fluctuations. These are measured over a $50\ \Omega$ resistor to finalize the impedance transformation. Note that while the voltage/current gain of the amplifier is of order unity, the gain of power is considerable. A $50\ \Omega$ coaxial line connects the amplifier circuit to a commercial 40 dB current amplifier at room temperature. Finally, the signal line is terminated by the $50\ \Omega$ input impedance of the spectrum analyzer.

2.3.2. CIRCUIT ELEMENTS AND PRINTED CIRCUIT BOARD DESIGN

The heart of the circuit is built on a ceramic printed circuit board (Rogers Corp TMM10i, selected for the very low outgassing properties) as depicted in Fig. 2.2 and described below. Figure 2.2 shows the circuit schematics of the amplifier. The board is located close to the STM head, at the base temperature of the liquid He 4 cryostat (Unisoku USM1500).

The input of the amplifier is connected to the STM tip via a coaxial cable (silver plated Cu mini-coax CW2040-3650F) with a total capacitance between inner and outer conductor of $C_w = 30\ \text{pF}$. The bias-tee (indicated by green shading) and tank (purple shading) combination is formed by two home-built superconducting Niobium inductors $L_1 = L_2 = 66\ \mu\text{H}$ coupled by capacitors $C_c = 100\ \text{pF}$ (Murata GRM 0805-size surface mount). The low-frequency transmission of the bias-tee is shown in Fig.

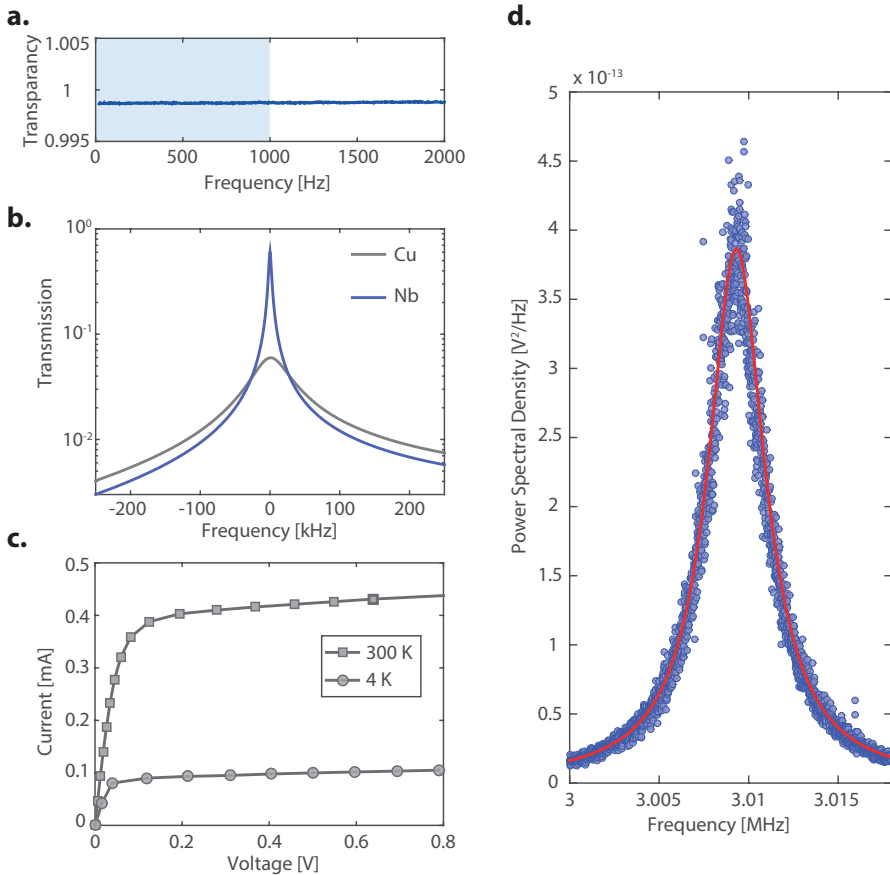


Figure 2.3: **a.** Low-frequency signal used for the STM feedback system. The transparency is close to 1 and flat from DC up to 2 kHz. Bandwidth of the FEMTO transimpedance amplifier (1kHz) is indicated by the shaded blue area. **b.** Transmission of a home-built copper (grey) and superconducting niobium (blue) inductor resonator circuit. The latter showing a much higher quality factor. **c.** Current-voltage characteristics of the high electron mobility transistor (HEMT) at 300 K and LHe temperatures. **d.** Power spectral density measured in a small bandwidth around the resonance frequency of the tank circuit (3.009 MHz). Blue dots are measured data points, red curve corresponds to a circuit diagram fit.

2.3.a, measured at low temperature. The flat transfer function in the frequency range of the Femto IV amplifier (1 kHz, blue shaded area in Fig. 2.3.a) ensures that this amplification scheme can be used for the STM feedback system.

The resonance circuit is formed by the self-resonance of the superconducting Nb inductors in combination with the coaxial cable C_w , providing a resonance frequency of 3.009 MHz. Parallel self-capacitances of the Nb inductors are also shown in Fig. 2.2.a, $C_1 = 15$ pF and $C_2 = 15$ pF. The Niobium inductors are made by cross-winding annealed Nb wire of 100 μm in diameter around a customized ceramic (macor) core. We choose superconducting Nb inductors to enhance the quality factor of the resonator, increasing current-to-voltage amplification at resonance. At 4 K, the Nb inductors show a high quality factor of $Q = 600$, 50 times larger than similarly made Cu inductors ($Q = 12$), see Fig. 2.3.b. The Nb inductors are covered by a Nb shield to minimize Eddy current damping, ensuring the highest possible quality factor Q .

The high-impedance part of the amplification scheme (tank circuit coupled to STM junction) is matched to the 50 Ω impedance of the spectrum analyzer by a home-built low-noise high electron mobility transistor (HEMT) made using molecular beam epitaxy. These specially designed HEMT's have a carrier mobility of $48\text{ m}^2/\text{Vs}$ and can reach unprecedented low noise levels at 1 MHz with a noise voltage of $0.25\text{ nV}/\sqrt{\text{Hz}}$ and a noise current of $2.2\text{ fA}/\sqrt{\text{Hz}}$, under deep cryogenic conditions (≤ 4.2 K), and with an input capacitance of about 5 pF [23, 24]. In addition, components $C_3 = 10$ pF, $R_1 = 10\Omega$ and $R_4 = 10\Omega$ are placed close to the HEMT case to improve its stability.

The operation point of the HEMT is determined by R_2 and R_3 and the supply voltage. Since we aim to have a very low power dissipation we choose $R_2 = 1\text{ k}\Omega$ to give a saturation current of the HEMT of a few tenths of mA. To ensure linear gate voltage to current conversion we operate the HEMT in saturation. We measured the drain current as function of drain-source voltage at room temperature and 4 K by varying the supply voltage, as depicted in Fig. 2.3.c. In the following demonstration the HEMT is biased in saturation at $V = 0.5$ V.

The voltage fluctuations in the 50 Ω line are amplified at room temperature by a +40 dB current amplifier with an input voltage noise of $310\text{ pV}/\sqrt{\text{Hz}}$ (Femto HSA-X-1-40) and is finally terminated by the 50 Ω input impedance of a Zurich Instruments MFLI digital spectrum analyzer. The power spectral density measured at the input of the spectrum analyzer is plotted in Fig. 2.3.d where the blue dots are the measured data points and the red curve represents a circuit diagram fit.

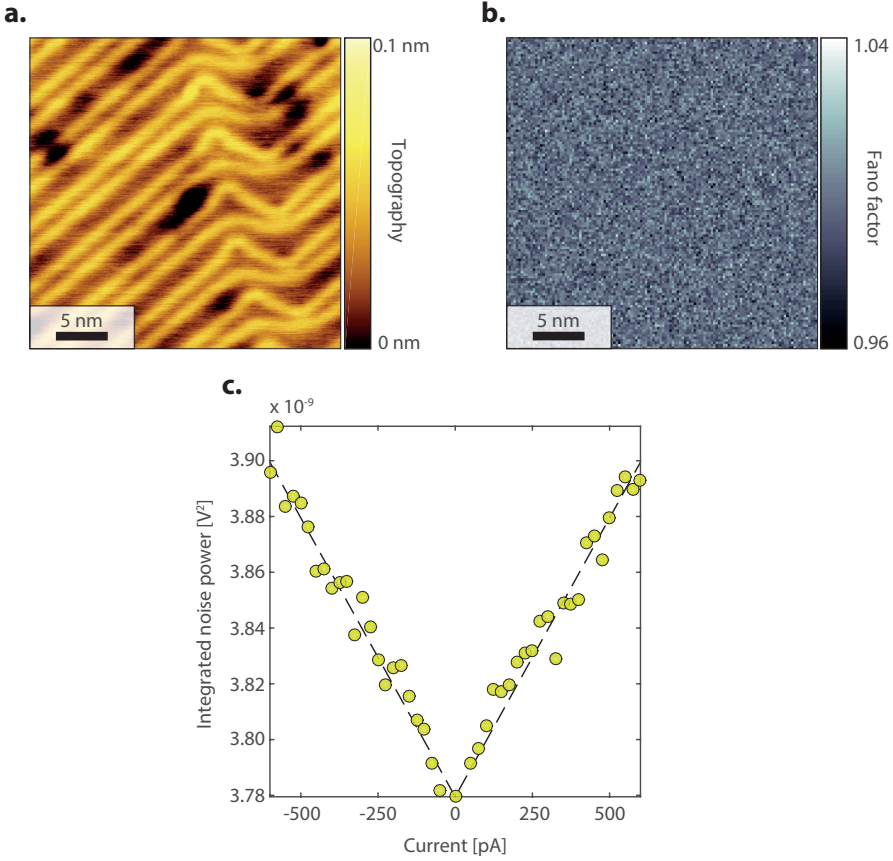


Figure 2.4: **Benchmark of noise-sensitive measurements on a gold on mica sample.** **a.** An atomically resolved STM topographic image of the Au(111) surface on a 30 nm field of view, the 'herringbone' reconstruction is clearly visible. (Setup conditions bias: 100 mV, current set point: 100 pA). **b.** Spatially resolved noise map at 500 mV, 500 pA in the same field of view as Fig 2.4.a, acquired in 48 hours. It shows homogenous Poissonian (Fano = 1) noise at all locations. Here the Fano factor is extracted as $F_{\text{measured}} = (S(500\text{pA}) - S(0\text{pA})) / (2e500\text{pA})$. **c.** Single point noise spectrum acquired at a random location in Fig. 2.4.b. The tunnel junction resistance is kept fixed to 1 GOhm. The dashed line indicates Poissonian shot noise $F = 1$.

2.4. NOISE SPECTROSCOPY PERFORMANCE ON ATOMICALLY Au(111)

To demonstrate the simultaneous use of the STM feedback system and noise sensitive measurements in the tunneling regime, we performed noise spectroscopy measurements on a gold on mica sample. We believe that the Au(111) surface is most ideal for characterizing our noise-sensitive measurement since the sample is metallic thus any electron correlations are negligible. Figure 2.4.a depicts an atomic-resolution image of the Au(111) terminated surface on a 30 nm field of view, the characteristic 'herringbone' reconstruction is clearly visible.

In the same field of view we performed noise-spectroscopy measurements to resolve the current noise with atomic-scale resolution. Even though several topographic features can be observed, the spatially resolved noise map (Fig. 2.4.b) exhibits homogeneous contrast, as is expected for a classical uncorrelated flow of electrons between sample and tip. The 128×128 pixel noise map was acquired in circa 48 hours.

The single point noise spectra (Fig. 2.4.c) acquired at randomly chosen sites always show a linear increase of the noise with increasing current for a typical tunneling junction resistance (1GOhm). The linear increase of the noise is a unique characteristic of shot noise in the junction.

2.5. MHZ DIFFERENTIAL CONDUCTANCE MEASUREMENTS

A second application for our amplifier circuit is to measure differential conductance (dI/dV) which is proportional to the local density of states in a frequency range where $1/f$ noise is suppressed. In conventional STM differential conductance measurements, a voltage modulation has to be applied in the DC - 1 kHz range, now we can also perform dI/dV measurements at 3 MHz. At this frequency, $1/f$ (and other) noise should be considerably lower, as we discussed in section 2.2, Fig. 2.1.a. Therefore, we expect that differential conductance measurements performed at 3 MHz will show superior performance over conventional spectroscopic-imaging STM measurements.

Figure 2.5.a shows that we can resolve the 3 MHz voltage modulation, applied to the sample, within the tank bandwidth; the sharp peak in Fig. 2.5.a (0.5 mV modulation amplitude at 3.009 MHz) is 6 orders of magnitude higher than the background. To verify that the signal to noise ratio of MHz differential conductance measurements is higher than state-of-the-art STM techniques, we will compare the two by the means of a demonstration measurement on a Pb(111) sample using a Pb-coated PtIr tip at 3.3 K.

First, we compare the differential conductance measured over a period of 10 s in tunneling (6 mV, 200 pA) with the feedback disabled. In this way we can check the influence of slow ($1/f$) fluctuations on the differential conductance signal. Comparing the conventional dI/dV measurement (Fig. 2.5.b, measured using the RHK R9 STM controller) with the MHz measurement (Fig. 2.5.c, measured using the Zurich Instruments MFLI) reveals that the former is subject to much severe low-frequency fluctuations than the latter. This directly translates into a higher quality dI/dV spectrum, as can be seen by comparing the 3.009 MHz dI/dV spectrum (Fig. 2.5.e) to the one measured at 887 Hz (Fig. 2.5.d).

2.6. CONCLUSIONS AND OUTLOOK

In this chapter we have shown how we have built a low temperature, low noise amplifier to measure the current (fluctuations) in a STM setup at a MHz frequency. We used two superconducting Nb inductors to form a bias-tee and tank resonator coupled to a home-built, low-noise HEMT which is essential for the impedance matching to $50\ \Omega$ coax cable. We demonstrated the performance of this amplifier by performing noise spectroscopy measurements on an Au(111) surface, showcasing simultaneous visualization of the surface topology and atomically resolved noise maps. We further demonstrated that the amplifier allows to measure differential conductance spectra at 3 MHz where $1/f$ noise is strongly suppressed.

The development of this MHz amplifier, along with recent developments from other research groups [25], directly opens new paths to explore many-body correlation effects in quantum materials. As we will discuss in the next chapter, we use MHz noise-spectroscopy in a STM setup to discover slow MHz timescale charge trapping behavior in a cuprate high-temperature superconducting, providing unique insights in the so-called 'c-axis mystery' in these materials. In chapter 4 we will use the same noise-spectroscopy technique to demonstrate the doubling of the noise due to Andreev reflections in a Josephson STM, and elucidate its future potential. Further, the developments presented in this chapter also open additional possibilities to probe electron spin resonances (ESR) in STM. ESR often leads to periodic processes and equilibration times in the MHz to GHz regime [26, 27]. These can be measured impedance matched with the presented amplifier instead of measuring indirect effects on the DC current. This could be further improved by guiding the microwave signal directly on the tip with coplanar waveguides, as suggested recently [28]. Finally, one could imagine that the thermal noise, introduced here as an unwanted noise source, could yield information about the sample via cross-correlation noise [29].

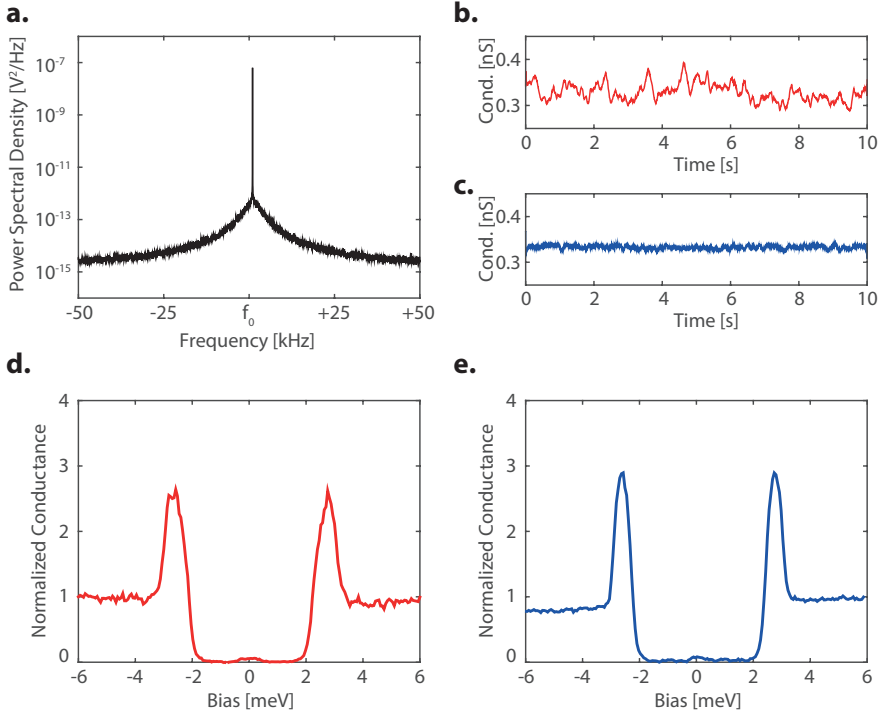


Figure 2.5: **MHz differential conductance.** **a.** Power spectrum obtained around the resonance peak. The modulation signal for the lock-in measurement is applied at the resonance frequency (3.009 MHz). **b.** Differential conductance measured over time at 887 Hz. A voltage modulation of 0.5 mV is used and feedback is disabled. **c.** Differential conductance measured over time at the resonance frequency (3.009 MHz) under similar conditions as figure 2.5.b. **d.** Differential conductance spectrum obtained with a 0.5 mV voltage modulation at 887 Hz (time constant 2 ms) on a Pb(111) surface at a base temperature of 3.3 K. **e.** Differential conductance spectrum obtained at the resonance frequency (3.009 MHz, time constant 3.5 μ s) obtained under the same conditions as figure 2.5.d.

BIBLIOGRAPHY

- [1] R. De-Picciotto, M. Reznikov, M. Heiblum, V. Umansky, G. Bunin, and D. Mahalu, *Direct observation of a fractional charge*, Nature **389**, 162 (1997).
- [2] L. Saminadayar, D. C. Glatthi, Y. Jin, and B. Etienne, *Observation of the $e/3$ fractionally charged Laughlin quasiparticle*, Phys. Rev. Lett. **79**, 2526 (1997).
- [3] Y. Ronen, Y. Cohen, J.-H. Kang, A. Haim, M.-T. Rieder, M. Heiblum, D. Mahalu, and H. Shtrikman, *Charge of a quasiparticle in a superconductor*, PNAS **113**, 1743 (2016).
- [4] A. Thielmann, M. H. Hettler, J. König, and G. Schön, *Cotunneling current and shot noise in quantum dots*, Phys. Rev. Lett. **95**, 146806 (2005).
- [5] E. Onac, F. Balestro, B. Trauzettel, C. F. J. Lodewijk, and L. P. Kouwenhoven, *Shot-noise detection in a carbon nanotube quantum dot*, Phys. Rev. Lett. **96**, 026803 (2006).
- [6] G. Iannaccone, G. Lombardi, M. Macucci, and B. Pellegrini, *Enhanced shot noise in resonant tunneling: Theory and experiment*, Phys. Rev. Lett. **80**, 1054 (1998).
- [7] S. Oberholzer, E. V. Sukhorukov, C. Strunk, C. Schönenberger, T. Heinzel, and M. Holland, *Shot noise by quantum scattering in chaotic cavities*, Phys. Rev. Lett. **86**, 2114 (2001).
- [8] H. E. Van den Brom and J. M. Van Ruitenbeek, *Quantum suppression of shot noise in atom-size metallic contacts*, Phys. Rev. Lett. **82**, 1526 (1999).
- [9] Y. M. Blanter and M. Büttiker, *Shot noise in mesoscopic conductors*, Physics Reports **336**, 1 (2000).
- [10] Y. M. Blanter and M. Büttiker, *Transition from sub-poissonian to super-poissonian shot noise in resonant quantum wells*, Physical Rev. B **59**, 10217 (1999).
- [11] U. Kemiktarak, T. Ndukum, K. C. Schwab, and K. L. Ekinci, *Radio-frequency scanning tunnelling microscopy*, Nature **450**, 85 (2007).
- [12] C. J. Chen, *Introduction to scanning tunneling microscopy*, Vol. 4 (Oxford University Press on Demand, 1993).
- [13] H. Birk, M. J. M. De Jong, and C. Schönenberger, *Shot-noise suppression in the single-electron tunneling regime*, Phys. Rev. Lett. **75**, 1610 (1995).
- [14] H. Birk, K. Oostveen, and C. Schönenberger, *Preamplifier for electric-current noise measurements at low temperatures*, Rev. Sci. Instrum. **67**, 2977 (1996).

- [15] M. J. Rost, L. Crama, P. Schakel, E. van Tol, G. B. E. M. van Velzen-Williams, C. F. Overgaw, H. ter Horst, H. Dekker, B. Okhuijsen, M. Seynen, A. Vijftigschild, P. Han, A. J. Katan, K. Schoots, R. Schumm, W. van Loo, T. H. Oosterkamp, and J. W. M. Frenken, *Scanning probe microscopes go video rate and beyond*, Rev. Sci. Instrum. **76**, 053710 (2005).
- [16] H. Mamin, H. Birk, P. Wimmer, and D. Rugar, *High-speed scanning tunneling microscopy: Principles and applications*, Journal of applied physics **75**, 161 (1994).
- [17] A. Burtzloff, A. Weismann, M. Brandbyge, and R. Berndt, *Shot noise as a probe of spin-polarized transport through single atoms*, Phys. Rev. Lett. **114**, 016602 (2015).
- [18] A. Burtzloff, N. L. Schneider, A. Weismann, and R. Berndt, *Shot noise from single atom contacts in a scanning tunneling microscope*, Surface Science **643**, 10 (2016).
- [19] L. DiCarlo, Y. Zhang, D. T. McClure, C. M. Marcus, L. N. Pfeiffer, and K. W. West, *System for measuring auto-and cross correlation of current noise at low temperatures*, Rev. Sci. Instrum. **77**, 073906 (2006).
- [20] T. Arakawa, Y. Nishihara, M. Maeda, S. Norimoto, and K. Kobayashi, *Cryogenic amplifier for shot noise measurement at 20 mk*, Applied Physics Letters **103**, 172104 (2013).
- [21] M. Hashisaka, Y. Yamauchi, S. Nakamura, S. Kasai, K. Kobayashi, and T. Ono, *Measurement for quantum shot noise in a quantum point contact at low temperatures*, in *Journal of Physics: Conference Series*, Vol. 109 (IOP Publishing, 2008) p. 012013.
- [22] A. M. Robinson and V. I. Talyanskii, *Cryogenic amplifier for 1 mhz with a high input impedance using a commercial pseudomorphic high electron mobility transistor*, Rev. Sci. Instrum. **75**, 3169 (2004).
- [23] Q. Dong, Y. X. Liang, D. Ferry, A. Cavanna, U. Gennser, L. Couraud, and Y. Jin, *Ultra-low noise high electron mobility transistors for high-impedance and low-frequency deep cryogenic readout electronics*, Applied Physics Letters **105**, 013504 (2014).
- [24] Y. Jin, Q. Dong, U. Gennser, L. Couraud, A. Cavanna, and C. Ulysse, *Ultra-low noise cryohemts for cryogenic high-impedance readout electronics: Results and applications*, in *2016 13th IEEE International Conference on Solid-State and Integrated Circuit Technology (ICSICT)* (IEEE, 2016) pp. 342–345.
- [25] F. Massee, Q. Dong, A. Cavanna, Y. Jin, and M. Aprili, *Atomic scale shot-noise using cryogenic mhz circuitry*, Rev. Sci. Instrum. **89**, 093708 (2018).

- [26] S. Loth, M. Etzkorn, C. P. Lutz, D. M. Eigler, and A. J. Heinrich, *Measurement of fast electron spin relaxation times with atomic resolution*, Science **329**, 1628 (2010).
- [27] S. Baumann, W. Paul, T. Choi, C. P. Lutz, A. Ardavan, and A. J. Heinrich, *Electron paramagnetic resonance of individual atoms on a surface*, Science **350**, 417 (2015).
- [28] M. Leeuwenhoek, R. A. Norte, K. M. Bastiaans, D. Cho, I. Battisti, Y. M. Blanter, S. Gröblacher, and M. P. Allan, *Nanofabricated tips as a platform for double-tip and device based scanning tunneling microscopy*, Nanotechnology, *in press* (2019).
- [29] H. Grabert, *Dynamical coulomb blockade of tunnel junctions driven by alternating voltages*, Phys. Rev. B **92**, 245433 (2015).

3

Charge trapping and super-Poissonian noise centers in a cuprate superconductor

This chapter has been published as *Nature Physics* **14**, 1183 (2018)

The electronic properties of cuprate high temperature superconductors in their normal state are highly two-dimensional: transport along the crystal planes is perfectly metallic, but is insulating along the perpendicular c -axis direction. The ratio of the in-plane and perpendicular resistance can exceed 10^4 (refs [1–4]). This anisotropy was identified as one of the mysteries of the cuprates early on [5, 6], and although widely different proposals exist for its microscopic origin [7–9], there is little empirical information on the microscopic scale. In this chapter, we elucidate the properties of the insulating layers with a newly developed scanning noise spectroscopy technique that can spatially map the current and its time-resolved fluctuations. We discover atomic-scale noise centres that exhibit MHz current fluctuations 40 times the expectation from Poissonian noise, more than what has been observed in mesoscopic systems [10]. Such behaviour can happen only in highly polarizable insulators and represents strong evidence for trapping of charge in the charge reservoir layers. Our measurements suggest a picture of metallic layers separated by polarizable insulators within a three-dimensional superconducting state.

3.1. INTRODUCTION

The difference between metals and insulators is that in the former, additional charge equilibrates in femtoseconds while the latter can be statically charged. The coupling to the lattice is a necessary condition for the trapping of charge in insulators on macroscopic timescales since electrons by themselves are too quantum mechanical to localize. The trapped charge is stabilized by the formation of static, localized polarons involving a reconfiguration of the atomic lattice. Strongly polarizable insulators such as SrTiO₃ exemplify this process. Such trapping of charge on slow timescales has been conjectured as a cause of the anomalous, highly resistive c-axis transport in the cuprate high-temperature superconductors [7], competing with alternative proposals such as incoherent transport [11, 12]. We note that in these materials, bands structure theory predicts metallic transport along the c-axis due to the small but finite c-axis bandwidth of the order of 0.1 eV (ref. [13]). In this chapter, we present firm evidence that such charge trapping processes do occur in a superconducting cuprate material by measuring atomically resolved current fluctuations.

3.2. NOISE AS THE SIGNAL

Quite generally, fluctuations in time of a signal - the noise - can be a powerful diagnostic tool as they contain information not present in the mean value. It has historically allowed to distinguish between signals carried by particles and waves or between black body radiation and coherent radiation of a laser. More recently, noise spectroscopy has established itself as a standard method of investigating mesoscopic systems. This is usually done by looking at the noise spectral power, $S(\omega) = \langle \delta I(t) \delta I(t') \rangle$, where δI is the deviation of the current operator from the mean, and the averaging $\langle \rangle$ is both quantum mechanical and statistical. Examples where noise transport measurements led to novel insight include: the study of fractional charge [14], the doubling of charge in Andreev processes (see chapter 4), and the vanishing of noise in break junctions at the quantum conductance [15]. We have succeeded in bringing this technique to the atomic scale in the tunnelling regime (see chapter 2), and in this chapter we show how we use this technique to discover an unanticipated phenomenon when we applied it to a cuprate high temperature superconductor.

The flow of classical, uncorrelated charged particles between two leads is a purely Poissonian process. Its noise is independent of frequency (white) and proportional to the charge q and the flow I of the carriers, $S = 2q|I|$, as a direct consequence of the discreteness of the carriers [16]. In chapter 2 we defined the normalized noise $S_n = S/2e|I|$, which shows the deviation from the Poissonian noise, similar to the Fano factor. Thus $S_n = 1$ represents Poissonian noise, $S_n < 1$ and $S_n > 1$ refer to sub-Poissonian and super-Poissonian noise, respectively (Fig. 3.1.a-b). For an uncorre-

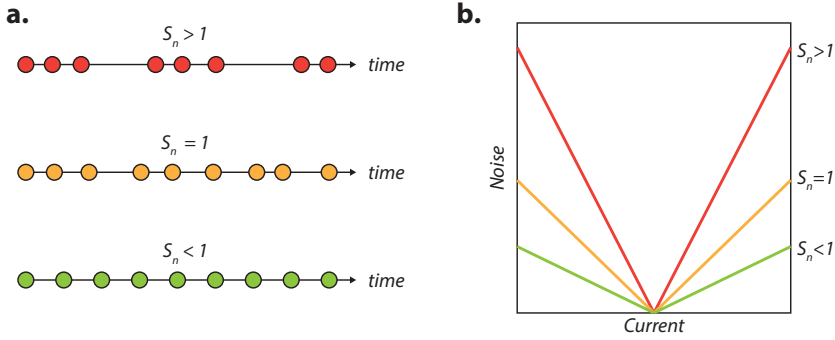


Figure 3.1: **Scanning tunnelling noise spectroscopy as a new diagnostic tool.** **a.** The classical flow of uncorrelated particles with charge q is a pure Poissonian process, $S = 2q|I|$. In the case of bunching, $S > 2q|I|$ and we refer to the noise as super-Poissonian (red). In the case of anti-bunching, $S < 2q|I|$ which is called sub-Poissonian (green). **b.** Noise S as a function of current in the cases described in (a).

lated electronic liquid, one expects $S_n = 1$; for an exotic, spatially inhomogeneous electronic liquid, this is a priori unclear. Importantly, in order to find $S_n > 1$, processes are required in the system on a frequency scale that fits into the slow (MHz) frequency window of the noise measurements. Another property of special relevance to our data is that such noise events may be completely invisible in the mean value of the current.

Our aim is thus to measure the fluctuations in the cuprates on the atomic scale. Bringing noise measurement to the tunnelling regime comes with unique challenges, as discussed in chapter 2, which prevented any atomic resolution shot noise measurement thus far. The central obstacle lies in the high impedance of the tunnelling junction, which is typically 0.3 GOhm to 10 GOhm. Together with the capacitance between tip and sample and the cable capacitance, the junction acts as low pass filter only allowing transmission of signals in the kHz range where $1/f$ noise and mechanical resonances dominate. Possible solutions include bootstrapping of an amplifier [17] or building an impedance matching circuit [18]. Matching a GOhm junction leads to considerable losses in the circuit. This is simplified when using the STM in point contact mode or in the low MOhm range [18, 19] or by using force-microscopy based methods [20], however, this increases interactions between tip and sample, making it more difficult to extrapolate the sample properties. Our goal is to perform noise measurements when in the tunnelling regime, with transparencies $\tau \sim 10^{-6}$. To accomplish this task, we build a new amplifier for scanning tunneling microscopy at MHz frequencies. The details of this amplification circuit that allows us to map out noise around 3 MHz with GOhm junction resistances are discussed in chapter 2.

3.3. DISCOVERY OF SUPER-POISSONIAN NOISE CENTERS

We choose to investigate cuprate high-temperature superconductors [21] first with this new scanning noise microscopy instrument, with the hope to find signs of the slow, glassy fluctuations associated with charge- and/or current loop order that have been claimed to show up in the noise [22–24]. We didn't observe any signs of these, but instead we found a surprise that we will explain in this chapter.

As a sample material, we decided to use the slightly overdoped bi-layer cuprate $(Pb, Bi)_2Sr_2CaCu_2O_{8+\delta}$ with $T_c = 79$ K. The Pb substitution for Bi has the advantage of suppressing the characteristic supermodulation seen in many Bi based cuprates, simplifying the interpretation and making higher voltage measurements possible. We cleave the samples in UHV at pressures below 10^{-10} mbar, and directly insert them into our STM head at 3.2 K. The single crystal sample is held at a constant voltage V_{bias} which drops over the GOhm junction between the tip and the uppermost CuO layer. The tunnelling process starts with electrons originating from the CuO layer which then tunnel through the SrO and Bi layers [25]. Tunnelling through these charge reservoir layers does not have much effect on the STM signal, except for some spatial filtering [25, 26]. Figure 3.2.a shows a topographic image revealing atomic resolution. The square Bi-lattice is clearly resolved with some bright protrusions induced by Pb-substitutions for Bi atoms (see appendix 3.B).

Upon recording the noise as a function of spatial location with atomic resolution at bias voltages of ± 0.1 eV we find homogeneously Poissonian noise, with no sign of the fluctuating orders. However, this changes dramatically when increasing the bias voltage, as shown in Figure 3.2.b-c. While most locations still exhibit Poissonian noise, a few atomic locations reveal striking enhancements of the noise. These super-Poissonian noise centers show noise values up to 40 times the expectation from Poissonian processes, more than anything that has been observed in mesoscopic systems [10]. We emphasise that the increase in noise is extremely localized, the width of the peaks in space being around 0.5 nm for most centers. The density of super-Poissonian noise centers is roughly 0.3% referenced to the number of Cu atoms, and they are evenly distributed throughout the sample.

3.4. NOISE SPECTROSCOPY ON NOISE CENTERS

A key insight comes from the energy dependence of the noise. Noise spectra are shown in Figure 3.2.d-f. Below a certain threshold, the noise in the tunnelling current is purely Poissonian, $S_n = 1$. But above around 1 eV or below around -650 meV the normalized noise rises rapidly. Surprisingly all noise centers appear to be highly asymmetric in energy: the noise enhancements at positive bias do not spatially correlate with the noise enhancement seen at negative energy. While different locations

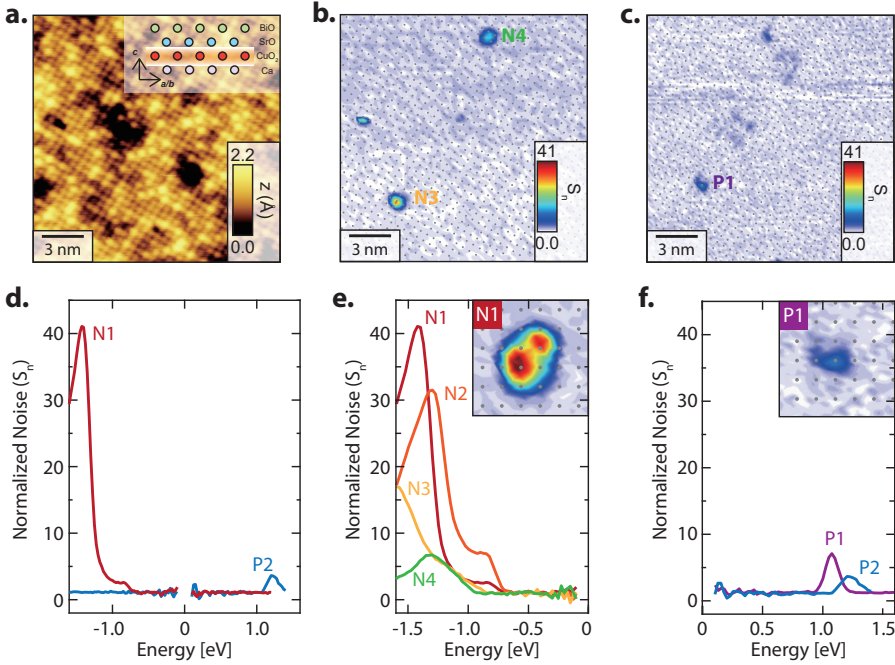


Figure 3.2: **Observation of super-Poissonian noise centers.** **a.** An atomic-resolution STM image of the BiO terminated overdoped bi-layer cuprate $(Pb,Bi)_2Sr_2CaCu_2O_{8+\delta}$ surface in a 18.3 nm field of view (sample bias $V_B = -0.10$ V, current $I_S = 0.1$ nA. Pb substitution for Bi are visible as bright protrusions. **b. c.** Spatially resolved, background line-subtracted, noise maps at -1.2 (b) and +1.1 (c) eV in the same field of view as figure 3.2a. The noise is normalized by the current simultaneously recorded at the same location. Most locations show homogeneous Poissonian noise ($S_n = 1$), but a few atomic locations reveal striking enhancements. N3, N4, and P1 indicate the negative and positive noise centers. Grey dots represent the Cu lattice sites. **d.** Representative noise spectra on the atomic locations that exhibit super-Poissonian noise show the strong asymmetry. **e. f.** Noise spectra on various positive and negative noise centers. Each inset shows the spatial distribution of the noise enhancements.

show different strengths of noise enhancement, the onset energy seems to be independent of the noise center, roughly -0.8 eV for the negative energy noise centers, and roughly +1 eV for the positive ones. This indicates a common mechanism and turns out to be an important diagnostic tool, as discussed below.

To understand these observations, it is worth taking a step back and look at engineered and natural systems that exhibit non-Poissonian noise, $S_n \neq 1$. In electronic systems this is most often sub-Poissonian noise [10, 12, 15, 17], usually due to sequential tunneling in quantum dots or Pauli exclusion effects. However, in the tunneling regime considered here ($\tau \sim 10^{-6}$), the latter are minimal. Super-Poissonian noise on the other hand is a much rarer occurrence, as it always has to include some sort of interaction [10]. Experimentally, super-Poissonian noise was first observed in semiconductor double-wells and later in quantum dots [27]. Examples of super-

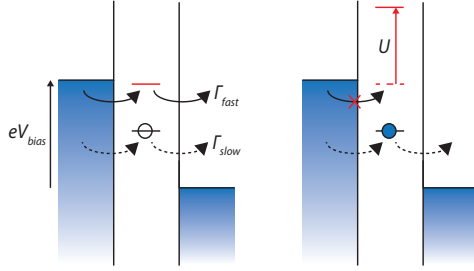


Figure 3.3: **Example of modulated transport by slow charge trapping processes.** Energy diagram of the co-tunnelling process via impurity states. Two tunnelling processes are possible; one of them has higher transmission rate than the other and dominates the total tunnelling current. Since they are strongly coupled by Coulomb energy (U), the tunnelling through the higher impurity level is prohibited by charge trapping of the lower one.

Poissonian noise include bi-stable systems that lead to random telegraph noise in the transport, and coupling to inelastic modes [28]. Our data allows us to exclude all these mechanisms as the observed noise is bias dependent and asymmetric.

3.5. MODULATED TRANSPORT BY POLARONIC CHARGE TRAPPING

Instead, our data suggests the following scenario known from double quantum dots, as illustrated in Fig. 3.3. Two tunneling processes are present, one fast, accounting for almost all the tunneling current, and one slow, acting as a switch for the first one. This switching mechanism is usually based on Coulomb interaction. For example, if the state of the slow process is occupied, it raises the energy level of the state necessary for the fast process and effectively blocks it, as shown in Fig. 3.3. This leads to an effective switching i.e. bunching of electrons that causes super-Poissonian noise. Such mechanisms have been discussed in detail for mesoscopic systems [10, 12, 29] and confirmed by experiments in double quantum dots [30]. We note that this scenario (i) predicts a clear threshold energy after which the noise increases, (ii) is asymmetric with respect to energy, (iii) is localized on the atomic scale. The key insight that follows from our observations is that some slow process is involved, i.e. a form of charge trapping that is known from strongly polarizable insulators but not from a metal.

One expects these noise centers to correspond with some form of polarons being localized at defects in the crystal lattice, in contrast to more itinerant polarons at other locations. To shed light on their precise nature, we searched for impurity states, following earlier work [31] but now taking fully normalized $dI/dV / (I/V)$ density of states maps over a large energy range to be able to differentiate impurity states that

overlap in energy. The energy dependent dI/dV / (I/V) maps reveal the spatial distribution of the different impurity states. Such states have been identified as (i) apical oxygen vacancies, (ii) Sr(Ca)-site impurities, (iii) interstitial oxygen dopants and (iv) Pb impurities. Figure 3.4 shows signatures of these specific states; details can be found in appendix 3.B.

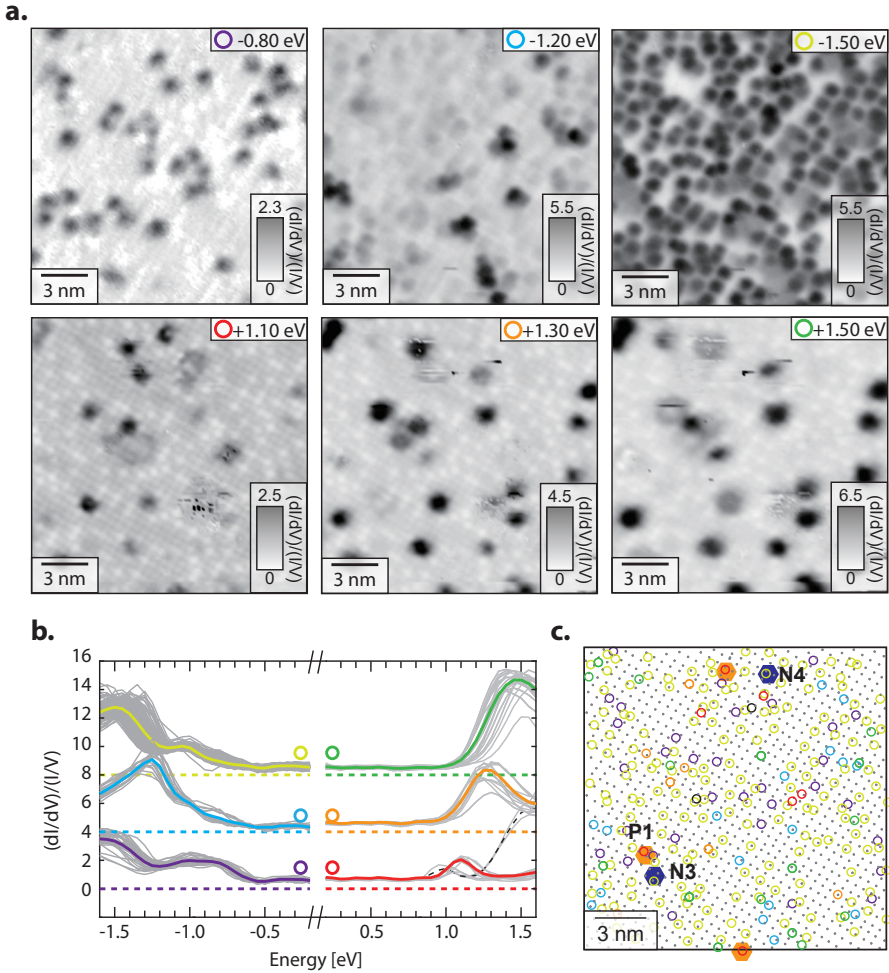


Figure 3.4: Bias-dependent conductance maps to identify impurity states and correlation with noise centers. **a.** Density of states at different energy levels: -1.5, -1.2, -0.8, +1.1, +1.3, and +1.5 eV. They were acquired in the same field of view as in Fig. 3.2a. The enhancement in normalized differential conductance (dI/dV / (I/V)) reveals the spatial distribution of various impurity states. **b.** Normalized differential conductance spectra taken on the different impurity states in Fig. 3.4a. The thick colored lines represent the average of the individual grey spectra. **c.** Overview of all impurity states in this field of view. Grey dots display the Cu-lattice. Various symbols corresponding to the different impurity states classified based on (a). The noise centers are indicated by the blue (negative) and red (positive) hexagons.

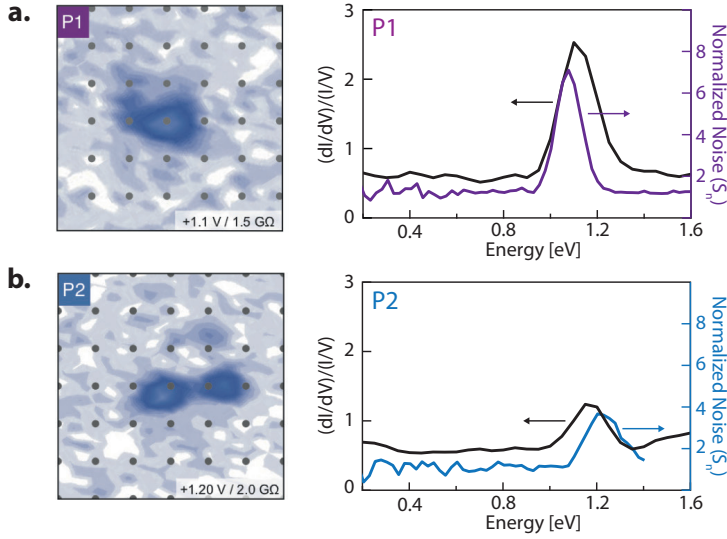


Figure 3.5: **Correspondence between the positive energy noise centers and the +1.1V impurity state.** **a.** Positive noise center P1 from Fig. 3.2. **b.** Positive noise center P2 from Fig. 3.2.

Most importantly, we find a clear correspondence between positive-energy noise centers and the +1.1 V impurity state, as shown in Fig. 3.4.c and 3.5. This impurity state has previously been identified as an apical oxygen vacancy [31] which, in the insulating oxygen materials, has various charge states stabilized by lattice distortions. This amounts to strong evidence for this signature to be associated with the charge trapping process. The positive noise centers show all this signature of an impurity state in the charge reservoir layer through which tunneling occurs but modulated by a slow charge trapping process. Surprisingly, we do not observe a clear correspondence between a specific type of impurity resonance and the site of the negative noise centers. This might be because the state is dark due to filtering mechanisms [26], or because of stronger coupling to the CuO layer.

3.6. CONCLUSIONS AND OUTLOOK

In this chapter we have presented direct evidence for the existence of slow charge trapping processes at defect sites in the form of the localized super-Poissonian noise signals. These are reminiscent of Coulombic impurities that occur generically in polarizable insulators, despite the three-dimensional superconducting state present in our samples. While the atomic centers with noise enhancement are sparse, they demonstrate the polaronic nature of charge carriers tunneling through the insulating layers. Apart from the noise centers, the polarons are likely itinerant to different

degrees; a situation that at present cannot be described by theory. The c-axis physics of the cuprates thus appears to be in a quite literal sense similar as to what is found in e.g. the aluminum oxide barriers employed for Josephson junctions: No coherent charge transport is possible for normal electrons, while the virtual tunnelling of Cooper pairs suffices for a coherent Josephson contact. In the cuprates, this is manifested of the form of the c-axis Josephson plasmons observed in the optical conductivity [32], emerging from a completely overdamped charge transport in the normal state [3]. The surprise is that apparently an oxidic layer that is only two atoms thick living in a metallic environment suffices for the polaronic trapping of charge.

3 The role of the ‘c-axis phenomena’ in the mechanism of high-temperature superconductivity is a long standing question [5, 6, 32], as is the unusual nature of the coupling of the polar insulator phonons to the electrons [5, 6, 8, 9, 33]. This acquired new impetus recently with the discovery that when a single layer of FeSe is removed from bulk and put on an polarizable insulator, the critical temperature increases by a factor of four [34], with evidence reported suggesting that the coupling to the polarizable insulating substrate may indeed play a critical role [35]. Further, interfaces of the polarizable insulators $SrTiO_3$ and $LaAlO_3$ host two dimensional superconductors with the highest T_c per charge density ratio [33]. So much is clear from our findings that even for the atomically thin insulating layers the polar electron-phonon interactions are of a severity sufficing to slow down electronic motions to macroscopic time scales. Although a great challenge for established theory, this conundrum deserves further close consideration.

APPENDICES

3.A. CORRELATION TO LOW-ENERGY FEATURES

We also correlated the atomic locations of the observed noise enhancement sites to the low-energy features known in Bi-based cuprate samples. Spectroscopic imaging STM has proven to be a very powerful tool for visualizing these low-energy features. By recording the dI/dV (proportional to the LDOS) spectrum over a spatially distributed grid of point we construct a three-dimensional dataset of the electronic structure as function of energy and the spatial coordinates. From this dataset we can then abstract the low-energy features like the superconducting gap magnitude (Fig. 3.6.b) or charge order arrangements in the electronic structure (Fig. 3.6.c). By recording an atomically resolved noise map (Fig. 3.6.a) in the same field of view at high energy we can correlate these low energy features of the sample to the noise enhancement centers we identified in this chapter. Visual comparison does not reveal any correlation between the noise enhancement sites and the low energy features (Fig. 3.6).

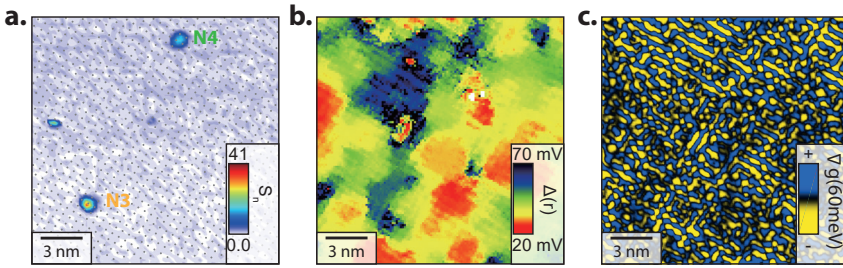


Figure 3.6: **Correlation of observed noise centers with low energy features.** **a.** Spatially resolved noise map at -1.2 eV at a 20 nm field of view. The negative noise centers exhibit enhancements of 10 times Poissonian noise and are indicated by the white circles. **b.** Spatial map of the superconducting gap magnitude over the sample surface in the same field of view as (a). The white circles indicate the locations of the negative noise centers. **c.** Laplacian of the ratio of the conduction maps at 52 meV and -52 meV in the same field of view, for better visualization of the atomic-scale arrangements of the spatial pattern.

3.B. DETERMINATION OF IMPURITY STATES

It is well known that there are several impurity states at high binding energy in $(Pb,Bi)_2Sr_2CaCu_2O_{8+\delta}$ samples [36]. Based on previous reports we expect that there are five kinds of impurities states, originating from type-A, type-B, apical oxygen vacancies [31], Pb^{2+} substitutions for Bi^{3+} , and Bi^{3+} substitutions for Sr^{2+} [37]. They are located at a binding energy of -1.5, -1.0, +1.0, -1.4, and +1.7 eV, respectively. Since all of the noise enhancement centers are observed at the high binding

energy regime, we want to identify all of impurity states in $(Pb, Bi)_2Sr_2CaCu_2O_{8+\delta}$ and check the correlation with the noise enhancement sites.

The conductance maps shown in Fig. 3.7 were acquired for the same field of view of noise maps shown in Fig. 3.2 using the typical spectroscopy technique. The setup conditions for the positive and negative bias maps are +1.60 and -1.60 V / 0.10 nA respectively. We used a lock-in modulation of 50 mV at 887 Hz. The STM images taken at the high bias have strong corrugations induced by the impurity states and thus the so called set-up effect is not negligible. To minimize these artifacts, we used the normalized local density of states by dividing dI/dV by I/V , which is a better measure of LDOS modulations in the present case. We thoroughly checked LDOS maps of all energy levels to identify all kinds of impurity states. There are six energy levels, -1.50, -1.20, -0.80, +1.10, +1.30, and +1.50 eV, which exhibit different impurity distributions. In Fig. 3.7.a, the colored circles on negative energy LDOS maps highlight local maxima. By overlaying the impurity maps for the filled states, we reveal that three separate impurities rarely coexist at the same site. Also all dI/dV spectra taken at these local maxima in Fig. 3.4.b show similar behavior. Therefore both the averaged spectra and the LDOS maps are usable for identifying the spectral feature of the impurity and their spatial distributions. From our analysis of the LDOS layers, we reveal that the LDOS map at -1.50 eV and the average spectra acquired at the local maxima are identical to the Pb impurity state. By comparison with previous studies, the impurity states around -1.20 and -0.80 eV are related with interstitial oxygen impurities. Previous theoretical study expected that one of interstitial oxygen impurities located close to *SrO* layer show a clear anti-correlation with inhomogeneous pseudogap due to hole-doping on *CuO₂* layer [38]. It was also experimentally shown in a high doped sample on the atomic scale [31]. However, we note that in our measurements the -1.2 eV state does not show a clear anti-correlation with the pseudogap, but a stronger correlation than the -0.8 eV impurity states. The latter are randomly distributed, the former tend to be located in the smaller pseudogap region. Therefore, we identify the -1.2 and -0.8 eV impurity states as the interstitial oxygen impurities around *SrO* and *BiO* layer, respectively.

To classify the impurity states at positive bias, we need one more procedure since different impurities exhibit similar contrast in the LDOS map at certain energies. The impurity map (Fig. 3.7.b) clearly shows several colored circles marked at the same atomic site. We sort collected spectra taken at the position according to the peak positions. According to our classifications shown in Fig. 3.4.b, there are at least 3 types of impurities which have a resonance peak above +0.9 eV. So far, only two impurities, apical oxygen vacancy and Bi^{3+} substitutions for Sr^{2+} , have been reported to have impurity states at the positive bias. The previous STS results [31] reported that the apical oxygen vacancies have the impurity state around +1.0 eV and exhibits a clear correlation with the pseudogap due to the local reduction of the hole concentration.

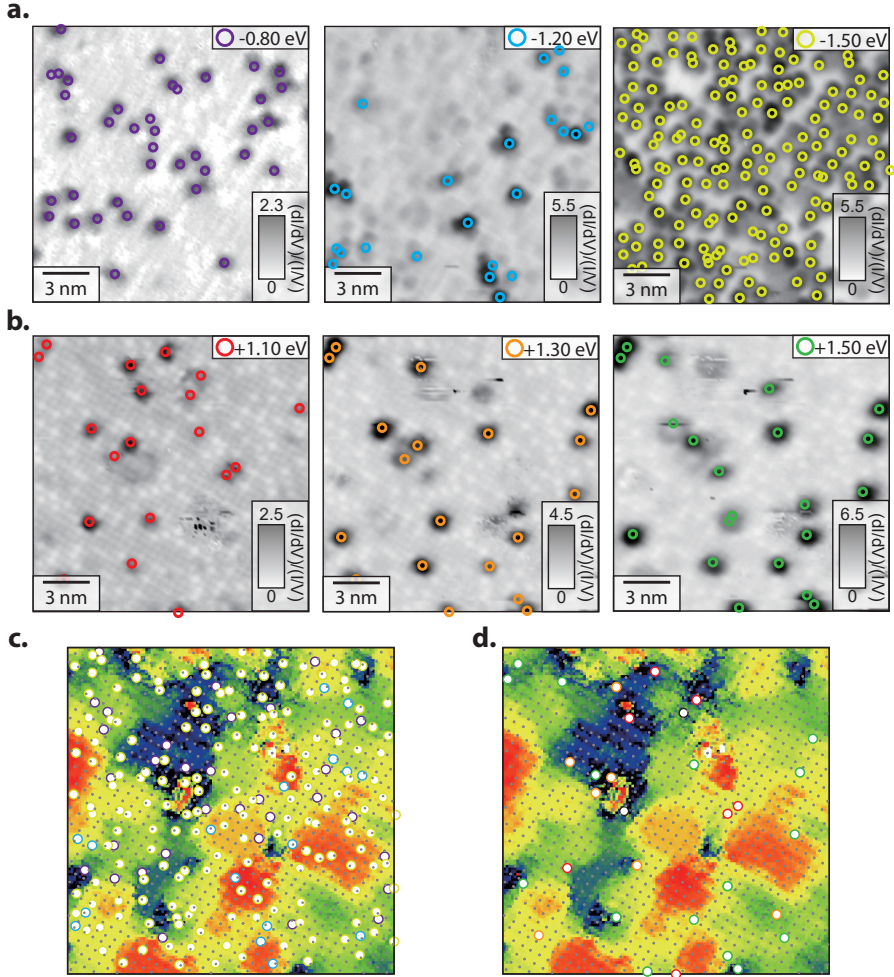


Figure 3.7: **Identification of impurity states.** **a and b.** The energy dependent normalized density of states maps $dI/dV/(I/V)$ maps for high negative and positive bias. The colored circles highlight the local maxima of the maps and correspond to the locations of impurities. The schematics are made by superimposing all of impurity markers. The dashed circles indicate the sites where the impurities coexist. **c and d.** Comparison between impurity site and inhomogeneous pseudogap. The impurity maps (same with Fig. 3.4) for negative (c) and positive (d) impurity state are superimposed on the pseudogap map.

This is consistent with one of our impurities whose spectra have a peak at 1.1 eV. The other two impurity states have similar atomic-scale feature (Fig. 3.4.a) and spectral shape (Fig. 3.4.b). We therefore identify these impurities as donor levels originated from Bi^{3+} substitutions for Sr^{2+} .

3.C. VARIOUS SUPER-POISSONIAN NOISE CENTERS

In this Fig. 3.8 we display the spatially resolved noise maps of the noise centers mentioned in Fig. 3.2.

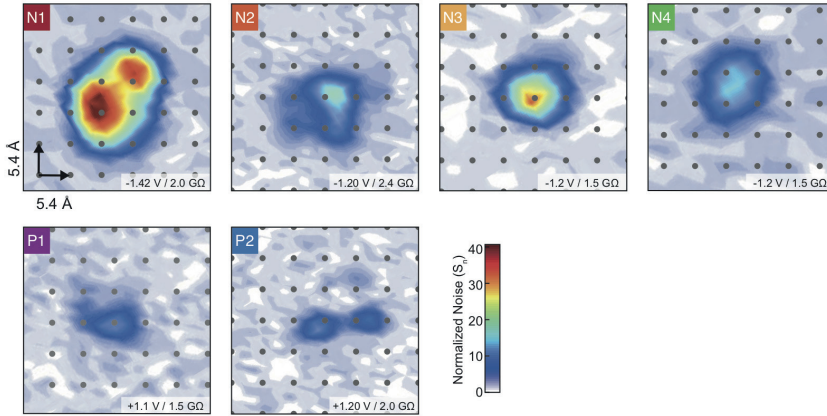


Figure 3.8: **Various super-Poissonian noise centers**, as referred to in Fig. 3.2. The grey dots display the Cu-lattice.

BIBLIOGRAPHY

- [1] T. Watanabe, T. Fujii, and A. Matsuda, *Anisotropic resistivities of precisely oxygen controlled single-crystal $\text{Bi}_2\text{Sr}_2\text{CaCu}_2\text{O}_{8+\delta}$: Systematic study on "spin gap" effect*, Phys. Rev. Lett. **79**, 2113 (1997).
- [2] G. Sordi, P. Semon, K. Haule, and A.-M. Tremblay, *c-axis resistivity, pseudogap, superconductivity, and Widom line in doped Mott insulators*, Phys. Rev. B **87**, 041101 (2013).
- [3] J. Levallois, M. Tran, D. Pouliot, C. Presura, L. Greene, J. Eckstein, J. Uccelli, E. Giannini, G. Gu, A. Leggett, and D. van der Marel, *Temperature-dependent ellipsometry measurements of partial Coulomb energy in superconducting cuprates*, Phys. Rev. X **6**, 031027 (2016).
- [4] J. H. Kim, H. Somal, M. Czyzyk, D. Van der Marel, A. Wittlin, A. Gerrits, V. Duijn, N. Hien, and A. Menovsky, *Strong damping of the c-axis plasmon in high- T_c cuprate superconductors*, Physica C: Superconductivity **247**, 297 (1995).
- [5] P. Anderson, *Experimental constraints on the theory of high- T_c superconductivity*, Science **256**, 1526 (1992).
- [6] A. Leggett, *A "midinfrared" scenario for cuprate superconductivity*, PNAS **96**, 8365 (1999).
- [7] D. Gutman and D. Maslov, *Anomalous c-axis transport in layered metals*, Phys. Rev. Lett. **99**, 196602 (2007).
- [8] S. Johnston, F. Vernay, B. Moritz, Z.-X. Shen, N. Nagaosa, J. Zaanen, and T. Devereaux, *Systematic study of electron-phonon coupling to oxygen modes across the cuprates*, Phys. Rev. B **82**, 064513 (2010).
- [9] W. Meevasana, T. Devereaux, N. Nagaosa, Z.-X. Shen, and J. Zaanen, *Calculation of overdamped c-axis charge dynamics and the coupling to polar phonons in cuprate superconductors*, Phys. Rev. B **74**, 174524 (2006).
- [10] Y. Blanter, *Recent advances in studies of current noise*. in *CFN Lectures on Functional Nanostructures-Volume 2* (Springer, Berlin, Heidelberg, 2011).
- [11] P. W. Anderson and Z. Zou, *"normal" tunneling and "normal" transport: Diagnostics for the resonating-valence-bond state*, Phys. Rev. Lett. **60**, 132 (1988).
- [12] P. Moses and R. H. McKenzie, *Comparison of coherent and weakly incoherent transport models for the interlayer magnetoresistance of layered Fermi liquids*, Phys. Rev. B **60**, 7998 (1999).

- [13] R. S. Markiewicz, S. Sahrakorpi, M. Lindroos, H. Lin, and A. Bansil, *One-band tight-binding model parametrization of the high- T_c cuprates including the effect of k_z dispersion*, Phys. Rev. B **72**, 054519 (2005).
- [14] R. De-Picciotto, M. Reznikov, M. Heiblum, V. Umansky, G. Bunin, and D. Mahalu, *Direct observation of a fractional charge*, Nature **389**, 162 (1997).
- [15] H. Van den Brom and J. Van Ruitenbeek, *Quantum suppression of shot noise in atom-size metallic contacts*, Phys. Rev. Lett. **82**, 1526 (1999).
- [16] Y. M. Blanter and M. Büttiker, *Shot noise in mesoscopic conductors*, Physics Reports **336**, 1 (2000).
- [17] H. Birk, M. De Jong, and C. Schönenberger, *Shot-noise suppression in the single-electron tunneling regime*, Phys. Rev. Lett. **75**, 1610 (1995).
- [18] U. Kemiktarak, T. Ndukum, K. Schwab, and K. Ekinci, *Radio-frequency scanning tunnelling microscopy*, Nature **450**, 85 (2007).
- [19] A. Burtzloff, A. Weismann, M. Brandbyge, and R. Berndt, *Shot noise as a probe of spin-polarized transport through single atoms*, Phys. Rev. Lett. **114**, 016602 (2015).
- [20] M. G. Sung, H. Lee, K. Heo, K.-E. Byun, T. Kim, D. H. Seo, S. Seo, and S. Hong, *Scanning noise microscopy on graphene devices*, ACS Nano **5**, 8620 (2011).
- [21] B. Keimer, S. A. Kivelson, M. R. Norman, S. Uchida, and J. Zaanen, *From quantum matter to high-temperature superconductivity in copper oxides*, Nature **518**, 179 (2015).
- [22] E. W. Carlson, K. A. Dahmen, E. Fradkin, and S. A. Kivelson, *Hysteresis and noise from electronic nematicity in high-temperature superconductors*, Phys. Rev. Lett. **96**, 097003 (2006).
- [23] S. A. Kivelson, I. P. Bindloss, E. Fradkin, V. Oganesyan, J. M. Tranquada, A. Kapitulnik, and C. Howald, *How to detect fluctuating stripes in the high-temperature superconductors*, Rev. Mod. Phys. **75**, 1201 (2003).
- [24] J. Zhang, Z. Ding, C. Tan, K. Huang, O. O. Bernal, P.-C. Ho, G. D. Morris, A. D. Hillier, P. K. Biswas, S. P. Cottrell, H. Xiang, X. Yao, D. E. MacLaughlin, and L. Shu, *Discovery of slow magnetic fluctuations and critical slowing down in the pseudogap phase of yba_2cu_3oy* , Science Advances **4** (2018).
- [25] P. Choubey, A. Kreisel, T. Berlijn, B. M. Andersen, and P. J. Hirschfeld, *Universality of scanning tunneling microscopy in cuprate superconductors*, Phys. Rev. B **96**, 174523 (2017).

- [26] I. Martin, A. V. Balatsky, and J. Zaanen, *Impurity states and interlayer tunneling in high temperature superconductors*, Phys. Rev. Lett. **88**, 097003 (2002).
- [27] E. Onac, F. Balestro, B. Trauzettel, C. Lodewijk, and L. Kouwenhoven, *Shot-noise detection in a carbon nanotube quantum dot*, Phys. Rev. Lett. **96**, 026803 (2006).
- [28] A. Thielmann, M. H. Hettler, J. König, and G. Schön, *Cotunneling current and shot noise in quantum dots*, Phys. Rev. Lett. **95**, 146806 (2005).
- [29] S. S. Safonov, A. K. Savchenko, D. A. Bagrets, O. N. Jouravlev, Y. V. Nazarov, E. H. Linfield, and D. A. Ritchie, *Enhanced shot noise in resonant tunneling via interacting localized states*, Phys. Rev. Lett. **91**, 136801 (2003).
- [30] S. Gustavsson, R. Leturcq, B. Simović, R. Schleser, P. Studerus, T. Ihn, K. Ensslin, D. C. Driscoll, and A. C. Gossard, *Counting statistics and super-poissonian noise in a quantum dot: Time-resolved measurements of electron transport*, Phys. Rev. B **74**, 195305 (2006).
- [31] I. Zeljkovic, Z. Xu, J. Wen, G. Gu, R. S. Markiewicz, and J. E. Hoffman, *Imaging the impact of single oxygen atoms on superconducting $\text{Bi}_2\text{Te}_{2-x}\text{Se}_{x+1}$* , Science **337**, 320 (2012).
- [32] A. Tsvetkov, D. Van der Marel, K. Moler, J. Kirtley, J. De Boer, A. Meetsma, Z. Ren, N. Kolesnikov, D. Dulic, A. Damascelli, M. Gruninger, J. Schutzman, J. Van der Eb, H. Somal, and J. Wang, *Global and local measures of the intrinsic josephson coupling in $\text{Ti}_2\text{Ba}_2\text{CuO}_6$ as a test of the interlayer tunnelling model*, Nature **395**, 360 (1998).
- [33] N. Reyren, S. Thiel, A. D. Caviglia, L. F. Kourkoutis, G. Hammerl, C. Richter, C. W. Schneider, T. Kopp, A.-S. Rüetschi, D. Jaccard, M. Gabay, D. A. Muller, J.-M. Triscone, and J. Mannhart, *Superconducting Interfaces Between Insulating Oxides*, Science **317**, 1196 (2007).
- [34] Q.-Y. Wang, Z. Li, W.-H. Zhang, Z.-C. Zhang, J.-S. Zhang, W. Li, H. Ding, Y.-B. Ou, P. Deng, K. Chang, J. Wen, C.-L. Song, K. He, J.-F. Jia, S.-H. Ji, Y.-Y. Wang, L.-L. Wang, X. Chen, X.-C. Ma, and Q.-K. Xue, *Interface-Induced High-Temperature Superconductivity in Single Unit-Cell FeSe Films on SrTiO_3* , Chinese Physics Letters **29**, 037402 (2012).
- [35] J. Lee, F. Schmitt, R. Moore, S. Johnston, Y.-T. Cui, W. Li, M. Yi, Z. Liu, M. Hashimoto, Y. Zhang, D. Lu, T. Devereaux, D.-H. Lee, and Z.-X. Shen, *Interfacial mode coupling as the origin of the enhancement of T_c in FeSe films on SrTiO_3* , Nature **515**, 245 (2014).
- [36] I. Zeljkovic and J. E. Hoffman, *Interplay of chemical disorder and electronic inhomogeneity in unconventional superconductors*, Physical Chemistry Chemical Physics **15**, 13462 (2013).

- [37] G. Kinoda, H. Mashima, K. Shimizu, J. Shimoyama, K. Kishio, and T. Hasegawa, *Direct determination of localized impurity levels located in the blocking layers of $\text{Bi}_2\text{Sr}_2\text{CaCu}_2\text{O}_y$ using scanning tunneling microscopy/spectroscopy*, Phys. Rev. B **71**, 020502 (2005).
- [38] S. Zhou, H. Ding, and Z. Wang, *Correlating off-stoichiometric doping and nanoscale electronic inhomogeneity in the high- T_c superconductor $\text{Bi}_2\text{Sr}_2\text{CaCu}_2\text{O}_{8+\delta}$* , Phys. Rev. Lett. **98**, 076401 (2007).

4

Imaging doubled shot noise in a Josephson Scanning Tunneling Microscope

This chapter has been published as *Physical Review B* **100**, 104506 (2019)

We have imaged the current noise with atomic resolution in a Josephson scanning tunneling microscope with a Pb-Pb junction. By measuring the current noise as a function of applied bias, we reveal the change from single electron tunneling above the superconducting gap energy to double electron charge transfer below the gap energy when Andreev processes become dominant. Our spatially resolved noise maps show that this doubling occurs homogeneously on the surface, and also on impurity locations, demonstrating that indeed the charge pairing is not influenced by disruptions in the superconductor smaller than the superconducting coherence length.

4.1. INTRODUCTION

The coupling between two macroscopic superconducting electrodes through an insulating layer can lead to a dissipationless current called the Josephson supercurrent. The critical current I_C is the maximal supercurrent that the junction can sustain; it is related to the individual superconducting order parameters in both electrodes, as well as their coupling [1]. In the zero-voltage limit, this supercurrent is carried by paired electrons (Cooper pairs), carrying twice the electron charge e . Applying a bias voltage V_B larger than twice the pair-breaking gap energy Δ , $eV_B > 2\Delta$, over the junction results in a normal current carried predominantly by quasiparticles with a single-electron charge (Fig. 4.1.b). In the energy range below the gap edge, only the so-called Andreev reflection processes can transport the quasiparticles across the junction by reflecting particles carrying the opposite charge. These processes lead to the effective charge transfer of multiple electron charges [2–4]. In the energy range $\Delta < eV_B < 2\Delta$, the dominant process is a single Andreev reflection leading to the transfer of effectively double the electron charge, as illustrated in Fig. 4.1.c.

One cannot tell from the time-averaged value of the current whether it is carried by multiple integers of charge, but this becomes apparent when measuring the fluctuations of the current, or in other words, the current noise [5–10]. In general, the noise originating from the flow of uncorrelated particles in a tunneling junction (shot noise) is a purely Poissonian process. The current noise power S_I is then proportional to the charge q and the current I of the carriers, $S = 2q|I|$ [5]. At lower bias voltages, when Andreev processes become relevant, the transferred charge in a Josephson junction can effectively double and therefore the noise is also expected to be two times the Poissonian value [11, 12]. Spectroscopic noise measurements in mesoscopic systems have revealed such noise signatures of multiple electron charge transport in superconducting junctions associated with Andreev processes [6–10], as well as fractional charges in quantum hall systems [13, 14] and the vanishing of shot noise at atomic-scale point contacts [15–17].

In this chapter we perform such noise spectroscopy measurements spatially resolved with atomic resolution in a Josephson scanning tunneling microscope. We use our recently developed scanning tunneling noise microscopy (STNM) technique to spatially resolve the current and its time-resolved fluctuations simultaneously with atomic resolution, as discussed in chapters 2 and 3 [18]. We first demonstrate the current noise doubling from single to double charge transfer below the gap edge in a junction between a superconducting Pb tip and a Pb(111) sample. We then visualize this noise enhancement by spatially mapping the effective charge transfer over the sample surface. We show that it is homogeneous over the sample surface, also including impurity locations, demonstrating that the charge pairing is not influenced by disruptions smaller than the coherence length ($\xi \sim 80$ nm in Pb).

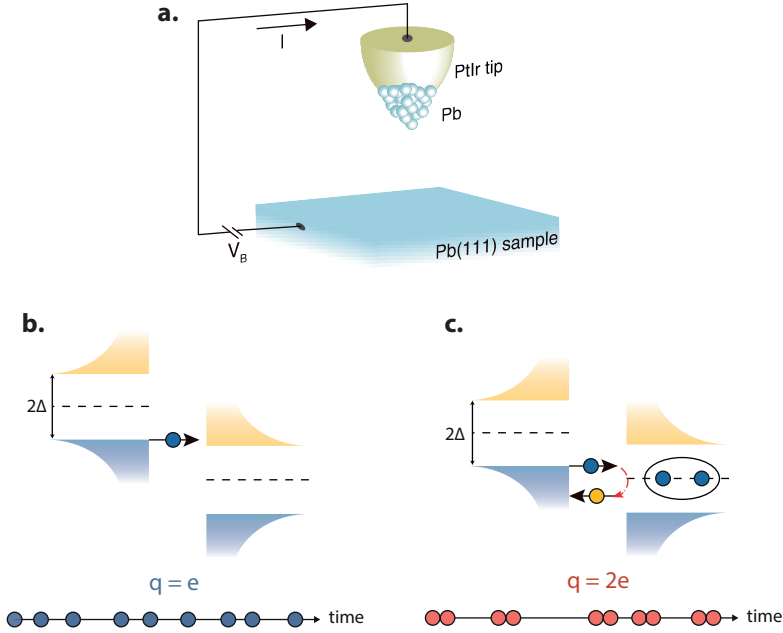


Figure 4.1: **a.** Schematics of a Josephson scanning tunneling microscope. The SIS junction consists of a Pb-coated tip ($\Delta_{\text{tip}} = 1.31$ meV) and an atomically flat Pb(111) surface ($\Delta_{\text{sample}} = 1.35$ meV) separated by a thin vacuum barrier. **b.** Normal current carried by quasiparticles transferring single electron charge. The characteristic density of states of both superconducting electrodes are shown, with filled and empty states denoted by blue and yellow separated by the pair-breaking gap $2\Delta_{\text{tip/sample}}$. **c.** Andreev reflection process. An electron transfers a Cooper-pair into the superconducting condensate by reflecting a hole in the opposite direction, effectively transferring $2e$ charge.

4.2. EXPERIMENTAL SETUP

A schematic of our setup is shown in Fig. 4.1, where a superconducting STM tip is brought in tunneling contact with a superconducting sample to form a superconductor-insulator-superconductor (SIS) junction. We create this junction in our modified low-temperature (2.2 K) Unisoku USM-1500 STM setup. First, the Pb(111) single crystal surface is cleaned by repetitive cycles of Ar^+ sputtering at 1 kV with an Ar pressure of 5.0×10^{-5} mbar (background pressure $< 1.0 \times 10^{-10}$ mbar) and annealing. We then push the mechanically grinded PtIr tip into the surface to decorate it with a superconducting cluster of Pb atoms until we obtain a SIS junction [19–21].

4.3. JOSEPHSON TUNNELING SPECTROSCOPY

To demonstrate the high quality of the SIS junction in our setup, we display its distinct spectroscopic signatures for varying normal state resistance R_N (by adjusting the bias and current setpoint) in Fig. 4.2. The first signature is visible in the single particle channel, where quasiparticles with energies larger than the pair-breaking gap transfer the charge. The tunneling spectra in Fig. 4.2.a show sharp coherence peaks, which are located at energies equal to the sum of both superconducting gaps of the tip and the sample $2\Delta = \Delta_{\text{tip}} + \Delta_{\text{sample}} = 2.66$ meV. The clear U-shaped gap at 13.6 M Ω can be used as a benchmark for bulk-like superconducting properties of the tip and, also considering the low conductance, indicates that only a single transmission channel is present [22]. Due to the sharp density of states of the superconducting tip, the spectroscopic features are much sharper than one would expect from conventional thermal broadening [19]. We can fit these spectra with a modified phenomenological gap equation [23] to extract an effective electron temperature of 2.2 K, which is similar to the measured phonon temperature, as electron-phonon coupling is still rather efficient at these temperatures.

The next signature stems from Andreev processes that are visible at lower junction resistances. These lead to a sub-gap structure with humps in the differential conductance. Specifically, at energies below $2\Delta/n$, Andreev processes of order n become possible with the relative probability τ^{n+1} , where τ is the transparency of the junction. A small hump, indicated by the black arrows in Fig. 4.2.a-b, is visible in the differential conductance when the order of the lowest-allowed Andreev reflection process changes [2, 3].

The spectroscopic signatures related to the Josephson supercurrent in the junction are observed in the differential conductance at energies close to the Fermi level E_F : a peak that is enhanced with decreasing R_N , and small oscillations around the central peak (Fig. 4.2.b). To understand these, we first survey the energy scales in our setup. The capacitive energy E_C and the thermal energy are larger than the Josephson energy E_J . Therefore, the environmental impedance becomes a relevant quantity, and thermal phase fluctuations across the junction govern the Josephson current, shifting the maximum current to a non-zero bias [24]. Close to the Fermi energy E_F we access the Cooper-pair channel associated with the coupling between the two superconducting condensates. The prominent peak at E_F in Fig. 4.2.b, corresponding to the local maximum in the current in Fig. 4.2.c, originates from the phase fluctuating Josephson current [21, 24]. Both the maximum Josephson current and the differential conductance at zero bias are proportional to the square of the intrinsic critical current of the Josephson junction. The critical currents we obtain for these spectra show a linear relation with R_N and are consistent with the Ambegaokar-Baratoff formula (Fig. 4.2.d) [25]. We also note the small oscillating features in both the con-

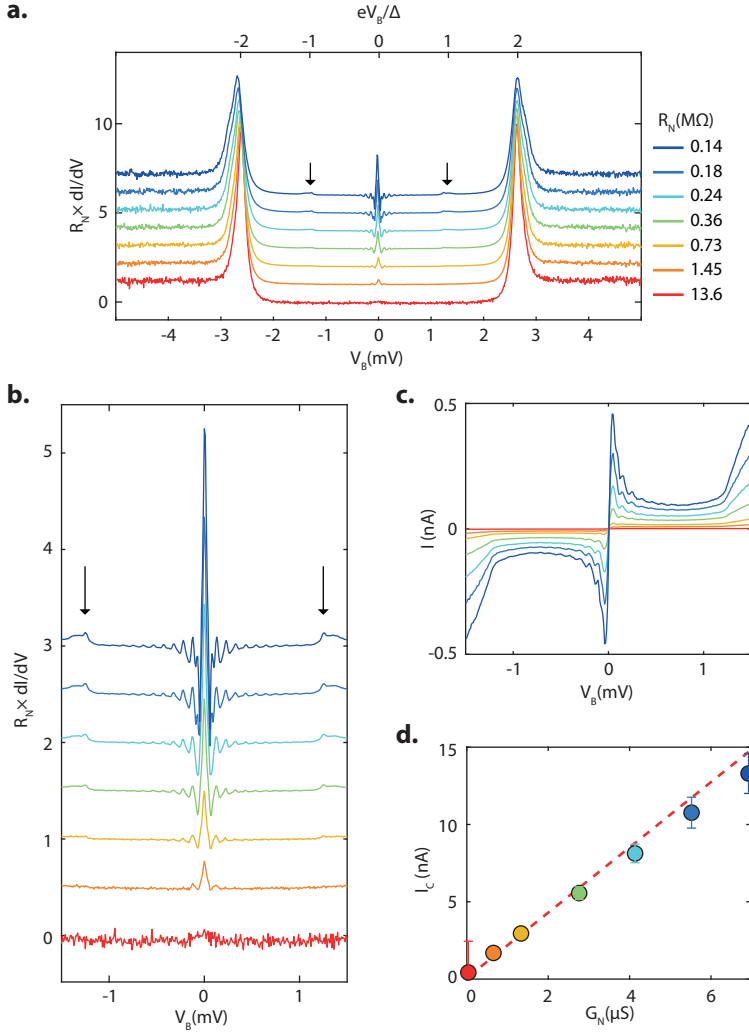


Figure 4.2: **a.** Differential conductance spectra multiplied by the normal state resistance acquired for various setup conditions. Sharp coherence peaks can be seen at $eV_B/\Delta = \pm 2$. The increasing conductance around $eV_B/\Delta = \pm 1$ (arrows) with various normal state resistance indicates the presence of Andreev processes. Curves are offset for clarity. **b.** Zoom in at the low energy features in the differential conductance spectra. The prominent peak at the Fermi energy that rises with decreasing R_N is a signature of the Josephson supercurrent. Curves are offset for clarity. **c.** Current-voltage characteristics acquired simultaneously with the spectra shown in panel (b). **d.** Critical supercurrent of the junction (points) and its quantitative agreement with the Ambegaokar-Baratoff formula (red dashed line).

ductance and the current spectra stretching far out to ~ 1 meV, originating from coupling of the junction with its dissipative electromagnetic environment, previously explained by a tip-induced antenna mode [21, 26].

4.4. NOISE SPECTROSCOPY

We now come to the central part of this chapter, where we visualize the doubling of the current noise in this scanning Josephson junction using STNM. The central challenge for measuring current noise in a conventional scanning tunneling microscope (STM) is that the temporal resolution is generally limited to only a few kHz, because the combination of the high impedance ($\sim \text{G}\Omega$) tunnel junction and capacitance of the interfacing cables (~ 100 pF) form an inherent low-pass filter. As a consequence, STM usually provides a static, time-averaged picture, lacking information about possible dynamical phenomena in the junction [27], especially when requiring atomic-resolution scanning.

Our noise measurement apparatus, described in detail in chapter 2 [18], builds upon earlier high-frequency STMs [28–30] but is based on a superconducting LC resonating circuit that is connected to the Josephson junction, as illustrated in Fig. 4.3.a. Current fluctuations in the junction are converted into voltage fluctuations at resonance of the LC circuit, which are then amplified by the custom-built cryogenic amplifier [31] into a 50Ω line. To illustrate how we extract the magnitude of the current noise in the junction, we plot several curves of the measured power spectral density in Fig. 4.3.b for various bias voltages. To mitigate the effect of a non-linear differential conductance on the effective resonator impedance, one needs to separate the measured signal into the noise components [18, 32]. The total measured voltage noise is

$$S_V^{\text{meas}}(\omega, V) = G^2 |Z_{\text{res}}|^2 S_I, \quad (4.1)$$

where G is the total gain of the amplification chain, Z_{res} the impedance of the resonating circuit and S_I the total current noise in the circuit. The strong influence of the highly non-linear differential conductance on the total impedance of the resonator is also illustrated in Fig. 4.3.b, where the clear change of the measured power spectral density for varying bias voltage is due to the simultaneously changing impedance of the resonator and the amplitude of the noise as a function of bias.

After correcting for the non-linear differential conductance, the total current noise equals

$$S_I(I) = 2q|I| \coth \frac{qV}{2k_B T} + \frac{4k_B T}{|Z_{\text{res}}|} + S_{\text{amp}}, \quad (4.2)$$

where q is the effective charge, T is the effective temperature and S_{amp} is the input noise of the amplifier. The first term represents the shot noise in the junction and the

second term represents the thermal noise. The black curves in Fig. 4.3.b represent fitting of $S_V^{\text{meas}}(\omega, V)$ to the measured noise spectra, which we then use to obtain a value for the effective charge q transferred across the junction.

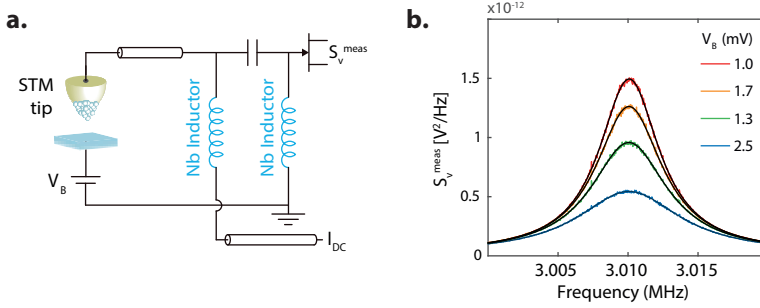


Figure 4.3: **a.** Measurement circuit of STNM, which allows for spatial mapping of the current fluctuations with atomic resolution. Superconducting niobium ($T_C = 9.2$ K, indicated in blue) inductors are used for the resonating circuit. **b.** Power spectral density of the resonator circuit, in a small bandwidth around the resonance frequency. The different spectra represent various values of the applied bias to the Josephson junction. Measured data are plotted by the colored lines, the black curves correspond to a circuit diagram fit via Eq. 4.1.

4.5. DOUBLED NOISE DUE TO ANDREEV REFLECTIONS

We first measure the current noise as a function of energy at a single location. Figure 4.4.a shows the measured current noise power as a function of bias, with the zero-current noise subtracted to remove the thermal noise component and input noise of the amplifier: $S_I(I) - S_I(0)$. The dashed lines indicate the theoretically calculated shot-noise curves as described above, for effective charge e (blue) and $2e$ (red). At large bias voltage the experimental data follows the noise for single-electron tunneling. However, the current noise clearly doubles from e to $2e$ at the coherence peak energy $eV_B/\Delta = \pm 2$. We obtain the effective charge transferred by dividing the measured noise power by the full Poissonian noise $S = 2e|I| \coth \frac{eV}{2k_B T}$ (Fig. 4.4.b). Note that, since we keep the junction resistance R_J constant, the transmission of the junction is changing when the bias voltage is reduced, leading to a correction of the effective q by $(1 - \tau_n)$ with $\tau_n \sim (G_0 R_J)^{-1/n}$ for small transparencies. The correction, applied to the data points in Fig. 4.4.b is smaller than the scatter of our data points, due to the low transparency of our junction. The clear step in effective charge as a function of applied bias at the gap energy demonstrates that the tunneling current is now effectively carried by double charge quanta due to Andreev reflection processes. This is well consistent with theoretical descriptions [2–4, 11, 12] and experimental observations in mesoscopic devices, where Andreev reflections lead to enhanced noise in nanofabricated SIS junctions [9, 10] and short diffusive normal metal – supercon-

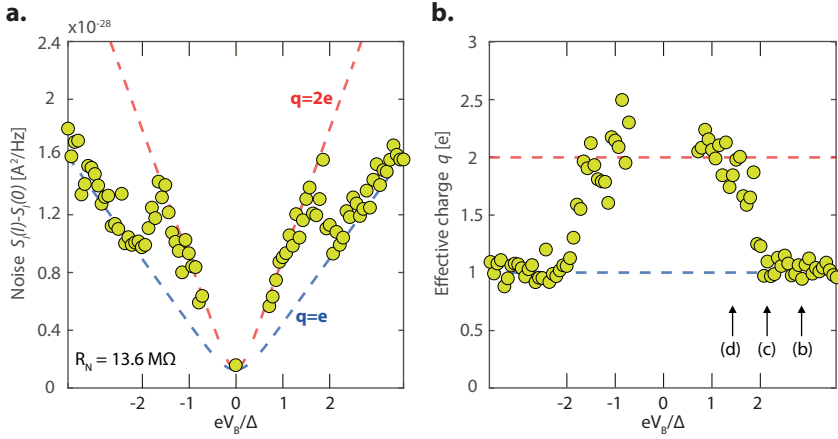


Figure 4.4: **a.** Measured current noise for varying bias voltage acquired at a random location in Fig. 4.5.a, maintaining a constant junction resistance $R_J = 13.6 \text{ M}\Omega$. The dashed lines represent the calculated values for an effective charge equals e (blue) and $2e$ (red). **b.** Effective charge transferred through the Josephson junction for varying bias. The data points represent $q = (S(I) - S(0))/2e|I|$, similar to the Fano factor. Dashed lines indicate $q = e$ and $q = 2e$ lines. The black arrows indicate the bias voltage of the spatially resolved noise maps of Fig. 4.5.

ductor contacts [6, 8], but have never been seen in a STM setup or at such low transparencies. In the present project, we use transparencies of $\tau \sim 10^{-3} - 10^{-4}$ leading to a single channel of transmission, whereas in mesoscopic devices usually multiple channels of $\tau \sim 10^{-1}$ are involved.

4.6. SPATIALLY RESOLVED NOISE DOUBLING

Finally, we apply the spatial mapping capabilities of our STNM setup to resolve this doubling of the noise over the sample surface with atomic-scale resolution. Figure 4.5.a shows a topographic image of the Pb(111) surface in a 12.5 nm field of view, including a hexagonal shaped impurity previously identified as a sub-surface Ar nanocavity [33]. Next to locally reducing the scattering length, this nanocavity located beneath the surface also vertically and laterally confines charge carriers on a few nanometer length scale. We performed the noise-spectroscopy measurement in the same field of view by scanning the tip over the surface while simultaneously measuring the current noise. The spatially resolved noise maps at various bias voltages shown in Fig. 4.5.b-d, exhibit a homogeneous contrast at energies above the pair-breaking gap energy, as is expected for transfer of uncorrelated particles. Below the superconducting gap energy we again observe homogeneous contrast, but now at an elevated value of the noise power around an effective charge equal to $2e$. While we observe a strong contrast in the topography, these spatially resolved noise maps

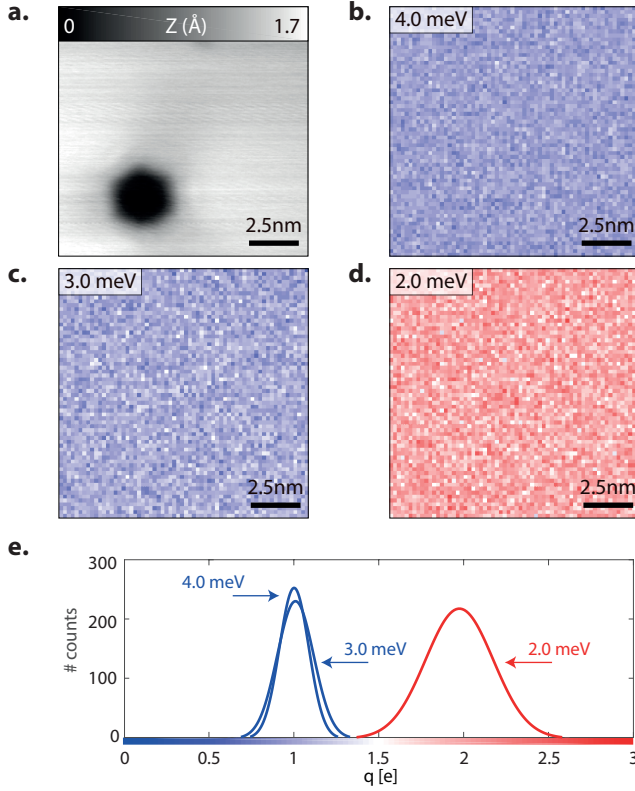


Figure 4.5: **a.** Topograph of 12,5 nm field of view on the Pb(111) surface, including a hexagonal shaped Ar nanocavity. **b-d.** Spatial imaging of the effective charge for various bias voltages measured in feedback with a normal state resistance $R_N = 13.6 \text{ M}\Omega$. The spatially resolved noise maps show homogeneous $q = e$ noise for $eV_B > 2\Delta$ (4.0 (b) and 3.0 (c) meV) and $q = 2e$ noise for $eV_B < 2\Delta$ (2.0 meV (d)). **e.** Distribution of the effective charge for each spatial noise map, obtained by fitting a normal distribution to the histogram of each panel.

show that the doubling occurs homogeneously over the surface, also on the location of the nanocavity. This demonstrates that disruptions in the superfluid, due to local confinement of the charge carriers or scattering on the nanocavity [33], on length scales smaller than the superconducting coherence length ($\xi \sim 80 \text{ nm}$ in Pb), do not influence the charge pairing, since the spatially resolved current noise is unaffected. This finding is in line with STM experiments showing that Andreev reflections are virtually unaffected by small diameter molecules [34].

4.7. CONCLUSIONS AND OUTLOOK

In this chapter we measured doubled shot noise caused by Andreev reflections in a Josephson scanning tunneling microscope using noise spectroscopy measurements. We spatially resolved this doubling with atomic-scale resolution on the surface of the conventional superconductor Pb(111). The ability to spatially resolve the charge dynamics with such precision opens new paths for investigating many-body correlation effects in quantum materials.

As we have seen in chapter 3, scanning noise spectroscopy led to a novel understanding of cuprate high-temperature superconductors, where the discovery of charge trapping dynamics suggests a picture of copper-oxide planes separated by thin insulating layers within the three-dimensional superconducting state [35, 36]. But the list of potential for STNM is a continuously growing one; we believe that atomically resolved noise measurements will also reveal new insight in fluctuating stripe order [37] and pre-formed pairing in the pseudogap regime [38, 39]. One could imagine a similar experiment like the one presented in this chapter being performed on a cuprate high-temperature superconductor. If the sample would be in the superconducting phase one would expect to measure similar noise doubling as for the Pb-Pb junction in this chapter, but then with one of the gaps Δ_{sample} shifted to the relative value of the cuprate superconductor. The real interesting question would be what will happen if one would then tune the cuprate sample into the pseudogap regime. This phase is sometimes considered to be a precursor phase of superconductivity, hosting pre-formed pairs [39, 40]. A direct measurement of the effective charge of the carries would help to resolve the real nature of this phase.

Further examples of potential experiments where our scanning noise technique could lead to new insights include Kondo effects in heavy fermion systems, where the shot noise exhibits a characteristic bias dependence arising from Kondo screening, depending on the ratio of the different tunneling amplitudes [41, 42]. Finally, similar noise investigations as presented in this chapter could also reveal signatures of Majorana zero-modes in one-dimensional chains of atoms on a superconducting surface [43, 44].

BIBLIOGRAPHY

- [1] B. D. Josephson, *Possible new effects in superconductive tunnelling*, Phys. Lett. **1**, 251 (1963).
- [2] G. E. Blonder, M. Tinkham, and T. M. Klapwijk, *Transition from metallic to tunneling regimes in superconducting microconstrictions: Excess current, charge imbalance, and supercurrent conversion*, Phys. Rev. B **25**, 4515 (1982).
- [3] M. Octavio, M. Tinkham, G. E. Blonder, and T. M. Klapwijk, *Subharmonic energy-gap structure in superconducting constrictions*, Phys. Rev. B **27**, 6739 (1983).
- [4] C. W. J. Beenakker, *Random-matrix theory of quantum transport*, Rev. Mod. Phys. **69**, 731 (1997).
- [5] Y. M. Blanter and M. Büttiker, *Shot noise in mesoscopic conductors*, Physics Reports **336**, 1 (2000).
- [6] X. Jehl, M. Sanquer, R. Calemczuk, and D. Mailly, *Detection of doubled shot noise in short normal-metal/superconductor junctions*, Nature **405**, 50 (2000).
- [7] T. Hoss, C. Strunk, T. Nussbaumer, R. Huber, U. Staufer, and C. Schönenberger, *Multiple andreev reflection and giant excess noise in diffusive superconductor/normal-metal/superconductor junctions*, Phys. Rev. B **62**, 4079 (2000).
- [8] F. Lefloch, C. Hoffmann, M. Sanquer, and D. Quirion, *Doubled Full Shot Noise in Quantum Coherent Superconductor-Semiconductor Junctions*, Phys. Rev. Lett. **90**, 067002 (2003).
- [9] Y. Ronen, Y. Cohen, J.-H. Kang, A. Haim, M.-T. Rieder, M. Heiblum, D. Mahalu, and H. Shtrikman, *Charge of a quasiparticle in a superconductor*, PNAS **113**, 1743 (2016).
- [10] P. Dieleman, H. Buikkens, T. Klapwijk, M. Schicke, and K. Gundlach, *Observation of Andreev Reflection Enhanced Shot Noise*, Phys. Rev. Lett. **79**, 3486 (1997).
- [11] M. J. M. de Jong and C. W. J. Beenakker, *Doubled shot noise in disordered normal-metal-superconductor junctions*, Phys. Rev. B **49**, 16070 (1994).
- [12] J. C. Cuevas, A. Martín-Rodero, and A. L. Yeyati, *Shot noise and coherent multiple charge transfer in superconducting quantum point contacts*, Phys. Rev. Lett. **82**, 4086 (1999).
- [13] R. De-Picciotto, M. Reznikov, M. Heiblum, V. Umansky, G. Bunin, and D. Mahalu, *Direct observation of a fractional charge*, Nature **389**, 162 (1997).

- [14] L. Saminadayar, D. C. Glattli, Y. Jin, and B. Etienne, *Observation of the $e/3$ fractionally charged Laughlin quasiparticle*, Phys. Rev. Lett. **79**, 2526 (1997).
- [15] H. E. van den Brom and J. M. van Ruitenbeek, *Quantum suppression of shot noise in atom-size metallic contacts*, Phys. Rev. Lett. **82**, 1526 (1999).
- [16] N. Agrait, A. L. Yeyati, and J. M. Van Ruitenbeek, *Quantum properties of atomic-sized conductors*, Physics Reports **377**, 81 (2003).
- [17] A. Burtzloff, A. Weismann, M. Brandbyge, and R. Berndt, *Shot noise as a probe of spin-polarized transport through single atoms*, Phys. Rev. Lett. **114**, 016602 (2015).
- [18] K. M. Bastiaans, T. Benschop, D. Chatzopoulos, D. Cho, Q. Dong, Y. Jin, and M. P. Allan, *Amplifier for scanning tunneling microscopy at MHz frequencies*, Rev. Sci. Instrum. **89**, 093709 (2018).
- [19] M. Ruby, B. W. Heinrich, J. I. Pascual, and K. J. Franke, *Experimental demonstration of a two-band superconducting state for lead using scanning tunneling spectroscopy*, Phys. Rev. Lett. **114**, 157001 (2015).
- [20] K. J. Franke, G. Schulze, and J. I. Pascual, *Competition of Superconducting Phenomena and Kondo Screening at the Nanoscale*, Science **332**, 940 (2011).
- [21] M. T. Randeria, B. E. Feldman, I. K. Drozdov, and A. Yazdani, *Scanning Josephson spectroscopy on the atomic scale*, Phys. Rev. B **93**, 161115(R) (2016).
- [22] E. Scheer, N. Agrait, J. C. Cuevas, A. L. Yeyati, B. Ludoph, A. Martín-Rodero, G. R. Bollinger, J. M. van Ruitenbeek, and C. Urbina, *The signature of chemical valence in the electrical conduction through a single-atom contact*, Nature **394**, 154 (1998).
- [23] R. C. Dynes, V. Narayanamurti, and J. P. Garno, *Direct Measurement of Quasiparticle-Lifetime Broadening in a Strong-Coupled Superconductor*, Phys. Rev. Lett. **41**, 1509 (1978).
- [24] G.-I. Ingold, H. Grabert, and U. Eberhardt, *Cooper-pair current through ultra-small Josephson junctions*, Phys. Rev. B **50**, 395 (1994).
- [25] V. Ambegaokar and A. Baratoff, *Tunneling between Superconductors*, Phys. Rev. Lett. **10**, 486 (1963).
- [26] B. Jäck, M. Eltschka, M. Assig, A. Hardock, M. Etzkorn, and C. R. Ast, *A nanoscale gigahertz source realized with Josephson scanning tunneling microscopy*, Appl. Phys. Lett. **106**, 013109 (2015).
- [27] C. J. Chen, *Introduction to Scanning Tunneling Microscopy Second Edition* (Oxford University Press, 2008).

- [28] H. Birk, M. J. M. de Jong, and C. Schönenberger, *Shot-noise suppression in the single-electron tunneling regime*, Phys. Rev. Lett. **75**, 1610 (1995).
- [29] H. Birk, K. Oostveen, and C. Schönenberger, *Preamplifier for electric-current noise measurements at low temperatures*, Rev. Sci. Instrum. **67**, 2977 (1996).
- [30] U. Kemiktarak, T. Ndukum, K. C. Schwab, and K. L. Ekinci, *Radio-frequency scanning tunnelling microscopy*, Nature **450**, 85 (2007).
- [31] Q. Dong, Y. X. Liang, D. Ferry, A. Cavanna, U. Gennser, L. Couraud, and Y. Jin, *Ultra-low noise high electron mobility transistors for high-impedance and low-frequency deep cryogenic readout electronics*, Appl. Phys. Lett. **105**, 6 (2014).
- [32] R. N. Jabdaraghi, D. S. Golubev, J. P. Pekola, and J. T. Peltonen, *Noise of a superconducting magnetic flux sensor based on a proximity Josephson junction*, Scientific Reports **7**, 8011 (2017).
- [33] M. Müller, N. Neel, S. Crampin, and J. Kröger, *Lateral Electron Confinement with Open Boundaries : Quantum Well States above Nanocavities at Pb (111)*, Phys. Rev. Lett. **117**, 136803 (2016).
- [34] J. Brand, P. Ribeiro, N. Néel, S. Kirchner, and J. Kröger, *Impact of atomic-scale contact geometry on andreev reflection*, Phys. Rev. Lett. **118**, 107001 (2017).
- [35] K. M. Bastiaans, D. Cho, T. Benschop, I. Battisti, Y. Huang, M. S. Golden, Q. Dong, Y. Jin, and M. P. Allan, *Charge trapping and super-Poissonian noise centres in a cuprate superconductor*, Nature Physics **14**, 1183 (2018).
- [36] F. Massee, Y. K. Huang, M. S. Golden, and M. Aprili, *Noisy defects in the high- T_c superconductor $\text{Bi}_2\text{Sr}_2\text{CaCu}_2\text{O}_{8+x}$* , Nature Comm. **10**, 544 (2019).
- [37] E. W. Carlson, K. A. Dahmen, E. Fradkin, and S. A. Kivelson, *Hysteresis and noise from electronic nematicity in high-temperature superconductors*, Phys. Rev. Lett. **96**, 097003 (2006).
- [38] P. A. Lee, *Amperean Pairing and the Pseudogap Phase of Cuprate Superconductors*, Phys. Rev. X **4**, 031017 (2014).
- [39] B. Keimer, S. A. Kivelson, M. R. Norman, S. Uchida, and J. Zaanen, *From quantum matter to high-temperature superconductivity in copper oxides*, Nature **518**, 179 (2015).
- [40] P. A. Lee, N. Nagaosa, and X.-G. Wen, *Doping a mott insulator: Physics of high-temperature superconductivity*, Rev. Mod. Phys. **78**, 17 (2006).
- [41] J. Figgins and D. K. Morr, *Differential conductance and quantum interference in kondo systems*, Phys. Rev. Lett. **104**, 187202 (2010).

- [42] S. Cocklin and D. K. Morr, *Scanning tunneling shot noise spectroscopy in kondo systems*, arXiv:1906.02553 (2019).
- [43] S. Nadj-Perge, I. K. Drozdov, J. Li, H. Chen, S. Jeon, J. Seo, A. H. MacDonald, B. A. Bernevig, and A. Yazdani, *Topological matter. Observation of Majorana fermions in ferromagnetic atomic chains on a superconductor*. *Science* **346**, 602 (2014).
- [44] T. Jonckheere, J. Rech, A. Zazunov, R. Egger, A. L. Yeyati, and T. Martin, *Giant shot noise from majorana zero modes in topological trijunctions*, *Phys. Rev. Lett.* **122**, 097003 (2019).

5

A strongly inhomogeneous superfluid in an iron-based superconductor

This chapter has been published as *Nature* **571**, 541 (2019)

Although the possibility of spatial variations in the superfluid of unconventional, strongly correlated superconductors has been suggested, it is not known whether such inhomogeneities - if they exist - are driven by disorder, strong scattering, or other factors. In this chapter we use atomic-resolution Josephson scanning tunneling microscopy to reveal a strongly inhomogeneous superfluid in the iron-based superconductor $FeTe_{0.55}Se_{0.45}$. By simultaneously measuring the topographic and electronic properties, we find that this inhomogeneity in the superfluid is not caused by structural disorder or strong inter-pocket scattering, and does not correlate with variations in the energy of the Cooper pair-breaking gap. Instead, we see a clear spatial correlation between superfluid density and the quasiparticle strength, defined as the height of the coherence peak, on a local scale. This places iron-based superconductors on equal footing with the cuprates, where a similar relation has been observed on the macroscopic scale. Our results establish the existence of strongly inhomogeneous superfluids in an unconventional superconductor, exclude chemical disorder and inter-band scattering as causes of the inhomogeneity, and shine light into the relation between quasiparticle character and superfluid density. When repeated at different temperatures, our technique could further help to elucidate what local and global mechanisms limit the critical temperature in unconventional superconductors.

5.1. INTRODUCTION

Superconductivity emerges when electrons pair up to form so-called Cooper pairs and then establish phase coherence to condense into the macroscopic quantum state that is the superfluid. Cooper pairing is governed by the binding energy of the pairs, Δ_{CP} , while the phase coherence (or stiffness) governs the superfluid density, n_{sf} [1]. For conventional superconductors like aluminum or lead, the superfluid density is spatially homogeneous because the lattice constant is much smaller than the Cooper pair size (usually hundreds of nanometers) and because the large superfluid density guarantees a high phase stiffness. In unconventional, strongly correlated superconductors the situation is very different for the following reasons: (i) the Cooper pair size, roughly given by the coherence length, is generally smaller than the pair size in conventional superconductors; (ii) the superfluid density is smaller (iii), more disorder exists due to dopant atoms or intrinsic tendencies for phase separation or charge order; and (iv) the sign of the superconducting gap changes. Despite much progress [2, 3], we lack a theoretical understanding of these strongly correlated superconductors. It has long been proposed that there can, in principle, exist spatial variations of the superfluid density [4, 5]. Very similar ideas have been discussed thoroughly in the context of superconductor-insulator transitions [6–8], or Bose-Einstein condensation of electronic liquids [9]. However, little is known about the local physics in such systems because of the technical challenges associated with visualizing the superfluid density on the atomic scale, especially when simultaneously probing the density of states to investigate the origin of the inhomogeneity. In this chapter we use atomic-resolution Josephson scanning tunneling microscopy to reveal a strongly inhomogeneous superfluid in the iron-based superconductor $FeTe_{0.55}Se_{0.45}$.

5.2. SPECTROSCOPY IN A JOSEPHSON STM

As we discussed in chapter 4, both the pair-breaking gap (the energy required to break Cooper pairs) and the superfluid density should be accessible through two distinct spectroscopic signatures in a tunneling contact between superconductors (Fig 5.1.a). The first one is visible in the single-particle channel, where Bogoliubov quasiparticles with energies larger than the pair-breaking gaps transport the charge, as shown in Fig 5.1.b. In the case of the Josephson scanning tunneling microscopy (STM) configuration, one of the superconductors is the tip with gap $\Delta_{CP,t}$ and the other is the sample with gap $\Delta_{CP,s}$; leading to a total gap of energy $2(\Delta_{CP,s} + \Delta_{CP,t})$ (Fig 5.1.c). The second spectroscopic feature is at bias energies close to the Fermi energy, where one can access the Cooper-pair channel which yields information about the superfluid density. Voltage-biased Josephson tunneling in our STM configuration differs somewhat from the case of planar junctions: the capacitive energy E_C is

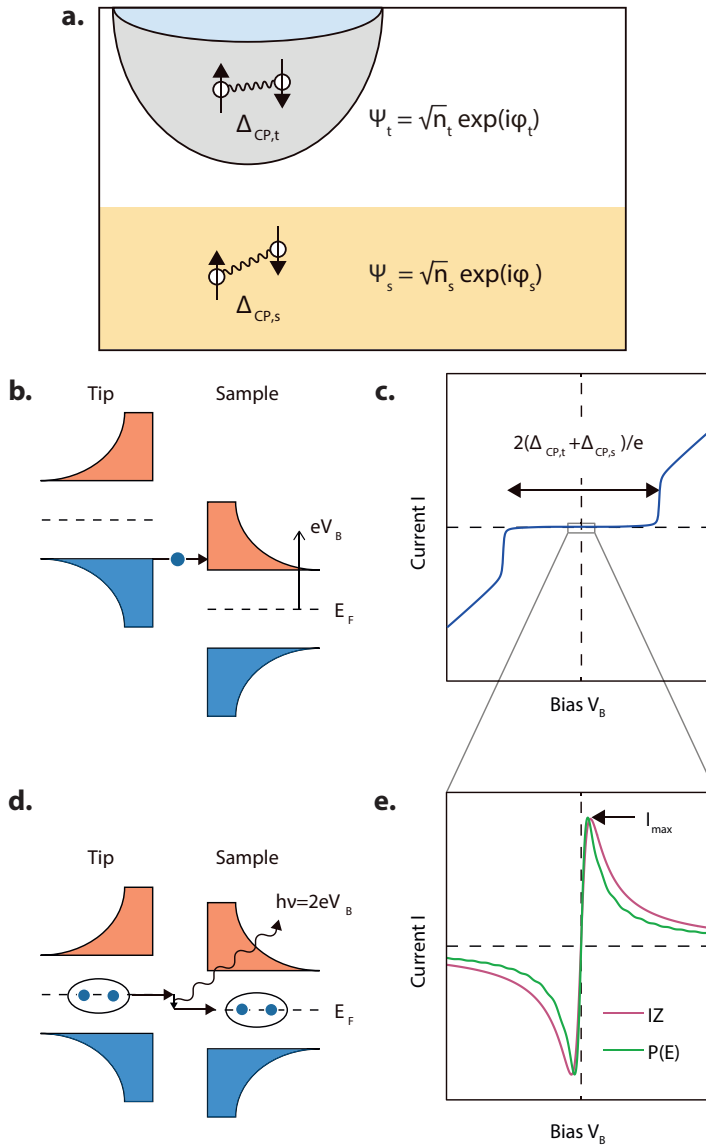


Figure 5.1: **Principles of Josephson Scanning Tunneling Microscopy.** **a.** Schematic of the Josephson junction consisting of tip (t) and sample (s). **b.** Schematic energy diagram of quasiparticle tunneling between tip and sample. Black lines indicate the density of states (horizontal axis) as a function of energy (vertical axis); filled / empty states are denoted with blue / red; dashed lines indicate the Fermi level E_F . When the voltage bias V_B is larger than $(\Delta_{CP,s} + \Delta_{CP,t})/e$, quasiparticles can tunnel. **c.** Current-Voltage I - V characteristic curve for quasiparticle tunneling. **d.** Schematic of inelastic Cooper-pair tunneling in a Josephson junction. Cooper pairs interact with the environment by emitting energy (wavy arrow) and subsequently tunnel across the junction. **e.** Simulated I - V curves for Cooper-pair tunneling. Both curves exhibit a maximum I_{max} at finite bias which is proportional to I_C^2 .

much bigger than the Josephson energy, E_J , turning the environmental impedance into a relevant quantity, and, in our case, the thermal energy is relatively high.

We calculate the current-voltage characteristics of Josephson tunneling based on two different theoretical frameworks: IZ and P(E). The former, named after its developers Ivanchenko and Zil'berman, models the environment as Ohmic and assumes that the thermal energy exceeds the Josephson energy [10]. The latter, named after the probability function central to the theory, is a quantum mechanical treatment of Cooper pair tunneling in ultra-small junctions [11]. For our specific configuration, the qualitative predictions from both theoretical descriptions are similar: a Josephson current flows at small bias, with a maximum within a few microvolts around the Fermi energy (Fig 5.1.d-e), reflected in a conductance spectrum that shows a peak at zero applied bias. The maximum Josephson current (arrow in Fig 5.1.e) is proportional to the square of the critical current I_C of the junction.

In in single band, s-wave superconductors the superfluid density is then proportional to $(I_C R_N)^2$, where R_N is the normal state resistance, and the interpretation is straightforward: it is the density of condensed Cooper pairs [12]. In multi-band or unconventional superconductors, the superfluid density defined this way represents the superposition of different contributions from different bands, with weights depending on the relative phase,

$$I_C R_N \propto \sum_i \sqrt{n_i} \cos \chi_i, \quad (5.1)$$

where n_i are the individual superfluid densities of the different bands and χ_i their relative phases (see also appendix 5.A and 5.B). When tunneling locally, one has to convert from a band basis to an orbital basis and consider the overlap of each kind of the orbitals with different bands, as well as the individual tunneling matrix elements for the different orbitals. One can still extract spatial variations in the superfluid using the definition above, if the ratios between the tunneling matrix elements are spatially constant or when the superconducting phase is not strongly related to the orbitals. But importantly, the superfluid density thus defined cannot be simply interpreted as the total density of Cooper pairs for unconventional or multi-band superconductors, including the one investigated here. Notably, the multiplication with R_N in the $(I_C R_N)^2$ product also allows to disentangle the measured superfluid density from variations in the coupling between the tip and the superfluid which might vary spatially [13, 14]. Spatially imaging a superfluid using Josephson STM techniques [15] has thus far been achieved in two instances. First, a pair density wave was discovered in a copper oxide sample [13], by exfoliating pieces of the sample onto the STM tip and imaging it with a resolution of about 1 nm. Second, the superfluid of a Pb(111) surface was resolved with atomic resolution, by using the sample material to coat the STM tip [14].

In this chapter, we investigate the unconventional iron-based superconductor $FeTe_{0.55}Se_{0.45}$. Iron-based superconductors are moderately to strongly correlated, with Hund's rule and orbital selectivity playing important roles [16]. We chose $FeTe_{0.55}Se_{0.45}$ because it encompasses the key properties of unconventional superconductivity. Furthermore, its nodeless gap structure [17, 18] and the possibility to scan at low junction resistances facilitate the Josephson experiments described below. $FeTe_{0.55}Se_{0.45}$ is considered not to be in the dirty BCS limit and has a low average superfluid density similar to cuprate high temperature superconductors [19, 20]. We cleave the single crystals at 30 K and insert the samples into our cryogenic STM system with rigorous electronic filtering (as described in chapters 2 and 4). All measurements were performed at an effective electron temperature of 2.2 K. The topograph (Fig. 5.2.a) shows atomic resolution and contrast differences that stem from the tellurium or selenium inhomogeneities; we further verify that the interstitial iron concentration is negligible. Similar to chapter 4, we use a mechanically sharpened platinum iridium wire with its apex coated with lead, which is a s-wave superconductor with a relatively large gap of ~ 1.3 meV [14].

These preparations enable us to acquire Josephson tunneling spectra and maps on $FeTe_{0.55}Se_{0.45}$. Figure 5.2 shows current and differential conductance spectra acquired at the location marked by a cross in Fig. 5.2.a. The data agrees well with expectations from the IZ and P(E) models, and reproduces small oscillation features seen previously on elemental superconductors and explained by a tip-induced antenna mode in chapter 4 and in references [14, 21]. Decreasing the junction resistance shows the increase of the critical current expected for a Josephson tunneling junction (as shown in Fig. 5.2). The rate of the increase is lower than expected for simple s-wave junctions but more consistent with theoretical predictions for a S_{\pm} pairing symmetry in the sample, where states with both positive and negative gap tunnel [22]. We further note a small kink in the Josephson current at $25\mu eV$ of yet unknown origin.

5.3. VISUALIZING THE INHOMOGENEOUS SUPERFLUID

In Figs 5.3.a and 5.3.b, we show an atomic-resolution map of the superfluid density as defined in section 5.2, extracted from $\sim 16,000$ individual spectra, and the topographic image, registered spatially to each other on the atomic scale. The most striking finding of our experiment is the strong inhomogeneity of the superfluid over length scales of the order of the coherence length, a few nanometers. We show in Fig. 5.3.c a series of individual raw spectra normalized by the normal state resistance to illustrate these changes. The inhomogeneities are not periodic; a possible underlying pair density wave is below our sensitivity. Our setup allows us to measure topographic and electronic properties in the same field of view and thus inves-

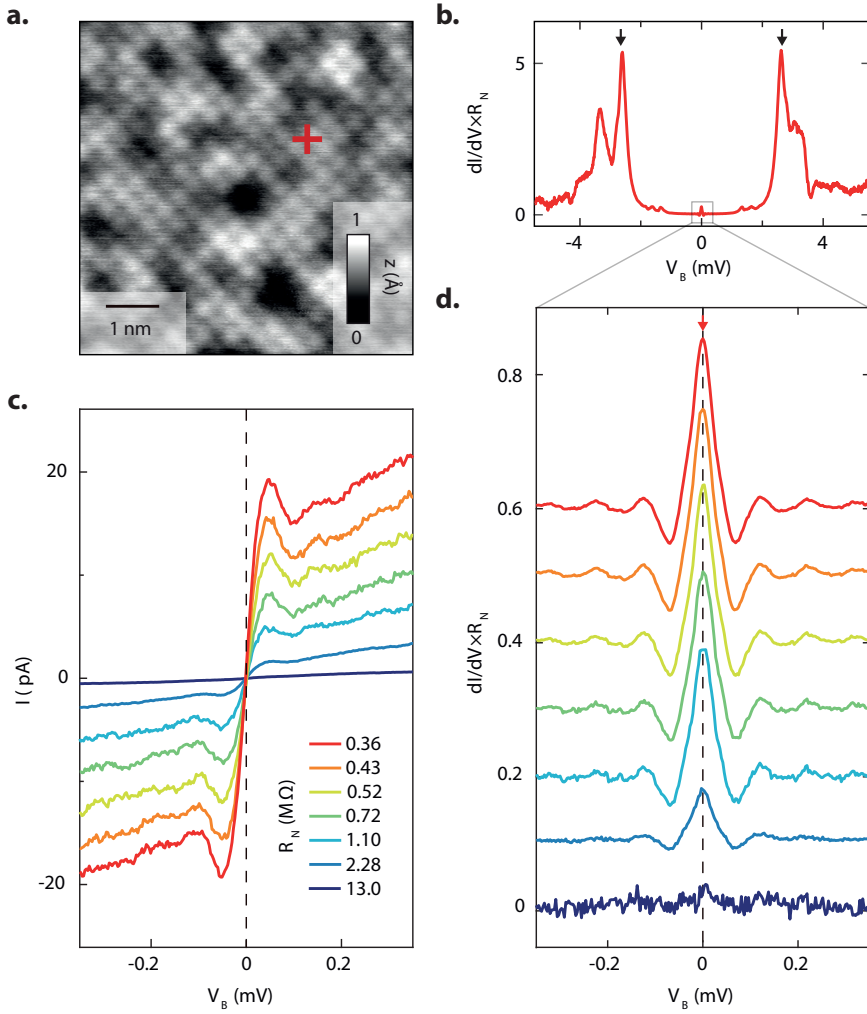


Figure 5.2: **Josephson tunneling spectra on $FeTe_{0.55}Se_{0.45}$.** **a.** Atomically resolved topographic image (setup conditions $V_{set} = -10\text{mV}$, $I_{set} = 5\text{nA}$). Brighter (darker) atoms correspond to Te (Se). **b.** Differential conductance spectrum acquired at the location of the red cross in (a), multiplied by the normal state resistance. Black arrows indicate the coherence peaks. The Josephson current can be observed at small bias. Setup conditions: $V_{set} = -10\text{ mV}$, $I_{set} = 30\text{nA}$, $V_{mod} = 20\mu V_{pp}$ **c.** Current-voltage characteristic for different normal state resistances. All spectra are acquired with $V_{set} = -10\text{ mV}$. **d.** Differential conductance spectra acquired with the same set-up conditions as in c and a lock-in modulation $V_{mod} = 20\mu V_{pp}$, multiplied by the respective normal state resistance, yielding a dimensionless quantity.

5

tigate possible causes for the inhomogeneous superfluid. The most obvious possible causes might be structural disorder and strong quasiparticle scattering. The structural disorder stems from the effective FeSe and FeTe alloying that is clearly visible in the topographic images (Fig. 5.2.a and Fig. 5.3.a). Surprisingly, the variations in the superfluid are not correlated to these structural features, with the exception of a few impurity atoms that lead to a strong suppression of the Josephson current. The strength of the quasiparticle scattering is visible in quasiparticle interference (QPI) pattern and is dominated by inter-pocket scattering in $FeTe_{0.55}Se_{0.45}$ [17]. We identify areas of strong scattering with red contours in Fig. 5.3.d, which are obtained by Fourier-filtering the QPI data in order to distinguish between strong and weak scattering regions. Again, there is no correlation between these regions and the superfluid density. We cannot exclude that the superfluid density is influenced by potential scatterers not visible in our measurement, remnant short range magnetic order, or possible phase separations at higher energies. Given the putative $s\pm$ pairing symmetry of the sample as mentioned above, one could also consider a scenario involving spatially varying tunneling matrix elements between the tip and orbitals coupled to opposite-sign gaps, leading to a spatially varying suppression of the Josephson current [22]. However, in $FeTe_{0.55}Se_{0.45}$, the gap sign is not strongly related to the orbital character [18, 23], and we do not observe the imprint that a relative change in the tunneling matrix elements of the different orbitals would leave on the local density of states and the topography. More generally, the fact that such prominent effects as the chemical disorder and the inter-pocket QPI do not influence the superfluid indicates that the inhomogeneity in the superfluid density is intrinsic.

We now return to the relation between the pair-breaking gap and the superfluid density. We extract the pair-breaking gap energy, as well as the height of the coherence peaks, which will prove to be important later, by fitting the coherence peaks of each spectrum to find the energy of the maxima. Figure 5.3.e shows the gap map for the same field of view as the Josephson map; the gap variations agree with previous reports [24]. It is clear that the pair-breaking gap is independent of the superfluid density. Instead we find a correlation to the quasiparticle character, as described in the following section.

5.4. CORRELATION BETWEEN SUPERFLUID DENSITY AND QUASIPARTICLE COHERENCE

In unconventional superconductors, there is a recurring theme that connects quasiparticle excitation line-shapes with the presence of superconductivity: Photoemission demonstrated that the incoherent quasiparticles in the normal state become coherent below the critical temperature [18, 25]. Previous STM measurements showed Bogoliubov QPI patterns at low energies which are even sharper than theory would

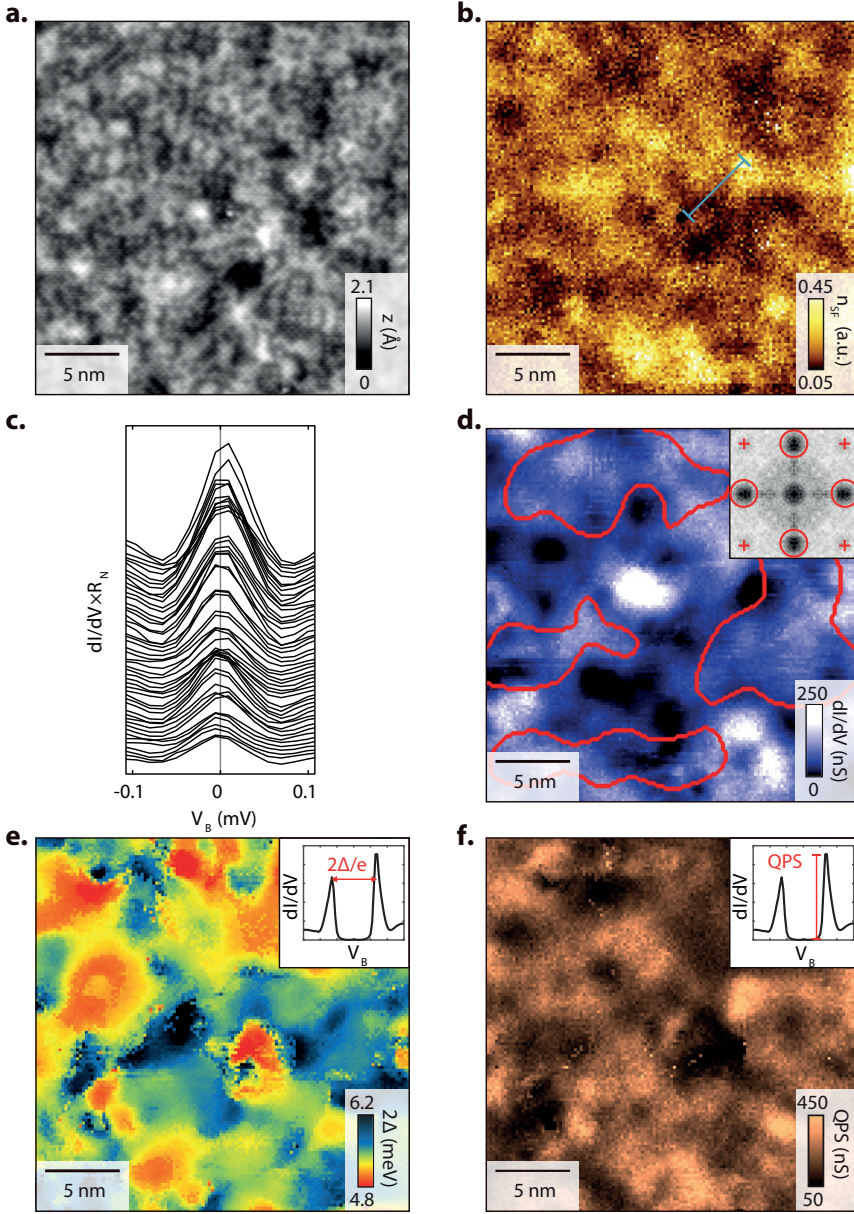


Figure 5.3: **Visualizing the superfluid in $\text{FeTe}_{0.55}\text{Se}_{0.45}$.** **a.** $25 \times 25 \text{ nm}^2$ topographic image of $\text{FeTe}_{0.55}\text{Se}_{0.45}$ ($V_{\text{set}} = -6 \text{ mV}$, $I_{\text{set}} = 0.12 \text{ nA}$). **b.** Spatially resolved map of $(I_C R_N)^2$ representing the superfluid density as discussed in section 5.2 ($V_{\text{set}} = -6 \text{ mV}$, $I_{\text{set}} = 5 \text{ nA}$, $V_{\text{mod}} = 30 \mu\text{V}_{\text{pp}}$). **c.** Series of differential conductance spectra multiplied by the normal state resistance around E_F along the blue line in (b). **d.** Conductance map at $V_B = +3.6 \text{ mV}$. Areas with strong quasiparticle interference patterns are marked by red contours, which are obtained by Fourier-filtering the QPI data using the filter shown in the inset (red circle). Inset: Fourier transform, with crosses at the Bragg peak locations. **e.** Pair-breaking gap map, $\Delta = \Delta_{\text{CPs}} + \Delta_{\text{Cpt}}$. **f.** Coherence peak-height map (QPS), extracted simultaneously with the pair-breaking gap. All maps in (b-f) were obtained in the same field of view as the topography in (a), registered to each other using the simultaneously acquired topographs. Setup conditions for (d-f): $V_{\text{set}} = -6 \text{ mV}$, $I_{\text{set}} = 0.3 \text{ nA}$, $V_{\text{mod}} = 400 \mu\text{V}_{\text{pp}}$.

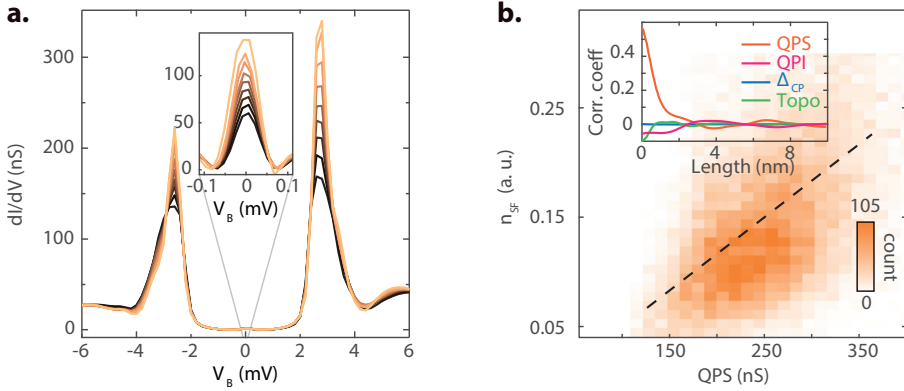


Figure 5.4: **Correlation between $(I_C R_N)^2$ and coherence peak-height.** **a.** Sorted spectra of the coherence peak-height ($V_{set} = -6\text{ mV}$, $I_{set} = 0.3\text{ nA}$) and the zero-bias Josephson peak ($V_{set} = -6\text{ mV}$, $I_{set} = 5\text{ nA}$). Spectra were sorted by binning of the superfluid density map shown in Fig. 5.3.b. The colors correspond to the quasiparticle strength in Fig. 5.3.f. **b.** Correlation between coherence peak-height and superfluid density extracted from the $(I_C R_N)^2$ product as discussed in section 5.2, yielding a correlation factor of 0.58 (dashed line). The inset shows the distance dependence of the correlation factors between the superfluid density and QPS, QPI, Δ_{CP} and topographic height.

predict, but vanish well below the gap energy [26]. Those measurements suggest a remarkable relation between the average quasiparticle excitation spectrum and superconductivity, but do not address the inhomogeneous character of unconventional superconductors. Although recently a relation between superfluid density and quasiparticle character has been conjectured to hold also locally for single-layer cuprates [27], direct experimental evidence is so far missing. Our measurement allows us to extract the quasiparticle strength (QPS), which we define phenomenologically as the height of the coherence peak (Fig. 5.3.f), and relate it directly to the superfluid density at the same location. Indeed, we find a striking correlation between the superfluid density and the QPS over the whole field of view, with a linear correlation coefficient of 0.58 (Fig. 5.4). Although this phenomenology cannot be explained by an existing theory, it points towards a local mechanism behind the relation found by photoemission experiments - a condition fulfilled by pinned thermal phase fluctuations and glassy superconductivity [1, 28].

The length scales of the superfluid inhomogeneity and of its correlation to the QPS (Fig. 5.4.b, inset) are of the same order as the average electron-electron distance. Therefore, our measurement indicates that the Cooper pairs in $\text{FeTe}_{0.55}\text{Se}_{0.45}$ are very local: they are small in size and have little overlap in comparison to the ones in conventional superconductors. We can further compare this situation to the crossover from momentum-condensed pairs described by BCS and completely local pairs described by Bose-Einstein condensation (BEC) which has been demonstrated

with ultracold atomic gases for s-wave superfluids [29, 30]. There also exist indications for pairing in the BEC or crossover regime close to superconductor-insulator transitions and in the cuprates; in $FeTe_{0.55}Se_{0.45}$ the phenomenology is not conclusive [18, 31]. Our data points towards local pairs in $FeTe_{0.55}Se_{0.45}$, but we note that in a multi-band, putative sign-changing superconductor, we expect the situation to be more complicated than the realization seen in ultracold atomic gases, and both better theory and more experiments are needed.

5.5. CONCLUSIONS AND OUTLOOK

In this chapter we have detected and directly imaged a strongly inhomogeneous superfluid and simultaneously measured the electronic and topographic properties in the same field of view, with atomic resolution. We found that the superfluid inhomogeneity is not caused by the structural disorder resulting from the Se/Te alloying, by the inter-pocket scattering, or by the variations of the pair-breaking gap energy (Fig. 5.4b, inset). Instead, the superfluid density shows strong positive correlation with the sharpness of the quasiparticle peak: Superconductivity appears to be needed for coherent quasiparticles, locally on the length scale of cooper pairing. It will be instructive to use the techniques described here to investigate the superfluid density in other materials, including superconductor-insulator transitions, disordered conventional superconductors, or twisted bilayer graphene [32, 33]. Lastly, we anticipate that future temperature-dependent superfluid density and gap measurements will elucidate what local and global mechanisms limit T_C in unconventional superconductors.

APPENDICES

5.A. ACCESSING THE SUPERFLUID DENSITY WITH JOSEPHSON STM

In Josephson Scanning Tunneling Microscopy (JSTM) [34], the Josephson junction [35] is formed between a STM tip and sample (both superconducting) which are separated by a vacuum barrier. The tunneling current of Cooper pairs contains information about the superfluid in both sample and tip. Starting from the wavefunctions of the superconductors on the tip (t) and the sample (s),

$$\Psi_{s,t} = \sqrt{n_{SF,s(t)}} \exp\{-i\phi_{s(t)}\}, \quad (5.2)$$

where $n_{SF,s(t)}$ is the superfluid density and $\phi_{s(t)}$ the phase of the condensate in the sample or tip, it can be shown that the supercurrent follows the Josephson relation

$$I = I_C \sin \phi_s - \phi_t, \quad (5.3)$$

with

$$I_C = \kappa \sqrt{n_{SF,s}} \sqrt{n_{SF,t}}, \quad (5.4)$$

(κ is a coupling constant) being the maximum (critical) supercurrent that the junction can sustain. Assuming the superfluid density in the tip to be constant, one can treat the critical supercurrent as a measure to probe the superfluid density in the sample. We note that while the relation between critical current and superfluid density is straightforward in single band s-wave superconductors [36, 37], it can become more complicated in multiband systems, where the critical current is related to an effective superposition of superfluid densities [38–43]. Because the ratio between tunneling elements into different orbitals is spatially constant, and because the gap sign is only weakly coupled to the different orbitals, the changes in I_C that we measure reflect changes of the superfluid density in the sample.

5.B. DETERMINING THE CRITICAL CURRENT FROM JOSEPHSON TUNNELING SPECTRA

To extract the critical supercurrent from our spectra, we fit the conductance spectra with the use of the IZ model [10]. Taking the derivative of the IZ formula with respect to the voltage we get:

$$dI/dV = \frac{I_C^2 Z_{env}}{2} \frac{V_C^2 - V^2}{(V^2 + V_C^2)^2}, \quad (5.5)$$

We fit our spectrum based on the above formula with free fitting parameters being the pre-factor $I_C^2 Z_{env}/2$ and V_C . A typical IZ fit of the conductance spectrum is shown in Fig. 5.5.

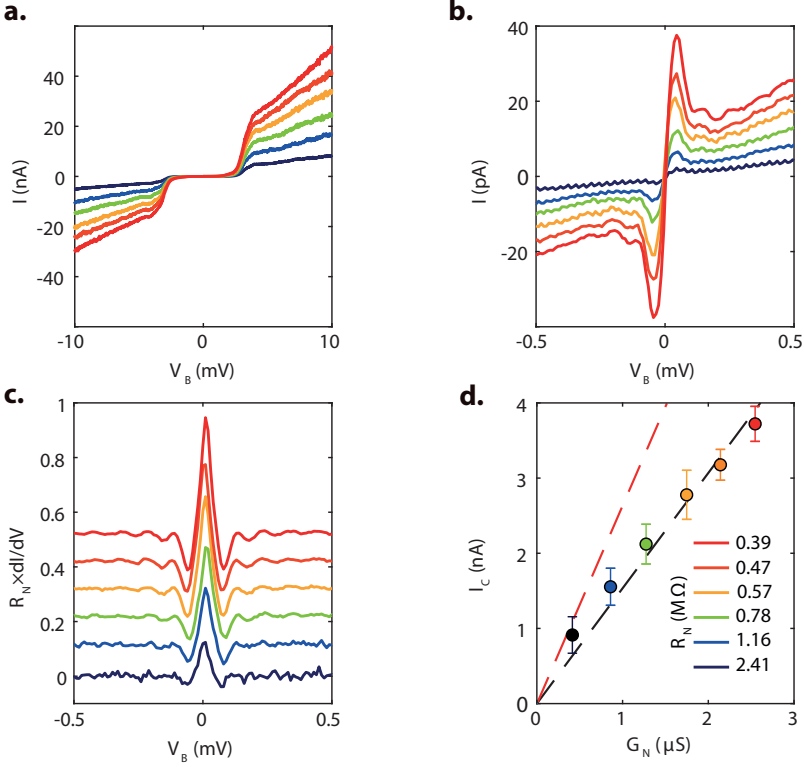


Figure 5.5: **Josephson tunneling spectroscopy in the Pb / FeTe_{0.55}Se_{0.45} junction.** **a-b.** R_N -dependent I-V curves. **c.** R_N -dependent dI/dV curves multiplied by R_N corresponding to I-V curves in (a-b). Curves are offset for clarity. When decreasing R_N , Cooper-pair tunneling induced zero bias peak and small modulations with period of 0.1 meV become more pronounced. **d.** The linear relation (black dashed line) between the critical Josephson current and the normal state conductance. The red dashed line corresponds to AB-formula for a asymmetry Josephson junction where two superconductor electrodes have same s-wave symmetry with different sizes of the pair-breaking gap ($\Delta_{CP,t} = 1.30$ meV and $\Delta_{CP,s} = 1.68$ meV).

According to the IZ model the maximum (I_{max}) in the I-V characteristics is related to the critical supercurrent in the following way,

$$I_C = \sqrt{\frac{8I_{max}ek_BT}{\hbar}}. \quad (5.6)$$

Hence, we can use the maximum from our I-V curves and use the above formula for quantifying I_C (we use $T = 2.2$ K which is equal to our measurement temperature). In Fig. 5.5, we plot I_C as function of normal junction conductance $G_N = (R_N)^{-1}$. A linear trend is observed which is consistent with previous theoretical works. A linear fit to our data gives a slope of 1.534 meV which is used to estimate Δ_s from the formula of an asymmetric junction [44],

$$I_C R_N = \frac{2}{e} \frac{\Delta_{CP,t} \Delta_{CP,s}}{\Delta_{CP,t} + \Delta_{CP,s}} K \left(\left| \frac{\Delta_{CP,t} - \Delta_{CP,s}}{\Delta_{CP,t} + \Delta_{CP,s}} \right| \right), \quad (5.7)$$

where $K(x)$ is the elliptic integral function of first kind. Assuming $\Delta_{CP,t} = 1.3$ meV we find $\Delta_{CP,s} = 0.67$ meV. This is to be compared with the gap that we read from our conductance spectra. We find that the coherence peak is located at 3.08 meV. Subtracting $\Delta_{CP,t}$ gives an estimation of $\Delta_{CP,s} = 1.68$ meV. We believe that the reason for this deviation can be attributed to the unconventional superconducting nature of $FeTe_{0.55}Se_{0.45}$. Sign-changing gaps have been shown to influence the Josephson tunneling [22, 38–43]. It has been predicted theoretically that for Cooper pair tunneling between a conventional s-wave superconductor and an unconventional s_{\pm} multiband superconductor (here $FeTe_{0.55}Se_{0.45}$) I_C still grows linearly with G_N . However, for that case the slope is expected to be lower. Such reduction of Josephson current was also observed in a multiband superconductor without sign changing using a s-wave superconducting tip [43]. We expect that better calculations of the orbital-decomposed gap structure and their individual tunneling processes allow for quantitative comparisons with our data.

5.C. VISUALIZING THE SUPERFLUID DENSITY FOR SAMPLES WITH INHOMOGENEOUS NORMAL STATE JUNCTION RESISTANCE

To visualize the spatial variations of the superfluid density, we record differential conductance spectroscopic maps on a grid of points (r_x, r_y) and fit each spectrum using the IZ model described in the previous section. This allows us to construct atomic-scale $I_C(\mathbf{r})$ maps, i.e. the magnitude of the critical supercurrent as a function of location. Figure 5.6.a-b show an example of these maps on the same $25 \times 25 nm^2$ field of view, obtained using opposite setup bias Fig. 5.6.a -10 mV and Fig. 5.6.b +10 mV). These maps reveal spatial variations of the critical supercurrent on a small length scale of a few nanometers. However, we notice that these two maps are not well consistent. This is because I_C (the measured critical current of the junction) is

influenced by the single-particle tunneling transmission rate represented by $(R_N)^{-1}$ at each point (r_x, r_y) . To allow for direct measurement of intrinsic variations of the superfluid density we take the product of the measured $I_C(\mathbf{r})$ with $R_N(\mathbf{r})$ (see Ref. [13]). Figures 5.6.c-d show the measured $R_N(\mathbf{r})$ images in the same field of view as the $I_C(\mathbf{r})$ maps for both bias polarities. The $R_N(\mathbf{r})$ are obtained by summing over all spatial resolved differential conductance layers $g(\mathbf{r})$ and divide by the size of the energy window. The product of measured $(I_C(\mathbf{r})R_N(\mathbf{r}))^2$ enables us to deduce the spatial variations of the superfluid density.

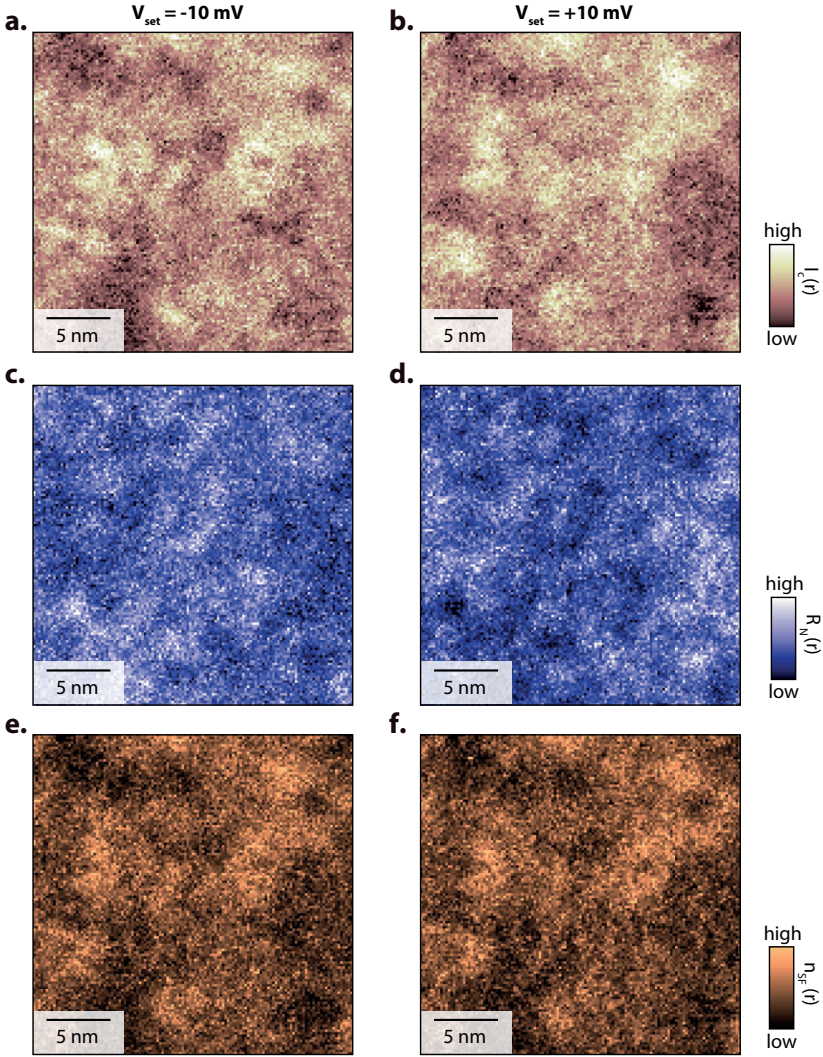


Figure 5.6: **Superfluid density maps with inhomogeneous normal state resistance.** **a-b.** The critical Josephson current I_C map. **c-d.** The spatial variations of the normal state resistance R_N . **e-f.** The $(I_C R_N)^2$ map associated with the superfluid density. The left (right) column were acquired with set-up bias of -10 mV (+10 mV) and set-up current of 10 nA. To map the intrinsic superfluid density, it is necessary to normalize the measured I_C by multiplying R_N . Topographs are simultaneously measured and used to align different maps.

BIBLIOGRAPHY

- [1] V. J. Emery and S. A. Kivelson, *Importance of phase fluctuations in superconductors with small superfluid density*, Nature **374**, 434 (1995).
- [2] F. Wang and D.-H. Lee, *The electron-pairing mechanism of iron-based superconductors*, Science **332**, 200 (2011).
- [3] B. Keimer, S. A. Kivelson, M. R. Norman, S. Uchida, and J. Zaanen, *From quantum matter to high-temperature superconductivity in copper oxides*. Nature **518**, 179 (2015).
- [4] P. Fulde and R. A. Ferrell, *Superconductivity in a strong spin-exchange field*, Phys. Rev. **135**, A550 (1964).
- [5] A. I. Larkin and Y. N. Ovchinnikov, *Nonuniform state of superconductors*, Zh. Eksperim. i Teor. Fiz. **47** (1964).
- [6] A. Ghosal, M. Randeria, and N. Trivedi, *Spatial inhomogeneities in disordered d-wave superconductors*, Phys. Rev. B **63**, 020505 (2000).
- [7] M. V. Feigel'man and L. B. Ioffe, *Superfluid density of a pseudogapped superconductor near the superconductor-insulator transition*, Phys. Rev. B **92**, 100509 (2015).
- [8] K. Bouadim, Y. L. Loh, M. Randeria, and N. Trivedi, *Single-and two-particle energy gaps across the disorder-driven superconductor-insulator transition*, Nature Physics **7**, 884 (2011).
- [9] I. Božović, J. Wu, X. He, and A. T. Bollinger, *What is really extraordinary in cuprate superconductors?* Physica C **558**, 30 (2019).
- [10] Y. M. Ivanchenko and L. A. Zil'Berman, *The Josephson Effect in Small Tunnel Contacts*, Sov. Phys. JETP **28**, 1272 (1969).
- [11] G.-L. Ingold, H. Grabert, and U. Eberhardt, *Cooper-pair current through ultra-small josephson junctions*, Phys. Rev. B **50**, 395 (1994).
- [12] O. Naaman, W. Teizer, and R. C. Dynes, *Fluctuation dominated josephson tunneling with a scanning tunneling microscope*, Phys. Rev. Lett. **87**, 097004 (2001).
- [13] M. H. Hamidian, S. D. Edkins, S. H. Joo, A. Kostin, H. Eisaki, S. Uchida, M. J. Lawler, E.-A. Kim, A. P. Mackenzie, K. Fujita, J. Lee, and J. C. Davis, *Detection of a cooper-pair density wave in $\text{Bi}_2\text{Sr}_2\text{CaCu}_2\text{O}_{8+x}$* , Nature **532**, 343 (2016).
- [14] M. T. Randeria, B. E. Feldman, I. K. Drozdov, and A. Yazdani, *Scanning josephson spectroscopy on the atomic scale*, Phys. Rev. B **93**, 161115 (2016).

- [15] M. Graham and D. K. Morr, *Imaging the spatial form of a superconducting order parameter via josephson scanning tunneling spectroscopy*, Phys. Rev. B **96**, 184501 (2017).
- [16] Z. P. Yin, K. Haule, and G. Kotliar, *Kinetic frustration and the nature of the magnetic and paramagnetic states in iron pnictides and iron chalcogenides*, Nature Materials **10**, 932 (2011).
- [17] T. Hanaguri, S. Niitaka, K. Kuroki, and H. Takagi, *Unconventional s-wave superconductivity in fe (se, te)*, Science **328**, 474 (2010).
- [18] H. Miao, W. H. Brito, Z. P. Yin, R. D. Zhong, G. D. Gu, P. D. Johnson, M. P. M. Dean, S. Choi, G. Kotliar, W. Ku, X. C. Wang, C. Q. Jin, S.-F. Wu, T. Qian, and H. Ding, *Universal $2\Delta_{max}/k_B T_c$ scaling decoupled from the electronic coherence in iron-based superconductors*, Phys. Rev. B **98**, 020502 (2018).
- [19] C. C. Homes, Y. M. Dai, J. S. Wen, Z. J. Xu, and G. D. Gu, *fete_{0.55}se_{0.45}: A multi-band superconductor in the clean and dirty limit*, Phys. Rev. B **91**, 144503 (2015).
- [20] M. Bendele, S. Weyeneth, R. Puzniak, A. Maisuradze, E. Pomjakushina, K. Conder, V. Pomjakushin, H. Luetkens, S. Katrych, A. Wisniewski, R. Khasanov, and H. Keller, *Anisotropic superconducting properties of single-crystalline fese_{0.5}te_{0.5}*, Phys. Rev. B **81**, 224520 (2010).
- [21] B. Jäck, M. Eltschka, M. Assig, A. Hardock, M. Etzkorn, and C. R. Ast, *A nanoscale gigahertz source realized with Josephson scanning tunneling microscopy*, App. Phys. Lett. **106**, 013109 (2015).
- [22] Y. Ota, N. Nakai, H. Nakamura, M. Machida, D. Inotani, Y. Ohashi, T. Koyama, and H. Matsumoto, *Ambegaokar-baratoff relations for josephson critical current in heterojunctions with multigap superconductors*, Phys. Rev. B **81**, 214511 (2010).
- [23] Z. K. Liu, M. Yi, Y. Zhang, J. Hu, R. Yu, J.-X. Zhu, R.-H. He, Y. L. Chen, M. Hashimoto, R. G. Moore, S.-K. Mo, Z. Hussain, Q. Si, Z. Q. Mao, D. H. Lu, and Z.-X. Shen, *Experimental observation of incoherent-coherent crossover and orbital-dependent band renormalization in iron chalcogenide superconductors*, Phys. Rev. B **92**, 235138 (2015).
- [24] U. R. Singh, S. C. White, S. Schmaus, V. Tsurkan, A. Loidl, J. Deisenhofer, and P. Wahl, *Spatial inhomogeneity of the superconducting gap and order parameter in fese_{0.4}te_{0.6}*, Phys. Rev. B **88**, 155124 (2013).
- [25] D. L. Feng, D. H. Lu, K. M. Shen, C. Kim, H. Eisaki, A. Damascelli, R. Yoshizaki, J.-i. Shimoyama, K. Kishio, G. D. Gu, S. Oh, A. Andrus, J. O'Donnel, J. N. Eckstein, and Z.-X. Shen, *Signature of superfluid density in the single-particle excitation spectrum of bi2sr2cacu2o8+ δ* , Science **289**, 277 (2000).

- [26] Y. Kohsaka, C. Taylor, P. Wahl, A. Schmidt, J. Lee, K. Fujita, J. W. Alldredge, K. McElroy, J. Lee, H. Eisaki, S. Uchida, D.-H. Lee, and J. C. Davis, *How cooper pairs vanish approaching the mott insulator in $\text{Bi}_2\text{Sr}_2\text{CaCu}_2\text{O}_{8+\delta}$* , Nature **454**, 1072 (2008).
- [27] W. Ruan, X. Li, C. Hu, Z. Hao, H. Li, P. Cai, X. Zhou, D.-H. Lee, and Y. Wang, *Visualization of the periodic modulation of cooper pairing in a cuprate superconductor*, Nature Physics **14**, 1178 (2018).
- [28] Y. Dubi, Y. Meir, and Y. Avishai, *Nature of the superconductor–insulator transition in disordered superconductors*, Nature **449**, 876 (2007).
- [29] I. Bloch, J. Dalibard, and W. Zwerger, *Many-body physics with ultracold gases*, Rev. Mod. Phys. **80**, 885 (2008).
- [30] M. Randeria and E. Taylor, *Crossover from bardeen-cooper-schrieffer to bose-einstein condensation and the unitary fermi gas*, Annu. Rev. Condens. Matter Phys. **5**, 209 (2014).
- [31] B. Sacépé, T. Dubouchet, C. Chapelier, M. Sanquer, M. Ovadia, D. Shahar, M. Feigel'man, and L. Ioffe, *Localization of preformed cooper pairs in disordered superconductors*, Nature Physics **7**, 239 (2011).
- [32] Y. Cao, V. Fatemi, S. Fang, K. Watanabe, T. Taniguchi, E. Kaxiras, and P. Jarillo-Herrero, *Unconventional superconductivity in magic-angle graphene superlattices*, Nature **556**, 43 (2018).
- [33] N. Reyren, S. Thiel, A. D. Caviglia, L. F. Kourkoutis, G. Hammerl, C. Richter, C. W. Schneider, T. Kopp, A.-S. Rüetschi, D. Jaccard, M. Gabay, D. A. Muller, J.-M. Triscone, and J. Mannhart, *Superconducting Interfaces Between Insulating Oxides*, Science **317**, 1196 (2007).
- [34] J. Šmakov, I. Martin, and A. V. Balatsky, *Josephson scanning tunneling microscopy*, Phys. Rev. B **64**, 212506 (2001).
- [35] B. D. Josephson, *Possible new effects in superconductive tunnelling*, Physics Letters **1**, 251 (1963).
- [36] M. Tinkham, *Introduction to superconductivity* (McGraw-Hill, Inc. New York, 1996).
- [37] V. Ambegaokar and A. Baratoff, *Tunneling between Superconductors*, Phys. Rev. Lett. **10**, 486 (1963).
- [38] C. C. Tsuei and J. R. Kirtley, *Pairing symmetry in cuprate superconductors*, Rev. Mod. Phys. **72**, 969 (2000).

- [39] T. K. Ng and N. Nagaosa, *Broken time-reversal symmetry in josephson junction involving two-band superconductors*, EPL (Europhysics Letters) **87**, 17003 (2009).
- [40] Y. Ota, M. Machida, T. Koyama, and H. Matsumoto, *Theory of heterotic superconductor-insulator-superconductor josephson junctions between single- and multiple-gap superconductors*, Phys. Rev. Lett. **102**, 237003 (2009).
- [41] P. Seidel, *Josephson effects in iron based superconductors*, Superconductor Science and Technology **24**, 043001 (2011).
- [42] S.-Z. Lin, *Josephson effect between a two-band superconductor with $s++$ or $s\pm$ pairing symmetry and a conventional s -wave superconductor*, Phys. Rev. B **86**, 014510 (2012).
- [43] O. Naaman, R. C. Dynes, and E. Bucher, *Josephson effect in $PbI/nbse_2$ scanning tunneling microscope junctions*, International Journal of Modern Physics B **17**, 3569 (2003).
- [44] P. W. Anderson, *Lectures on the Many-body Problem* (Academic Press, New York, 1964).

6

Universality of pseudogap and emergent order in lightly doped Mott insulators

This chapter has been published as *Nature Physics* **13**, 21 (2017)

It is widely believed that high-temperature superconductivity in the cuprates emerges from doped Mott insulators [1]. When extra carriers are inserted into the parent state, the electrons become mobile but the strong correlations from the Mott state are thought to survive; inhomogeneous electronic order, a mysterious pseudogap and, eventually, superconductivity appear. How the insertion of dopant atoms drives this evolution is not known, nor whether these phenomena are mere distractions specific to hole-doped cuprates or represent genuine physics of doped Mott insulators. Here, we visualize the evolution of the electronic states of $(\text{Sr}_{1-x}\text{La}_x)_2\text{IrO}_4$, which is an effective spin- $1/2$ Mott insulator like the cuprates, but is chemically radically different [2, 3]. Using spectroscopic-imaging STM, we find that for doping concentration of $x \approx 5\%$, an inhomogeneous, phase separated state emerges, with the nucleation of pseudogap puddles around clusters of dopant atoms. Within these puddles, we observe the same electronic order that is so iconic for the underdoped cuprates [1, 4–9]. Further, we illuminate the genesis of this state using unique possibilities on these samples. At low doping, we find evidence for deeply trapped carriers, leading to fully gapped spectra, which abruptly collapse at a threshold of around 4%. Our results clarify the melting of the Mott state, and establish phase separation and electronic order as generic features of doped Mott insulators.

6.1. INTRODUCTION

A core mystery of condensed matter physics is how the rigid arrangement of electrons in Mott insulators loosens when inserting electrons or holes, and how this leads to exotic states inside the Mott gap (Fig. 6.1). In the cuprate high-temperature superconductors, this process might be the cause of their poorly understood, remarkably complex behavior. Most prominent is the formation of a pseudogap and a variety of inhomogeneous electronic orders [4–9], sometimes described as intertwined [10]. This phenomenology has often been assumed (but not verified) to be generic of melting spin- $1/2$ Mott physics and not just cuprate-specific. In this chapter we show that an inhomogeneous electronic phase separation as well as a local glassy, stripy charge order exist in a chemically completely different two-dimensional Mott insulator, revealing an universality of these emergent phenomena.

To this end, we create $(\text{Sr}_{1-x}\text{La}_x)_2\text{IrO}_4$ samples with a range of different Lanthanum doping concentrations x , $0 < x < 6\%$. This material can be seen as a quasi two-dimensional, electron-doped Mott insulator similar to the cuprates despite a very different chemical make-up. The $x = 0$ parent material consists of alternating IrO_2 and SrO planes, such that oxygen octahedra form around each iridium atom. The five valence electrons in the outer Ir $5d$ shell are split by crystal field and strong spin-orbit coupling to form a filled $J_{\text{eff},3/2}$ and a half filled $J_{\text{eff},1/2}$ band. The moderate on-site repulsion U is then sufficient to open a Mott gap in the $J_{\text{eff},1/2}$ band, making Sr_2IrO_4 an effective spin- $1/2$ Mott insulator (Fig. 6.1.a-b) [3]. In contrast to hole doping in the cuprates, which is often interstitial oxygen doping, La^{3+} substitutions on the Sr site provide electron-doping for the iridates (Fig. 6.1.c-d). The resulting electronic structure is sometimes predicted to become high-temperature superconducting upon sufficient doping [11, 12].

Figures 6.1.e-f depict typical topographs on atomically flat, SrO terminated surfaces for different doping concentrations; the SrO lattice is visible with lattice constant $a_0 = 3.9\text{\AA}$ and the white squares identify the positions of La dopant atoms in the same layer [13]. The ability to identify the dopant positions easily with atomic precision on the topographs (e.g. in contrast to the cuprates [14, 15]) is key to this investigation, as it allows to precisely localize dopant atoms, even when samples show micrometer variations of the dopant concentration. For this study, we investigate surfaces with local doping concentrations of 2.1%, 2.2% (Fig. 6.1.e), 2.3%, 3.7%, 4.8%, 5.0% (Fig. 6.1.f), 5.2%, 5.5% (Fig. 6.3 and Fig. 6.4) in order to obtain a full overview of the doping evolution (Fig. 6.5).

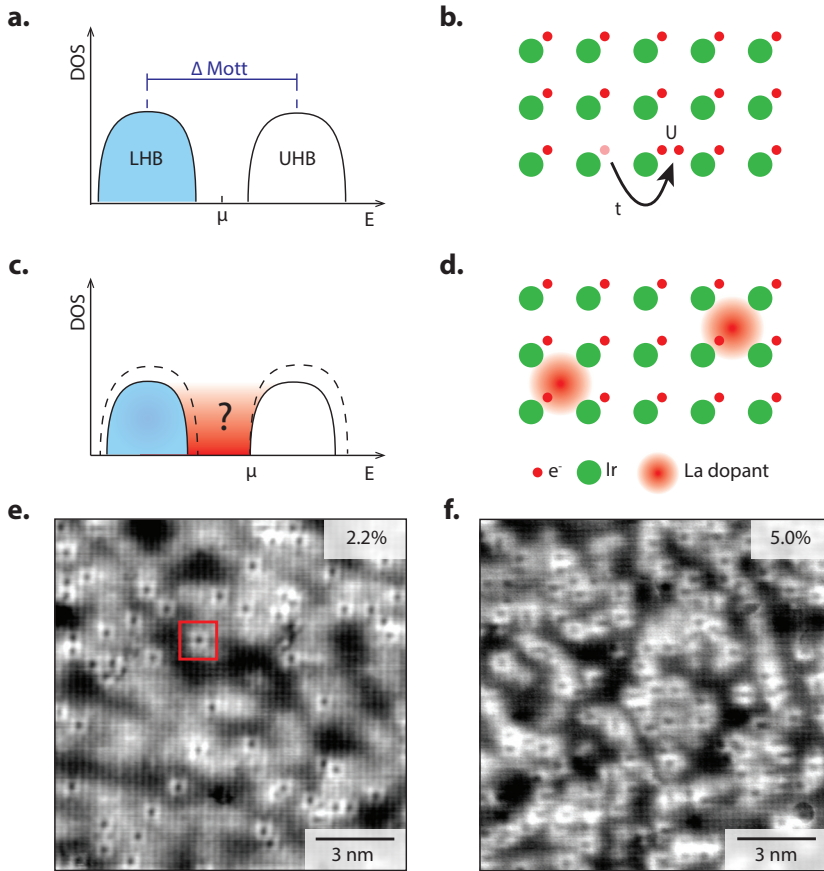


Figure 6.1: **The lightly doped effective Mott insulator** $(\text{Sr}_{1-x}\text{La}_x)_2\text{IrO}_4$. **a.** In Mott insulators, the electronic states split into a lower and upper Hubbard band separated by the Mott gap. **b.** The gap is caused by the on site interaction U that prevents electrons from hopping from site to site with energy gain t . **c.** **d.** When doping with charge carriers, new states move into the Mott gap in unknown ways. **e.** Atomically resolved topograph with a doping concentration 2.2%. The La^{3+} dopant atoms are readily identified as dark spots surrounded by brighter atoms (red square). **d.** Atomically resolved topograph with a doping concentration of 5.0%.

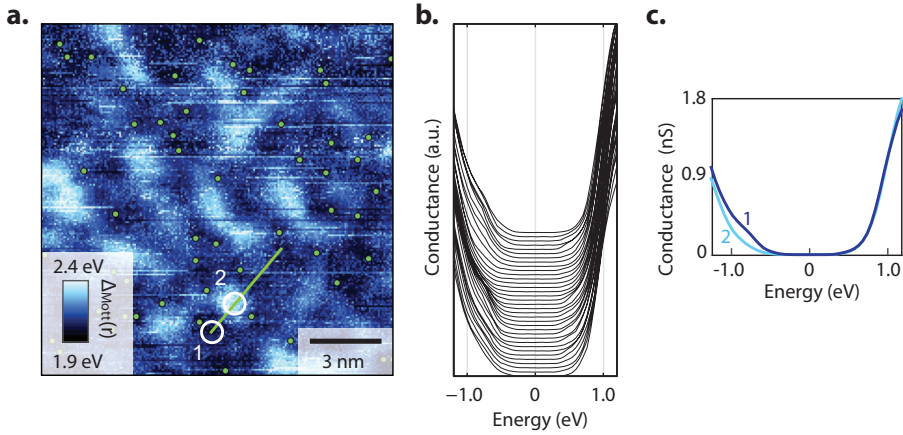


Figure 6.2: **The electronic structure of $(\text{Sr}_{1-x}\text{La}_x)_2\text{IrO}_4$ at low doping.** **a.** Mott gap map Δ_{Mott} of a sample with a doping concentration of $x = 2.2\%$. Position of dopant atoms are indicated by green circles. **b.** Local density of states spectra along the green line in (a) each with an offset on the vertical axis. **c.** Local density of states spectra averaged inside the white circles (1-2). An additional density of states at around -0.8 V is visible in the low gap regions, and might be related to the impending collapse of the impurity Mott state discussed later.

6.2. LOW DOPING: FROZEN MOTT STATE

We start our discussion with the very lightly doped samples that are deep in the Mott phase. A typical topograph of a sample with 2.2% dopant concentration is shown in Fig. 6.1.e. In all our measurements, this doping level yields a clear Mott gap, as shown in Fig. 6.2.a. The shape of the gap is reminiscent of STM spectra of cuprate parent materials [5–7, 16]. Battisti *et al.* describes how the poor screening in lightly doped Mott insulators leads to an additional potential that decays inside the sample, commonly called tip-induced-band-bending [17–19], yielding an apparent energy gap larger than the true Mott gap, $\Delta_{\text{appMott}} \gg \Delta_{\text{Mott}}$, which makes the gap roughly consistent with optical measurements [20].

To investigate how the Mott state reacts when dopant atoms are inserted, we acquire atomic-scale Mott maps, i.e. the magnitude of the Mott gap as a function of location, $\Delta_{\text{Mott}}(\mathbf{r})$, while measuring the dopant positions on the atomic scale. Each Mott map is extracted from a set of differential conductance spectra measured on a grid (rx, ry) . Figure 6.2a shows the result on a 2.2% sample; the dopant atoms are marked by green dots. La dopants do not significantly change the Mott gap size in their close vicinity; instead, they induce or pin long wavelength arrangement of varying Mott gap. We interpret these nanoscale arrangements as the first of a series of orders that appear upon doping. The most surprising observation, however, is the total lack of in-gap states, despite the presence of dopants – a mystery to which we shall return towards

the end of this chapter.

6.3. HIGHER DOPING: PSEUDOGAP AND LOCAL ORDER

6.3.1. PHASE SEPARATION: MOTT AND PSEUDOGAP

The pure Mott state described thus far is not sustained at doping levels above $\sim 5\%$. At that point, we discover an abrupt transition to a strikingly inhomogeneous electronic structure: a phase separated Mott/pseudogap landscape [21–23]. Some regions still exhibit a pure Mott gap; in contrast to the very low doping samples, now the Fermi level is pinned closer to the bottom of the upper Hubbard band, (blue curve in Fig. 6.3.a), as expected for a Mott insulator doped with free carriers (similar to electron doped bi-layer iridate [24] and opposite to hole doped cuprates [6]). Additionally, there are regions where we measure electronic states inside the Mott gap (red curve in Fig. 6.3a). Here, the spectra are remarkably similar to the pseudogap in the cuprates [4–6], with a gap value of around 70-300 meV, in rough agreement with recent photoemission measurements that extracted the leading edge gap [25, 26], and with some spectra showing clear ‘coherence peaks’ (Fig 6.3.d). We will refer to these regions as ‘pseudogap puddles’. They are not randomly distributed, but form around regions with clusters of dopant atoms. Importantly, we do not observe pseudogap puddles in low doped samples, even if a few dopants happen to be close together by chance; a certain threshold in the doping level is needed for the transition to occur.

In order to further analyze this phase separated landscape, it is necessary to establish the spatial distribution of the Mott/pseudogap character. To do so, we introduce a “Mott parameter” $M(\mathbf{r})$ by integrating the density-of states inside the putative Mott gap and normalize it by the integrated density-of-states outside the gap (Fig. 6.3.c, inset),

$$M(\mathbf{r}) = \int_{-350\text{meV}}^{+50\text{meV}} \text{LDOS}(\mathbf{E})d\mathbf{E} / \int_{+200\text{meV}}^{+500\text{meV}} \text{LDOS}(\mathbf{E})d\mathbf{E}. \quad (6.1)$$

This parameter is large when there are states inside the gap, and small when the Mott gap is dominating. Plotting $M(\mathbf{r})$ as a function of the spatial coordinates reveals the nanoscale character of the phase separation, with pseudogap puddles within regions of pure Mott gap. The phase separation is well defined and sharp, in the sense that the transition from pure Mott area to a pseudogap puddle occurs within less than a nanometer (Fig. 6.3.d). This allows us to define a threshold for Mott and pseudogap regions (black contour in Fig. 6.3.c).

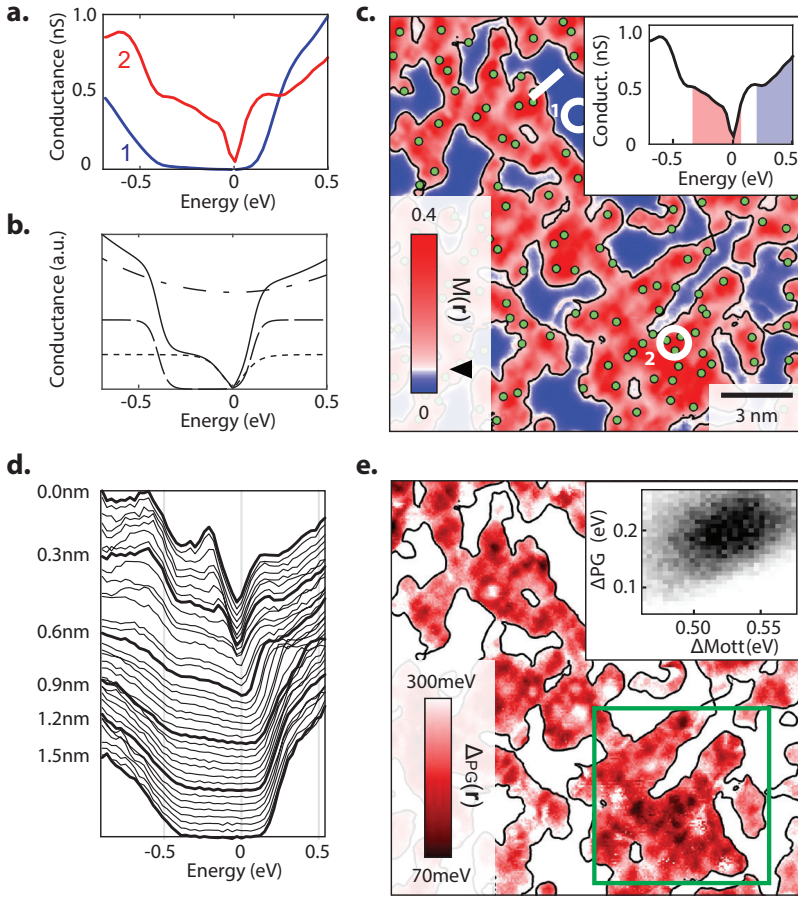


Figure 6.3: **Phase separated Mott/pseudogap electronic structure at 5.5% doping.** **a.** Different spectra in the phase separated region: Mott like spectrum (blue), with the chemical potential pinned to the UHB, and mixed Mott/pseudogap spectrum (red). The spectra are the average of 180 spectra inside the white circles in panel (c). **b.** Phenomenological fit function to simultaneously extract both the Mott and pseudogap size. It consists of a density of states (dot-dashed) multiplied with Mott gap (dashed) plus states inside the Mott gap with a v-shaped pseudogap (dotted). See appendix 6.B for details. **c.** The Mott parameter as defined in the text identifies pseudogap puddles (red) and pure Mott regions (blue). Green circles indicate La dopant locations. The triangle on the colorbar indicates the value of the black contour. Inset, definition of the Mott parameter: the integrated DOS inside Mott gap (red) normalized by the one outside the gap (blue). **d.** Local density of states spectra along the white line in (c) (each corresponding to a single measurement). The separation is sharp in the sense that a Mott spectrum becomes a pseudogap spectrum within roughly a nanometer. **e.** Δ_{PG} map extracted from the fitting procedure. The square indicates the region displayed in Figure 6.4. Inset, the correlation between Δ_{Mott} and Δ_{PG} .

We then develop a fitting procedure that is able to fit spectra both in the Mott regions and in the pseudogap puddles. The fitting function includes a phenomenological Mott gap, and additional density of states within that is gapped by a phenomenological pseudogap based on photoemission results [26, 27] and commonly used in the cuprates [7, 28] (Fig. 6.3.b and appendix 6.B). This function allows to simultaneously extract both the pseudogap Δ_{PG} (Fig. 6.3.e) and the Mott gap Δ_{Mott} for $\sim 10^5$ spectra located in the pseudogap puddles and to calculate the correlations between the two gaps. If the magnetic correlations J in the $t - J$ model are directly causing order that manifests the pseudogap, one could expect an anti-correlation between Δ_{PG} and Δ_{Mott} , as $J \sim t^2/U$. Intriguingly, within the puddles, our data show a clear positive correlation of 0.31, i.e. the larger the Mott gap, the larger the pseudogap (Fig. 6.3.e, inset). This is evidence that pseudogap and Mott physics are intimately linked [1, 29], but suggests that it is not simply the magnetic correlations that cause the pseudogap.

6.3.2. EMERGENT ORDER

To further test if the cuprate phenomenology is universal to lightly doped Mott insulators, we search for ordered phases on our samples. In the cuprates, it has become very clear that a sizable set of (possibly intertwined) orders coexist, perhaps causing the pseudogap [1]. These include disordered stripy charge arrangements, sometimes referred to as glassy order or charge density waves [1, 4–10]. Indeed, we find that the spatial distribution of the pseudogap value, when extracted with atomic precision, reveals a striking tendency for order. The Δ_{PG} gap maps exhibit glassy, locally unidirectional structures (Fig. 6.3.e and 6.4.a), reminiscent of lightly hole doped cuprates [4–8]. Glassy charge order is also visible in the density of states right outside the pseudogap, e.g. at -210 meV shown in Fig. 6.4.b-c. The arrangements consist of bond centered, unidirectional objects of length-scales of 2 to 4 Ir-Ir distances, clearly very disordered on a larger length-scale. These arrangements, like the pseudogap puddles, nucleate around the dopant atom positions (green circles).

6.4. DOPING EVOLUTION: IMPURITY BAND MOTT TRANSITION

Next, we want to elucidate how this inhomogeneous, charge ordered pseudogap state emerges from the fully gapped state at low doping, by using the unique availability of samples with densely spaced doping concentrations in the iridate family. We measure one or more spectroscopic imaging maps with $> 10^6$ data-points at each doping concentration, and we analyze each using the methods described above. Figure 6.5 summarizes the results, illustrating the abrupt nature of the transition. Panel

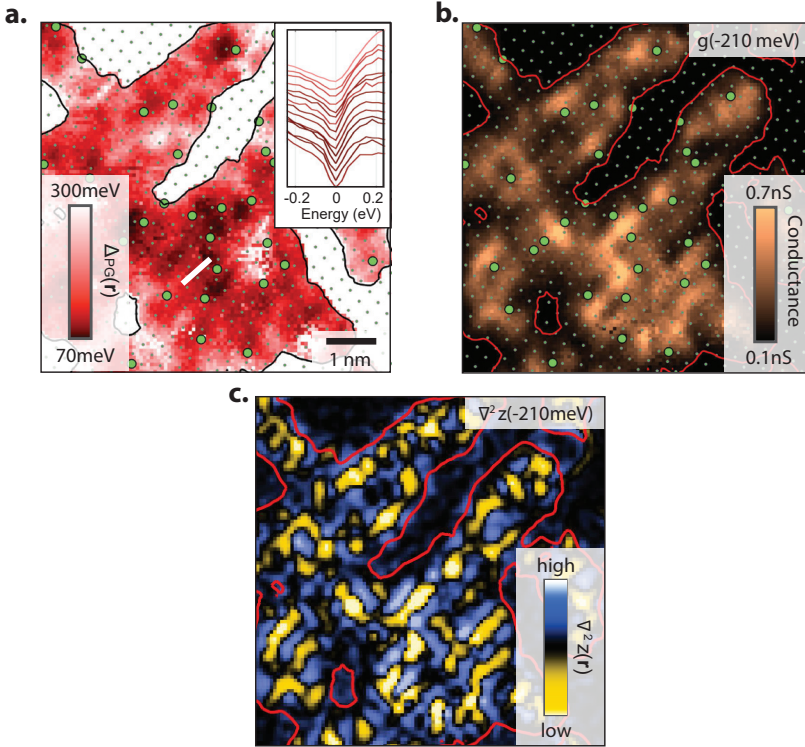


Figure 6.4: **Nucleating order.** **a.** Map of the pseudogap Δ_{PG} . The small green dots indicate Ir atom location, the larger green circles indicate La dopant locations on the Sr site. Disordered, locally unidirectional patterns are visible. The inset shows a series of spectra along the white line. The color indicates the gap value. **b.** Density of states at -210 meV. Glassy order is nucleating around the La dopant atoms. **c.** Laplacian of the ratio map at -210 meV.

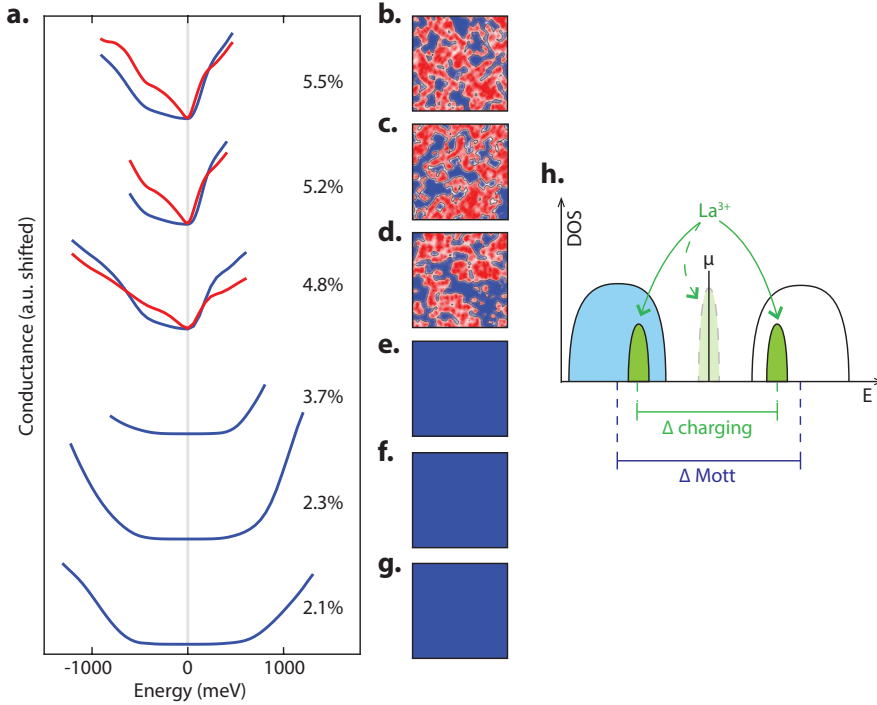


Figure 6.5: **The evolution of the electronic structure with increasing dopant atom concentration.** **a.** Density of states spectra at different doping levels, each averaged over regions with Mott gap (blue) and pseudogap (red) as defined by the Mott parameter in (b-g.) At around 5%, the phase separation abruptly starts. **b-g.** Respective maps of the Mott parameter, where blue indicates a pure Mott gap, and red indicates a pseudogap puddle. Increasing doping leads to smaller pure Mott areas. **h.** Schematic image of an impurity Mott transition, with the split impurity band states, (not) including the energy splitting Δ_{charging} in (light) green.

a shows the evolution of the averaged spectra in the regions with pseudogap (red) and in those without (blue), panels b-g show the phase separation on the respective field of views as defined by the Mott parameter defined above.

At doping concentration below the transition threshold, none of the spectra exhibits any sort of impurity state. Nor is the chemical potential pinned to one of the edges of the Mott gap, as one would expect from a Mott insulator with free carriers from shallow dopant centers. Combined with the fact that the phenomenology of the electronic structure is surprisingly independent of the doping concentration below $\sim 4\%$, this leads to the question: Where did all the dopant electrons go? We propose the scenario illustrated in Fig. 6.5.h. Tightly bound dopant electrons at the dopant locations lead to a putative dopant band (impurity band in semiconductor parlance) inside the gap which keeps the chemical potential around mid-gap. Because the extra electrons from the La^{3+} dopants reside in the upper Hubbard band in the IrO layer, they ex-

perience the strong Mott correlations. Consequently, the charging energy $E = e^2/C$ to remove or add electrons (or holes) to the $[La^{3+} + e^-]$ bound state is large enough to split the dopant band and push it outside the Mott gap (Fig. 6.5.h). An equivalent way of describing this, going back to N.F. Mott, is that there is a Mott transition in the dopant band [29]. With increasing doping, screening of the long-range Coulomb interaction by doped carriers leads to an abrupt collapse of the impurity Mott state at doping concentrations lower than one would expect in a static picture. In the cuprates, similar microscopic processes have initially been proposed, but the Mott state is much more fragile: even weak doping of around 2% can destroy the logarithmic divergence in the resistance [30]. This is due to the much smaller energy scales of the trapping in the cuprates; below the transitions, the material behaves similar to a doped semiconductor, with an impurity band close to the energy of the valence band [30]. This is consistent with the later observation that the dopant centers are quite shallow [6]. Based on our results, we predict that LDA+U calculations [3, 31] on doped iridates will reveal the trapping of La dopant states to be much deeper than the equivalent states in the cuprates, and that more homogenous samples will reveal a very sharp impurity band metal-insulator transition.

6.5. CONCLUSIONS AND OUTLOOK

In this chapter we have shown the melting of the Mott state in Sr_2IrO_4 upon electron doping, leading to the abrupt appearance of a phase-separated state at $x \approx 5\%$. The presence of the pseudogap we report in this chapter is to date well established and has been confirmed by other experimental techniques such as ARPES [26, 27] and optical spectroscopy [32, 33]. However, the microscopic origin of the pseudogap phase still remains unknown. We believe that both scanning noise and/or Josephson tunneling experiments, as described in previous chapters, could potentially resolve the true nature of the pseudogap state in doped Mott insulators, including both the iridate as cuprate families.

To conclude this chapter, we would like to go back to the comparison of the electron doped iridate material studied here to the cuprates. Detailed measurements on the cuprates, e.g. $Ca_{2-x}Na_xCuO_2Cl_2$ and $Bi_2Sr_2CaCu_2O_{8+\delta}$, revealed surprising universalities including the glassy charge order observed in the CuO layer. On first look, based on its chemical make-up, $(Sr_{1-x}La_x)_2IrO_4$ seems to be a very different material (Ir instead of Cu and $5d^5$ instead of $3d^9$ electrons). However, our data clearly shows that the physics of electronic order and the pseudogap are not specific to the cuprates but generic to lightly doped Mott insulators, and we believe that the interplay between dopants and order seen here holds for the cuprates as well. By extension, we can expect $(Sr_{1-x}La_x)_2IrO_4$ to become a high-temperature superconductor with only slightly higher doping concentration.

APPENDICES

6.A. EXPERIMENTAL SETUP

The STM experiments are performed with a modified, low-temperature, ultrahigh vacuum STM system from Unisoku. The $(\text{Sr}_{1-x}\text{La}_x)_2\text{IrO}_4$ crystals are cleaved in situ at temperature $T \sim 20\text{K}$ and base pressure $p = 2 \times 10^{-10}\text{mbar}$, and then transferred immediately into the STM sample stage. All STM results reported in this paper are acquired in cryogenic vacuum at temperatures of either $T \sim 2\text{K}$ or $T \sim 7\text{K}$ (no significant difference in our measurements has been observed between these temperatures). The STM topographs are taken in the constant current mode, and the dI/dV spectra are collected using a standard lock-in technique with modulation frequency $f = 857\text{Hz}$. Importantly, we set each spectrum up at I_{bias} and V_{bias} , and then sweep all the voltages. We use mechanically grinded PtIr tips for all the measurements. We always test the spectroscopic and topographic properties of the tips on a crystalline Au(111) surface prepared in situ by Ar ion sputtering and temperature annealing before measuring $(\text{Sr}_{1-x}\text{La}_x)_2\text{IrO}_4$. The topographs in Fig. 6.1.e-f are set up at -1.2V , 200pA . The map in Fig. 6.2 is set up at 1.2V , 500pA . The map in Figs. 6.3, 6.4 is set up at 460mV , 300pA . The maps in Figs. 6.5 are set up as following: Fig. 6.5.b: 460mV , 300pA ; Fig. 6.5.c: -0.4V , 250pA ; Fig. 6.5.d: -1.2V , 700pA ; Fig. 6.5.e: 0.9V , 220pA , Fig. 6.5.f: 1.2V , 250pA ; Fig. 6.5.g: 1.2V , 250pA .

6.B. EXTRACTION OF Δ_{MOTT} AND Δ_{PG}

In order to fit the vastly different spectra both in the Mott region and in the pseudogap puddles, we develop a fitting procedure as follows. We start with a smooth polynomial background density of states $\text{DOS}_{BG}(E) = aE^2 + c$, where E is the energy, and a and c are fitting parameters. Next, we multiply it with a phenomenological Mott gap Δ_{Mott} consisting of two slightly broadened gap edges, asymmetric around the chemical potential:

$$\Delta_{\text{Mott}}(E) = \left| \frac{1}{1 + e^{\frac{-E-E_0}{w}}} - \frac{1}{1 + e^{(-E+E_0-\Delta_{\text{Mott}})/w}} \right| \quad (6.2)$$

The gap edges are broadened by w , E_0 is the energy where the upper Hubbard band roughly pins to the chemical potential and Δ_{Mott} is the size of the Mott gap. We keep the first two parameters fixed ($w = 0.026\text{eV}$, $E_0 = 0.1\text{eV}$), while the size of the Mott gap Δ_{Mott} is used as a fitting parameter. We then allow for states inside the Mott gap that are gapped by introducing a phenomenological function based on photoemission results [26, 27] and commonly used in the cuprates [7, 28]. This part allows for

the extraction of the pseudogap value Δ_{PG} .

$$DOS_{PG}(E) = C_0 \left| \frac{E + i\alpha\sqrt{E}}{\sqrt{(E + i\alpha\sqrt{E})^2 - \Delta_{PG}^2}} \right| \quad (6.3)$$

This function contains two fitting parameters: a scaling factor C_0 and the size of the pseudogap Δ_{PG} . We keep α , an effective scattering rate, fixed to 0.2 eV. The square root in the imaginary part of the self-energy is selected to ensure a rather constant broadening independent of the gap. Albeit $DOS_{PG}(E)$ is inspired by recent photoemission results and experiences from the cuprates [27, 28], we emphasize that our motivation was to extract the key physical quantities with few fitting parameters. We expect future theoretical progress to yield even better, less phenomenological, fit functions.

At each point of the spectroscopy map the data is fitted with the constructed fit function, using the least squares method. The initial guess is provided by fitting the average of all spectra in the dataset. Since in the high-doping regime the upper edge of the Mott gap is pinned to the chemical potential, and because in that location pseudogap and Mott gap overlap, we only fit the model to the data for negative energies.

BIBLIOGRAPHY

- [1] B. Keimer, S. A. Kivelson, M. R. Norman, S. Uchida, and J. Zaanen, *From quantum matter to high-temperature superconductivity in copper oxides*, *Nature* **518**, 179 (2015).
- [2] J. G. Rau, E. K.-H. Lee, and H.-Y. Kee, *Spin-orbit physics giving rise to novel phases in correlated systems: Iridates and related materials*, *Annual Review of Condensed Matter Physics* **7**, 195 (2016).
- [3] B. J. Kim, H. Jin, S. J. Moon, J.-Y. Kim, B.-G. Park, C. S. Leem, J. Yu, T. W. Noh, C. Kim, S.-J. Oh, J.-H. Park, V. Durairaj, G. Cao, and E. Rotenberg, *Novel $J_{\text{eff}} = 1/2$ mott state induced by relativistic spin-orbit coupling in Sr_2IrO_4* , *Phys. Rev. Lett.* **101**, 076402 (2008).
- [4] K. Fujita, M. Hamidian, I. Firmo, S. Mukhopadhyay, C. K. Kim, H. Eisaki, S.-i. Uchida, and J. Davis, *Spectroscopic imaging stm: Atomic-scale visualization of electronic structure and symmetry in underdoped cuprates*, in *Strongly Correlated Systems* (Springer, 2015) pp. 73–109.
- [5] Y. Kohsaka, K. Iwaya, S. Satow, T. Hanaguri, M. Azuma, M. Takano, and H. Takagi, *Imaging nanoscale electronic inhomogeneity in the lightly doped mott insulator $\text{Ca}_{2-x}\text{Na}_x\text{CuO}_2\text{Cl}_2$* , *Phys. Rev. Lett.* **93**, 097004 (2004).
- [6] P. Cai, W. Ruan, Y. Peng, C. Ye, X. Li, Z. Hao, X. Zhou, D.-H. Lee, and Y. Wang, *Visualizing the evolution from the mott insulator to a charge-ordered insulator in lightly doped cuprates*, *Nature Physics* **12**, 1047 (2016).
- [7] Y. Kohsaka, T. Hanaguri, M. Azuma, M. Takano, J. Davis, and H. Takagi, *Visualization of the emergence of the pseudogap state and the evolution to superconductivity in a lightly hole-doped mott insulator*, *Nature Physics* **8**, 534 (2012).
- [8] C. V. Parker, P. Aynajian, E. H. da Silva Neto, A. Pushp, S. Ono, J. Wen, Z. Xu, G. Gu, and A. Yazdani, *Fluctuating stripes at the onset of the pseudogap in the high- T_c superconductor $\text{Bi}_2\text{Sr}_2\text{CaCu}_2\text{O}_{8+x}$* , *Nature* **468**, 677 (2010).
- [9] R. Comin and A. Damascelli, *Resonant x-ray scattering studies of charge order in cuprates*, *Annual Review of Condensed Matter Physics* **7**, 369 (2016).
- [10] E. Fradkin, S. A. Kivelson, and J. M. Tranquada, *Theory of intertwined orders in high temperature superconductors*, *Rev. Mod. Phys.* **87**, 457 (2015).
- [11] F. Wang and T. Senthil, *Twisted hubbard model for Sr_2IrO_4 : Magnetism and possible high temperature superconductivity*, *Phys. Rev. Lett.* **106**, 136402 (2011).
- [12] H. Watanabe, T. Shirakawa, and S. Yunoki, *Monte carlo study of an unconventional superconducting phase in iridium oxide $J_{\text{eff}}=1/2$ mott insulators induced by carrier doping*, *Phys. Rev. Lett.* **110**, 027002 (2013).

- [13] Y. Okada, D. Walkup, H. Lin, C. Dhital, T.-R. Chang, S. Khadka, W. Zhou, H.-T. Jeng, M. Paranjape, A. Bansil, Z. Wang, S. D. Wilson, and V. Madhavan, *Imaging the evolution of metallic states in a correlated iridate*, Nature materials **12**, 707 (2013).
- [14] K. McElroy, J. Lee, J. Slezak, D.-H. Lee, H. Eisaki, S. Uchida, and J. Davis, *Atomic-scale sources and mechanism of nanoscale electronic disorder in $\text{Bi}_2\text{Sr}_2\text{CaCu}_2\text{O}_{8+\delta}$* , Science **309**, 1048 (2005).
- [15] I. Zeljkovic, Z. Xu, J. Wen, G. Gu, R. S. Markiewicz, and J. E. Hoffman, *Imaging the impact of single oxygen atoms on superconducting $\text{Bi}_{2+\text{y}}\text{Sr}_{2-\text{y}}\text{CaCu}_2\text{O}_{8+\text{x}}$* , Science **337**, 320 (2012).
- [16] C. Ye, P. Cai, R. Yu, X. Zhou, W. Ruan, Q. Liu, C. Jin, and Y. Wang, *Visualizing the atomic-scale electronic structure of the $\text{Ca}_2\text{CuO}_2\text{Cl}_2$ mott insulator*, Nature communications **4**, 1365 (2013).
- [17] I. Battisti, V. Fedoseev, K. M. Bastiaans, A. de la Torre, R. S. Perry, F. Baumberger, and M. P. Allan, *Poor electronic screening in lightly doped mott insulators observed with scanning tunneling microscopy*, Phys. Rev. B **95**, 235141 (2017).
- [18] R. M. Feenstra, Y. Dong, M. Semtsiv, and W. Masselink, *Influence of tip-induced band bending on tunnelling spectra of semiconductor surfaces*, Nanotechnology **18**, 044015 (2006).
- [19] A. P. Wijnheijmer, J. K. Garleff, K. Teichmann, M. Wenderoth, S. Loth, and P. M. Koenraad, *Single si dopants in gaas studied by scanning tunneling microscopy and spectroscopy*, Phys. Rev. B **84**, 125310 (2011).
- [20] S. J. Moon, H. Jin, W. S. Choi, J. S. Lee, S. S. A. Seo, J. Yu, G. Cao, T. W. Noh, and Y. S. Lee, *Temperature dependence of the electronic structure of the $J_{\text{eff}} = \frac{1}{2}$ mott insulator Sr_2IrO_4 studied by optical spectroscopy*, Phys. Rev. B **80**, 195110 (2009).
- [21] X. Chen, T. Hogan, D. Walkup, W. Zhou, M. Pokharel, M. Yao, W. Tian, T. Z. Ward, Y. Zhao, D. Parshall, C. Opeil, J. W. Lynn, V. Madhavan, and S. D. Wilson, *Influence of electron doping on the ground state of $(\text{Sr}_{1-\text{x}}\text{La}_{\text{x}})_2\text{IrO}_4$* , Phys. Rev. B **92**, 075125 (2015).
- [22] Y. J. Yan, M. Q. Ren, H. C. Xu, B. P. Xie, R. Tao, H. Y. Choi, N. Lee, Y. J. Choi, T. Zhang, and D. L. Feng, *Electron-doped Sr_2IrO_4 : An analogue of hole-doped cuprate superconductors demonstrated by scanning tunneling microscopy*, Phys. Rev. X **5**, 041018 (2015).
- [23] J. Dai, E. Calleja, G. Cao, and K. McElroy, *Local density of states study of a spin-orbit-coupling induced mott insulator Sr_2IrO_4* , Phys. Rev. B **90**, 041102 (2014).

- [24] J. He, T. Hogan, T. R. Mion, H. Hafiz, Y. He, J. Denlinger, S. Mo, C. Dhital, X. Chen, Q. Lin, Y. Zhang, M. Hashimoto, H. Pan, D. Lu, M. Arita, K. Shimada, R. Markiewicz, Z. Wang, K. Kempa, M. Naughton, A. Bansil, S. Wilson, and R.-H. He, *Spectroscopic evidence for negative electronic compressibility in a quasi-three-dimensional spin-orbit correlated metal*, Nature materials **14**, 577 (2015).
- [25] Y. K. Kim, O. Krupin, J. Denlinger, A. Bostwick, E. Rotenberg, Q. Zhao, J. Mitchell, J. Allen, and B. Kim, *Fermi arcs in a doped pseudospin-1/2 heisenberg antiferromagnet*, Science **345**, 187 (2014).
- [26] A. de la Torre, S. McKeown Walker, F. Y. Bruno, S. Ricc , Z. Wang, I. Gutierrez Lezama, G. Scheerer, G. Giriat, D. Jaccard, C. Berthod, T. K. Kim, M. Hoesch, E. C. Hunter, R. S. Perry, A. Tamai, and F. Baumberger, *Collapse of the mott gap and emergence of a nodal liquid in lightly doped sr_2iro_4* , Phys. Rev. Lett. **115**, 176402 (2015).
- [27] Y. K. Kim, N. Sung, J. Denlinger, and B. Kim, *Observation of a d-wave gap in electron-doped sr_2iro_4* , Nature Physics **12**, 37 (2016).
- [28] J. Alldredge, J. Lee, K. McElroy, M. Wang, K. Fujita, Y. Kohsaka, C. Taylor, H. Eisaki, S. Uchida, P. Hirschfeld, and J. Davis, *Evolution of the electronic excitation spectrum with strongly diminishing hole density in superconducting $\text{bi}_2\text{sr}_2\text{cacu}_{2-o}\delta$* , Nature Physics **4**, 319 (2008).
- [29] N. F. Mott, *Metal-insulator transition*, Rev. Mod. Phys. **40**, 677 (1968).
- [30] M. A. Kastner, R. J. Birgeneau, G. Shirane, and Y. Endoh, *Magnetic, transport, and optical properties of monolayer copper oxides*, Rev. Mod. Phys. **70**, 897 (1998).
- [31] V. I. Anisimov, J. Zaanen, and O. K. Andersen, *Band theory and mott insulators: Hubbard u instead of stoner i* , Phys. Rev. B **44**, 943 (1991).
- [32] J. H. Seo, G. H. Ahn, S. J. Song, X. Chen, S. D. Wilson, and S. J. Moon, *Infrared probe of pseudogap in electron-doped sr_2iro_4* , Sci. Rep. **7**, 10494 (2017).
- [33] K. Wang, N. Bachar, J. Teyssier, W. Luo, C. W. Rischau, G. Scheerer, A. de la Torre, R. S. Perry, F. Baumberger, and D. van der Marel, *Mott transition and collective charge pinning in electron doped sr_2iro_4* , Phys. Rev. B **98**, 045107 (2018).

Samenvatting

Dit proefschrift beschrijft het onderzoek naar zogenoemde kwantummaterie gerealiseerd in elektronsystemen in een vaste stof. Het denkbeeld dat de elektronische fasetoestand van het materiaal in essentie niet hetzelfde hoeft te zijn als die van de vaste stof, zodat beide beschouwd kunnen worden als afzonderlijke eigenschappen van het materiaal, vormt hierbij een inspiratiebron. Bijvoorbeeld voor de meeste simpele metalen (een vaste stof) beschrijven we de elektronische eigenschappen aan de hand van een vloeibare of gasvormige elektronische fasetoestand. Dit is mogelijk omdat de afstotende Coulombkracht tussen de elektronen in het materiaal dermate klein is dat we de elektronen als nagenoeg onafhankelijk van elkaar kunnen beschouwen. Maar hoe zit het met materialen waar de interacties tussen de elektronen niet te verwaarlozen is? Hierbij betreden we het rijk der *kwantummaterialen*. Hier houdt het beeld van de onafhankelijke elektronen geen stand meer; de onderlinge krachten worden zo sterk dat de elektronen en daarmee het gehele elektronische systeem *sterk gecorreleerd* wordt. Dit heeft als gevolg dat het collectieve gedrag van alle elektronen de algemene elektronische eigenschappen van het materiaal gaat dicteren. Het fascinerende is dat vanuit deze microscopische brei van sterk gecorreleerde elektronen macroscopische eigenschappen kunnen oprijzen die van nature kwantummechanisch van aard zijn.

Omdat de meeste van deze emergente - een verschijnsel waar het geheel groter lijkt te zijn dan de som der delen - toestanden complexe eigenschappen bezitten, willen we zowel de microscopische details als de drijvende kracht van de emergentie begrijpen. Omdat er hierbij een samenspel lijkt te zijn tussen de elektronische en atomaire structuur van het materiaal maken we in dit proefschrift gebruik van een experimentele techniek die ons in staat stelt om beide te visualiseren op de atomaire schaal. We bouwen voort op de meest geavanceerde methodes en voegen nieuwe technieken toe die ons in staat stellen om het onbekende terrein van de kwantummaterie in sterk gecorreleerde materialen verder te verkennen.

In hoofdstuk 2 van dit proefschrift beschrijven we de ontwikkeling van een nieuw soort microscoop die wij de 'scanning tunneling noise microscope' dopen. Deze techniek is geïnspireerd op de woorden van Rolf Landauer "De ruis is het signaal", waarmee hij bedoelt dat de fluctuaties in de tijd van een meting een bron van informatie is die niet toegankelijk is in de tijdgemiddelde waarde van de meting.

Onze microscoop is opgebouwd uit een scherpe, geleidende naald die we in 'tunnelcontact' brengen met het te bestuderen materiaal. De elektronen die dan kunnen stromen in dit contact volgen een Poissonproces, wat inhoudt dat de elektronen onafhankelijk en op volkomen willekeurige momenten in de tijd overstappen tussen naald en materiaal. De netto som aan lading die per tijdseenheid wordt overgedragen is wat we beschouwen als de (tijdsgemiddelde) stroomsterkte. De standaardafwijking van dit gemiddelde is wat we verstaan onder de ruis. De stroomruis in een tunnelcontact ontstaat door het feit dat de stroming van ladingsdragers discreet is, bestaand uit kleine ladingspakketjes: de elektronen. In hoofdstuk 2 beschrijven wij de ontwikkeling van een nieuwe voorversterker, die wij kunnen gebruiken om de stroomruis in het tunnelcontact te meten. We demonstreren de unieke prestaties van deze versterker door deze uitgebreid te testen op een metallisch materiaal.

In hoofdstuk 3 gebruiken wij deze nieuw 'scanning noise' microscoop om een koper-oxidaat, een kwantummateriaal waar de sterke correlaties tussen de ladingsdragers leiden tot supergeleiding met een relatief hoge transitietemperatuur, te verkennen. Hierbij ontdekken we atomaire 'hotspots' waar de stroomruis fluctuaties laat zien die tot wel 40 keer groter zijn dan de verwachte waarde voor ongecorrleerde systemen. Door deze ontdekking te combineren met de reeds bestaande onderzoeksmethodes kunnen we deze atomaire ruispunten correleren met de elektronische en atomaire structuur. Uit deze vergelijking kunnen wij concluderen dat deze ruispunten toe te schrijven zijn aan lokale invang van ladingen in het materiaal. De resultaten gepresenteerd in dit hoofdstuk schetsen een nieuw beeld van hoe men naar deze materialen moet kijken: een atomaire stapeling van metallische lagen gescheiden door polarizeerbare isolerende lagen, leidend tot een driedimensionale supergeleidende toestand.

De tweede nieuwe techniek waar we gebruik van maken in dit proefschrift is gebaseerd op het *Josephson* effect. Door een supergeleidende naald in contact te brengen met een supergeleidend materiaal koppelen we twee supergeleidende macroscopische objecten door een dunne isolerende vacuumbarière. Op deze manier creëren we een scanbare Josephsonjunctie. De tunnelstroom kan nu naast enkele elementaire ladingen ook door gepaarde (supergeleidende) ladingen gedragen worden. Deze gepaarde ladingen geven directe toegang tot het supergeleidende condensaat in het materiaal.

In hoofdstuk 4 combineren we onze 'scanning noise' microscoop met deze 'Josephson' techniek. We visualiseren de stroomruis met atomaire resolutie op een supergeleidend Pb(111) oppervlak door gebruik te maken van een supergeleidende Pb naald. Door de stroomruis te meten als functie van de spanning over de junctie laten we zien dat er een transitie plaatsvindt van transport van enkele elementaire ladingen buiten het supergeleidende regime naar transport van gepaarde ladingen binnen het supergeleidende energiebereik. Dit tonen we aan door de verdubbeling in de

stroomruis als gevolg van het paren van de ladingsdragers te meten en ook ruimtelijk in kaart te brengen op het Pb(111) oppervlak.

We gebruiken deze 'Josephson Scanning Tunneling Microscoop' ook in hoofdstuk 5 om de sterk inhomogene aard van het supergeleidende condensaat in een ijzer-gebaseerde supergeleider te visualiseren. Voorafgaand aan dit onderzoek werd er al gespeculeerd dat het supergeleidende condensaat in deze materialen ruimtelijk sterk zou kunnen variëren en nu tonen wij dit experimenteel aan met atomaire resolutie. Door tegelijkertijd ook de topografische en elektronische eigenschappen van dit materiaal te meten, ontdekken we dat de inhomogeniteit in het supergeleidende condensaat gecorreleerd is met de coherentie van de quasi-deeltjes. Dit impliceert dat supergeleiding nodig lijkt te zijn voor coherente quasi-deeltjes, lokaal, op de lengteschaal van de supergeleidende paring van elektronen.

In het laatste hoofdstuk van dit proefschrift, hoofdstuk 6, visualiseren we de elektronische eigenschappen van het iridaat Sr_2IrO_4 , een kwantummateriaal waar door de sterke correlaties tussen de elektronen de ladingsdragers niet vrij door het materiaal kunnen bewegen. Doordat de elektronen als het ware 'vastgevroren' zitten op de atomaire positie gedraagt dit materiaal zich als een elektrische isolator (een zogenoemde Mott-isolator). Wij meten de lokale elektronische eigenschappen van dit materiaal terwijl het een overgang ondergaat van de vaste 'Mott'-toestand naar de 'pseudogap' toestand. We laten zien dat wanneer er extra ladingsdragers worden toegevoegd aan het materiaal er een fase-gesepareerde toestand ontstaat samen met emergente elektronische structurering op atomaire lengteschaal. Hoewel er weinig chemische overeenkomsten zijn, observeren we wel dezelfde fysische effecten als in de koperoxide hoge-temperatuur supergeleiders. Daarom beschouwen wij deze verschijnselen als algemene eigenschappen van gedoopte Mott-isolatoren, onafhankelijk van hun chemische samenstelling.

Curriculum Vitae

I, Koen Mathijs Bastiaans, was born on 7 April 1990 in Leiden, and always kept a strong connection to my city of birth. After graduating from the Stedelijk Gymnasium in Leiden in 2008 with double study profiles (Science & Health and Science & Technology), I started my studies in Business Administration at the Vrije Universiteit in Amsterdam. Soon after, I realized how much I truly enjoy the challenges and beauty of the natural sciences and therefore decided to enroll for the Physics program at Leiden University in 2009. Early 2013 I obtained my BSc degree in Physics after having worked under the supervision of Prof. S.J. van der Molen on a project where we studied the conduction properties of spin-transition molecules in a gold nanoparticle network. I continued my studies in Physics at Leiden University following the MSc 'Experimental Physics'-track, where I worked on two thesis projects. One under the supervision of Prof. T.H. Oosterkamp studying the low temperature dissipation of superconductors and one with Dr. M.P. Allan working on a Spin Hall effect-based STM tip. I obtained my MSc degree in Physics in 2015 and decided, driven by the passion I found for experimental physics, to continue to pursue a PhD in Physics under the supervision of Dr. M.P. Allan, working on novel experimental probes to investigate the mysteries of strongly correlated quantum materials.

List of Publications

11. **K.M. Bastiaans**, T. Benschop, D. Chatzopoulos, D. Cho, Q. Dong, Y. Jin and M.P. Allan, "*Amplifier for scanning tunneling microscopy at MHz frequencies*", Review of Scientific Instruments **89**, 093709 (2018) (*Chapter 2*).
10. **K.M. Bastiaans***, D. Cho*, T. Benschop, I. Battisti, Y. Huang, M.S. Golden, Q. Dong, Y. Jin, J. Zaanen and M.P. Allan, "*Charge trapping and super-Poissonian noise centers in a cuprate superconductor*", Nature Physics **14**, 1183 (2018) (*Chapter 3*).
9. **K.M. Bastiaans**, D. Cho, D. Chatzopoulos, M. Leeuwenhoek, C. Koks and M.P. Allan, "*Imaging doubled shot noise in a Josephson Scanning Tunneling Microscope*", Physical Review B **100**, 104506 (2019) (*Chapter 4*).
8. D. Cho*, **K.M. Bastiaans***, D. Chatzopoulos*, G.D. Gu and M.P. Allan, "*A strongly inhomogeneous superfluid in an iron-based superconductor*", Nature **571**, 541 (2019) (*Chapter 5*).
7. I. Battisti*, **K.M. Bastiaans***, V. Fedoseev, A. de la Torre, N. Iliopoulos, A. Tamai, E.C. Hunter, R.S. Perry, J. Zaanen, F. Baumberger and M.P. Allan, "*Universality of pseudogap and emergent order in lightly doped Mott insulators*", Nature Physics **13**, 21 (2017) (*Chapter 6*).
6. D. Chatzopoulos, **K.M. Bastiaans**, D. Cho, G.D. Gu and M.P. Allan, "*Tunable impurity states in the unconventional iron-based superconductor $\text{FeTe}_{0.55}\text{Se}_{0.45}$* ", in preparation.
5. M. Leeuwenhoek, R.A. Norte, **K.M. Bastiaans**, D. Cho, I. Battisti, Y.M. Blanter, S. Gröblacher and M.P. Allan, "*Nanofabricated tips for device-based scanning tunneling microscopy*", Nanotechnology **30**, 335902 (2019).
4. I. Battisti, G. Verdoes, K. van Oosten, **K.M. Bastiaans** and M.P. Allan, "*Definition of design guidelines, construction, and performance of an ultra-stable scanning tunneling microscope for spectroscopic imaging*", Review of Scientific Instruments **89**, 123705 (2018).

*These authors contributed equally

3. S. Tewari, **K.M. Bastiaans**, M.P. Allan and J.M. van Ruitenbeek, "*Robust procedure for creating and characterizing the atomic structure of scanning tunneling microscope tips*", Beilstein Journal of Nanotechnology **8**, 2389 (2017).
2. I. Battisti, V. Fedoseev, **K.M. Bastiaans**, A. de la Torre, R.S. Perry, F. Baumberger and M.P. Allan, "*Poor electronic screening in lightly doped Mott insulators observed with scanning tunneling microscopy*", Physical Review B **95**, 235141(R) (2017)
1. J.J.T. Wagenaar*, A.M.J. den Haan*, J.M. de Voogd, T.A. de Jong, M. de Wit, **K.M. Bastiaans**, D.J. Thoen, A. Endo, T.M. Klapwijk, J. Zaanen and T.H. Oosterkamp, "*Probing the nuclear spin-lattice relaxation time at the nanoscale*", Physical Review Applied **6**, 014007 (2016)

Acknowledgements

I consider this, without any doubt, as the most important part of my dissertation. Most of the scientific progress presented here is a result of the hard work over the past four years and could not have been done without the collaboration, discussions and support of many great people.

First and foremost, nothing of this would have been realized without the fantastic support, trust and encouragement of my supervisor Milan Allan. Our deep discussions about physics, technological and personal development, decision making and always striving forward were an unforgettable experience for me. Thanks for sharing this amazing adventure together!

I would like to express my sincere gratitude to the professors at the Leiden Institute of Physics, of which many acted, knowingly or unknowingly, as great teachers and mentors to me. Jan Aarts, thanks for acting as my promotor, being that stable and experienced factor in the process. Sense Jan van der Molen and Tjerk Oosterkamp, I would like to thank you for being my early mentors, opening the fascinating world of experimental physics. Jan van Ruitenbeek, for your broad knowledge and our valuable discussions on noise experiments. And Jan Zaanen, your deep knowledge and enthusiasm for strongly correlated electron systems excellently placed our measurement results into the right perspective.

Also I would like to thank our collaborators from all over the globe. Alberto de la Torre (University of Geneva / Caltech), Robin Perry (University College London), Anna Tamai and Felix Baumberger (both University of Geneva), I really appreciate our collaboration on the lightly-doped iridates. Yingkai Huang and Mark Golden from the University of Amsterdam, thanks for growing the Pb-doped BSCCO samples. Genda Gu at Brookhaven National Lab, for providing the finest Fe(Se,Te) samples. Quan Dong and Yong Jin at C2N in Paris, for their superior ultra-low noise HEMT's and advice on how to squeeze the most out of them. Freek Massee at CNRS in Paris, for our early discussion on making the MHz amplifier. Dirk Morr at the University of Illinois at Chicago and Teun Klapwijk at the TU Delft, for our discussions on noise and Josephson measurements.

Special thanks to all the employees of Unisoku, for delivering such a wonderful product. In particular: Toshiyuki Kishimoto, Yoshihide Seino and Katsuya Iwaya, your advice and help was always excellent.

Closer to home I want to thank all the members of the Allan lab. It is a real pleasure to be part of this dynamic and stimulating team. Irene Battisti, of course you were there from day one. I will never forget setting up Tamagotchi together and the great team we formed on the iridates project. The always smiling Doohee Cho, it was a real honor to explore the noise on the cuprates with you, the tricky journeys on lead and our successes on the iron-based samples. Study hard! In this light also Damianos Chatzopoulos, completing the Tamagotchi team. A big thanks to Tjerk Benschop (who also was my student), developing the double-tank amplifier maybe was our finest moment. And of course all other members of the Allan lab: Nikolaos Iliopoulos, Vitaly Fedoseev, Maarten Leeuwenhoek, for his smart tips, Willem Tromp and Vincent Stalman, for bravely eating away all his noodles. Also I am thankful to all the students who helped me throughout the different projects: Farshaad Hoeseni, Tjerk Benschop, Margot Leemker, Vishnu Saj, Bert Visscher, Ahmad Jamalzada, Corn   Koks and Kemal Demir.

Many thanks to all my colleagues at the Leiden Institute of Physics, who all contributed in many different ways: the guys with the golden hands at the FMD and ELD, especially Gijsbert Verdoes, Kees van Oosten and Freek Groenewoud as close members of the Allan lab. Peter van Veldhuizen, Bert Crama and Co Konings at the electronics department. Kier Heeck, for reminding me about the ratio of things. Marcel Rost, for your enthusiasm and our discussions on radio-frequency STM. Wilfred van der Geest, for keeping the helium liquid. Sumit Tewari, for the art of mechanical annealing. Edwin Devid, my early mentor. Arthur den Haan, for sharing your knowledge on interfacing instruments. And Ellie van Rijsewijk, for making sure everything went as smooth as it can be.

My close friends, in random order: Maarten, Martin, Jelmer, Oliver, EJ, Nigel, Freek and Patrick (for paying the bills). Whom I shared my physics education with from the beginning, for different lengths, and who are always there to make sure life in- and outside the lab is never boring.

Tenslotte, wil ik uiteraard mijn familie bedanken. Pap, mam, Daan en Tim, jullie zijn stuk voor stuk fantastisch! Lein, een liefdevollere steun kan ik me niet wensen. Ik kijk al uit naar ons volgende avontuur.